Application of Density Functional Theory to Heterogeneous Catalysis and Development of Computational Methods for Photochemistry

A DISSERTATION
SUBMITTED TO THE FACULTY OF
UNIVERSITY OF MINNESOTA BY

Suman Bhaumik

IN PARTIAL FULFILLMENT OF THE REQUIREMENTS
FOR THE DEGREE OF
DOCTOR OF PHILOSOPHY

Professor Donald G. Truhlar, Adviser

January 2025

Acknowledgements

I would like to thank my advisor Prof. Donald Truhlar for accepting me into his group, guiding me throughout my Ph. D. journey, and for the immense support during the time of my knee surgery. I feel lucky to be able to do research with an imminent researcher like Prof. Donald Truhlar, and have learnt a lot during this phase.

I would like to thank all the members of the Truhlar group for all the help with my research work. Not only are the group members very smart, but they are also extremely hard working. I have learnt a lot from all of them. I would like to thank Dr. Kelsey Parker for her support and guidance even after she finished her Ph.D. I would like to thank Dr. Siriluk Kanchanukungwangkul for being a mentor to me, that helped me navigate a lot of the issues I faced. I would like to thank Dr. Yinan Shu for being an invaluable academic mentor and collaborator. I would like to thank Dr. Dayou Zhang for his input in understanding different quantum mechanical concepts and coding concepts.

I would also like to acknowledge my experimental collaborator Prof. Joseph Hupp, Ying Yang, Qing Ma, and Sol Ahn for the wonderful collaboration.

I would like to thank my mother and father who have been immensely supportive of me throughout this journey. My mother has been my strongest pillar of strength. I would like to thank my brother Sudip Bhaumik, my cousin Tamal Bhowmik and all my relatives back in India whose support to my family helped me finish my Ph. D. without dwelling much into those thoughts. I would like to thank my friends for being there for me.

I would like to thank my best friend Abhishek Sahoo for always being there for me. I would like to thank Akanksha Aggarwal for supporting me and understanding me. I would like to thank Hridya Premnathan for being an amazing friend over the years. I would like to thank my friends Stuti Gupta, Ramachandra Sorren, Ujjayanta Bhaumik, Biswajit Sahoo, and Abhishek Roy for keeping me sane. I would like to thank Adrian Gordon, Zhihao Wu, Jacob Schaffner, Eduardo Medina, and Punarbasu Roy for all the fun times. I would also like to thank Bittu Chandra, Arpan Biswas, and Rajneesh Singh for the amazing times. I

would like to thank my friends Aditya Madabhushi, Nanda Unnikrishnan, Debarati Das, Vidya Chhabria, Smitha Muthya, Preethy Parthiban, Shruti Verma, and Taaresh Taneja for providing me the sense of belonging and community.

I would like to thank my teachers Dr. Sudhan Debnath, Dr. Atanu Bhattacharyya, and Dr. Sameer Sapra for encouraging me and supporting me over the years to pursue research as a career option.

Dedication

This thesis is dedicated to my mother and father for their love and support throughout my life. My mother could not even finish high school due to poor economic background. She has been my pillar of support since my childhood. This Ph. D. is as much as mine as my mother's. This thesis is also dedicated to a few friends who have been there for me through ups and downs of life.

Abstract

This Ph. D. thesis focuses on modeling heterogeneous catalysis and developing methods for quantum mechanical photochemistry.

Density functional theory (DFT) is one of the most widely used methods for structural and mechanistic studies of chemical reactions in heterogeneous catalysis. DFT has been powerful for the discovery of new structures, functionalities of new materials, and in the determination of possible reaction mechanisms. Despite the efforts to study Cu-catalyzed methane oxidation to methanol, there has been no consensus thus far about the actual structure of the active site(s) or the mechanism(s). In Chapter 2, we have modeled the active site of and mechanistic pathways for catalysis of methane to methanol through DFT calculations in Gaussian and through enzyme biomimicking enabling the identification and validation of the material Cu-ZIF for controlled C-H bond activation.

Photochemistry is very important for organic synthesis and photosynthesis. We need quantum mechanical methods which are accurate as well as computationally affordable. For direct dynamics, in Chapter 3, we focus on the usage of the curvature-driven coherent switching with decay of mixing dynamical method Like Trajectory Surface Hopping, it predicts physically realistic asymptotic behavior, and like the Ehrenfest method, it allows continuous trajectory propagation (without hops) in regions of strong state interaction, making it more robust with respect to the choice of representation. Since the method is driven by the curvature of the adiabatic surfaces, it saves the cost of calculating exact nonadiabatic coupling vectors by electronic structure theory.

Dynamics calculations on fitted potential energy surface (PES) are orders of magnitude faster than direct dynamics, but accurate PES prediction is computationally very expensive for even small systems. Our group has developed a machine-learning method called diabatization by deep neural network (DDNN), which can provide learned adiabatic PESs from input points on adiabatic surfaces. However, a notorious drawback for machine-learned potentials is their unreliable behavior when applied to data quite different from that

used for training. In Chapter 4, we have developed a physics-based machine learning technique called parametrically managed diabatization by a deep neural network (PM-DDNN), enabling construction of analytical machine-learned smooth ground and excited state PES and extrapolation of the PES for O_3 outside the training region. The PES from PM-DDNN gives excellent results for collision dynamics of O + O_2 calculated with the *ANT* program.

In Chapter 5, we benchmarked and developed DFT datasets for studying the photodissociation of *o*-fluorothiophenol. In particular, we presented a combined Δ-learning method (using a higher-level and lower-level DFT dataset) and physics-based NN, called dual-level parametrically managed neural network (DL-PMNN), to obtain the 33-dimensional ground state PES, extrapolated the PES outside the training region, and validated the PES by running trajectories using the *SHARC-MN* program.

Table of Contents

List of Figures

List of Tables

Chapter 1 Introduction to Density Functional Theory and Computational Methods to Study Photochemistry

1.1 Density Functional Theory

In density functional theory (DFT) ground state energies are predicted using the electron density of a system. It was proposed by Hohenberg and Kohn (HK)[1] and Kohn and Sham (KS)[2] in 1960s. From the 1990s, the use of the method has grown exponentially. In addition to being computationally economical, it is powerful for calculating molecular properties like molecular structure, energies, vibrational frequencies, and reaction pathways. It is one of the most popular methods for solid state physics and computational chemistry. Walter Kohn was awarded the Nobel Prize in Chemistry in 1998 for his major contributions in developing DFT.[3] Three notable studies can be traced in the trail of development of DFT. First in 1927, the most basic form of DFT was proposed by Thomas[4] and Fermi[5], this is popularly known as Thomas-Fermi (TF) theory. The other two important studies are the developed forms of inspirational Thomas-Fermi theory put forward in the form of two papers[1,2], known as HK theorem and KS equation.

1.1.1 Hohenberg-Kohn theorem

Uniqueness: The basic lemma of the Hohenberg-Kohn (HK) theory is that ``the ground state density $n(\mathbf{r})$ of a bound system of interacting electrons in some external potential $v(\mathbf{r})$ determines the potential uniquely".[1]

Hohenberg-Kohn variational principle

The most significant property of an electronic ground state is the energy E which by means of wave function methods could either be calculated by the approximate solution of the Schrödinger equation $H\Psi = E\Psi$ or by using the Rayleigh-Ritz minimal principle,

$$E = \min_{\Psi}(\Psi, H\Psi) \tag{1}$$

where Ψ is the normalized trial wave function.

The HK variational principle was formulated using trial densities $n(\mathbf{r})$ rather than trial wave functions Ψ. Every trial wave function Ψ has a one-to-one correspondence to a trial density $n(\mathbf{r})$. For an N electron system, $n(\mathbf{r})$can be obtained as:

$$n(\mathbf{r}) = N \int \Psi^*(\mathbf{r}, \mathbf{r}_2, \dots, \mathbf{r}_N)\Psi(\mathbf{r}, \mathbf{r}_2, \dots, \mathbf{r}_N)\mathrm{d}\mathbf{r}_2 \dots \mathrm{d}\mathbf{r}_N \quad (2)$$

The minimization of Eq. (1) can be done in two steps using the constrained search method. described below. Firstly, a trial density $n(\mathbf{r})$ can be fixed and then a class α of trial wave functions having density $n(\mathbf{r})$ can be denoted as Ψ_n^α. Then the constrained energy minimum with the fixed $n(\mathbf{r})$ can be defined as:

$$\begin{aligned} E_\mathrm{v}[n(\mathbf{r})] &= \min_\alpha(\Psi_\mathrm{n}^\alpha, H\Psi_\mathrm{n}^\alpha) \\ &= \int v(\mathbf{r})n(\mathbf{r})d\mathbf{r} + F[n(\mathbf{r})] \end{aligned} \quad (3)$$

where

$$F[n(\mathbf{r})] = \min_\alpha[\Psi_n^\alpha, (T+U)\Psi_n^\alpha] \quad (4)$$

and T and U are the kinetic and the potential energy operators. $F[n(\mathbf{r})]$ is a universal functional of $n(\mathbf{r})$ and doesn't require any explicit knowledge of $v(\mathbf{r})$. Secondly, Eq. (3) can be minimized over all $n(\mathbf{r})$ as:

$$\begin{aligned} E &= \min_{n(\mathbf{r})} E_v\,[n(\mathbf{r})] \\ &= \min_{n(\mathbf{r})} \int v(\mathbf{r})n(\mathbf{r})d\mathbf{r} + F[n(\mathbf{r})] \end{aligned} \quad (5)$$

The minimum for a nondegenerate ground state is obtained when $n(\mathbf{r})$ is the density of the ground state. For a degenerate ground state, $n(\mathbf{r})$ is one of the densities. The best thing here is the transformation of the problem from a tough task of finding the minimum of $(\Psi, H\Psi)$ with respect to the $3N$-dimensional trial wave function Ψ to a seemingly more manageable problem of obtaining the minimum of $E_v[n(\mathbf{r})]$ with respect to the three-dimensional density $n(\mathbf{r})$. The total energy can then be written as a sum of kinetic energy, classical electrostatic energy and the energy of non-interacting electron moving under an external potential v as:

$$E[n(\mathbf{r})] = T[n(\mathbf{r})] + U[n(\mathbf{r})] + \int v(\mathbf{r})n(\mathbf{r})\mathrm{d}\mathbf{r} \quad (6)$$

The first two terms are not explicitly dependent on external potential v. It is possible now to derive the TF theory by making the approximations as:

$$T = \int \frac{3}{10} k_{\mathrm{F}}^2[n(\mathbf{r})]\mathrm{n}(\mathbf{r})\mathrm{d}\mathbf{r} \tag{7}$$

$$U = \frac{1}{2}\int\int \frac{n(\mathbf{r})n(\mathbf{r}')}{|\mathbf{r}-\mathbf{r}'|}\mathrm{d}\mathbf{r}\mathrm{d}\mathbf{r}' \tag{8}$$

where $k_{\mathrm{F}}(n)$ is the Fermi wave vector of a homogeneous electron gas of density $n(\mathbf{r})$ and represents the mean kinetic energy per electron of that system. The expression for U follows the classical approximation. Despite giving a method for calculating the energy using electron density, the HK theorem is hard to use for accurate work due to the difficulty in finding an accurate kinetic energy functional $T[n(\mathbf{r})]$.

1.1.2 Kohn-Sham equations

According to the Kohn-Sham (KS) theorem, if we can find the ground state electron density, then we can locate the lowest energy state of the system and hence, the ground state of the system. The theorem also provides a way of finding the true ground state electron density. It provides an expression that gave the ground state energy E as a functional of the electron density $n(\mathbf{r})$ as:

$$E[n(\mathbf{r})] = T[n(\mathbf{r})] + E_{\mathrm{ext}}[n(\mathbf{r})] + \frac{1}{2}\int\int \frac{\mathrm{n}(\mathbf{r})\mathrm{n}(\mathbf{r}')}{|\mathbf{r}-\mathbf{r}'|}\mathrm{d}\mathbf{r}\mathrm{d}\mathbf{r}' + E_{\mathrm{xc}}[n(\mathbf{r})] \tag{9}$$

where T refers to the kinetic energy of non-interacting electrons, E_{ext} refers to the energy due to the interaction between the electron and the external potential, the third term refers to the electron-electron electrostatic interaction energy and E_{xc} represents the non-classical exchange-correlation energy. The third and the fourth terms describe electron-electron interaction.

In the past, Hartree provided the self-consistent single particle equations[6] for making approximations in the electronic structure theory. Hartree considered every electron in an atom to be moving in an effective single-particle potential v_{H} given by

$$v_{\mathrm{H}} = -\frac{Z}{\mathbf{r}} + \int \frac{n(\mathbf{r}')}{|\mathbf{r}-\mathbf{r}'|}\mathrm{d}\mathbf{r}' \tag{10}$$

where the first term is the potential due to nucleus of atomic number Z, and the second term is the potential due to average electron density $n(\mathbf{r})$. Each electron follows the single particle Schrödinger equation

$$\left(-\frac{\hbar^2}{2m}\nabla^2 + v_{\mathrm{H}}(\mathbf{r})\right)\psi_i(\mathbf{r}) = \epsilon_i\psi_i(\mathbf{r}) \tag{11}$$

where ψ represents the single particle wave function, ϵ is the eigenvalue, i denotes spin and spatial quantum numbers, and the density is given by

$$n(\mathbf{r}) = \sum_{i=1}^{n} \psi_i^*(\mathbf{r})\psi_i(\mathbf{r}) \tag{12}$$

Coming to the case of interacting electrons, Kohn and Sham assumed the electrons to be non-interacting among themselves while calculating the kinetic energy T, motivated by the Hartree approximation. They ended up solving the Schrödinger's equation of electrons which are moving in an effective potential $v_{\mathrm{eff}}(\mathbf{r})$

$$\left(-\frac{\hbar^2}{2m}\nabla^2 + v_{\mathrm{eff}}(\mathbf{r})\right)\psi_i(\mathbf{r}) = \epsilon_i\psi_i(\mathbf{r}) \tag{13}$$

where $v_{\mathrm{eff}}(\mathbf{r})$ is given by

$$v_{\mathrm{eff}}(\mathbf{r}) = v(\mathbf{r}) + v_{\mathrm{xc}}(\mathbf{r}) + \int \frac{n(\mathbf{r}')}{|\mathbf{r}-\mathbf{r}'|}\,\mathrm{d}\mathbf{r}' \tag{14}$$

and the exchange-correlation potential $v_{\mathrm{xc}}(\mathbf{r})$ is expressed as

$$v_{\mathrm{xc}}(\mathbf{r}) = \frac{\delta E_{\mathrm{xc}}[n(\mathbf{r})]}{\delta n(\mathbf{r})} \tag{15}$$

The total energy of the system can be expressed as

$$E[n] = \sum_{i=1}^{n} \epsilon_i - \frac{1}{2}\int\int \frac{n(\mathbf{r})n(\mathbf{r}')}{|\mathbf{r}-\mathbf{r}'|}\,\mathrm{d}\mathbf{r}\mathrm{d}\mathbf{r}' + E_{\mathrm{xc}}[n(\mathbf{r})] - \int \frac{\delta E_{\mathrm{xc}}[n(\mathbf{r})]}{\delta n(\mathbf{r})} n(\mathbf{r})\mathrm{d}\mathbf{r} \tag{16}$$

where the ϵ_i is the i^{th} eigenvalue of non-interacting single particle equation as shown in Eq. (11). In DFT, the practicality depends on the accuracy of the exchange-correlation functional.

1.1.3 Exchange-correlation functionals

We must know the exact form of the exchange-correlation functional if we want to use the KS equations to get the exact energy. However, it is practically impossible to know the exact form of this functional. After the development of DFT, several approximations have been made for exchange-correlation functionals. One of the ways for categorizing various exchange-correlation functionals is to follow `Jacob's ladder' proposed by Schmidt and Perdew. In "Jacob's ladder"[7] as shown in Figure 1, the functionals are arranged from bottom to top in the order of increasing complexity. At the bottom, there is the Hartree approximation and at the top, there is the exact exchange-correlation functional.

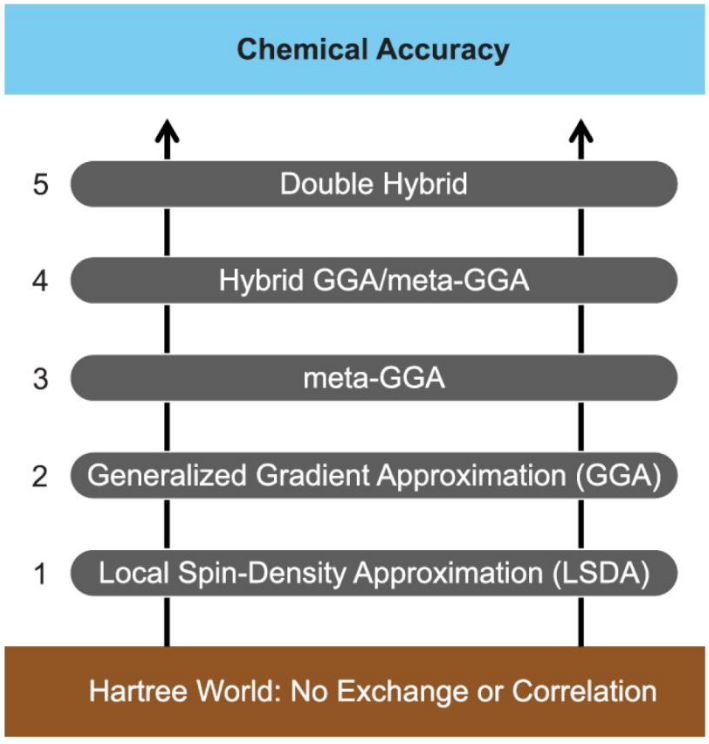

Figure 1: Scmidt and Perdew's "Jacob's Ladder"

Here, we discuss some of the rungs of the ladder to introduce the varied class of exchange-correlation functionals:

a) Local spin-density approximation (LSDA): LSDA occupies the first rung of `Jacob's ladder'. To understand, we need to understand local-density approximation (LDA). LDA is the simplest of all the approximations and the exchange-correlation energy functional is represented as:

$$E_{\mathrm{xc}}^{\mathrm{LDA}}[n] = \int n(\mathbf{r}) e_{\mathrm{xc}}\big(n(\mathbf{r})\big)\mathrm{d}\mathbf{r} \tag{17}$$

where $e_{\mathrm{xc}}\big(n(\mathbf{r})\big)$ is the exchange-correlation energy density of uniform electron gas of density $n(\mathbf{r})$. The exchange-correlation energy can be written as the individual sum of the exchange and correlation energy as

$$E_{\mathrm{xc}}^{\mathrm{LDA}}[n] = E_{\mathrm{x}}^{\mathrm{LDA}}[n] + E_{\mathrm{c}}^{\mathrm{LDA}}[n] \tag{18}$$

where the exchange energy is given by

$$E_{x}^{\mathrm{LDA}}[n] = C \int n^{\frac{4}{3}}(\mathbf{r})\mathrm{d}\mathbf{r} \tag{19}$$

where C is a fixed coefficient, and the correlation energy can be found by fitting to the works of Gell-Mann and Brueckner,[8] Ceperly and Alder,[9] or other workers. The various LDA functionals differ in the way the correlation energy is fitted to the free-electron gas data. From the formulation, it follows that the LDA is valid for systems where the density varies slowly. PW[10] and VWN[11] are some of the commonly used LDA functionals. LDA approximations that treat the densities of the α and the β electrons separately are called LSDA. One example of an LSDA is the GPWL[12] functional.

b) Generalized gradient approximation (GGA): These functionals sit at the second rung of “Jacob's ladder” andbring into account the gradient of density $\nabla n(\mathbf{r})$ along with density $n(\mathbf{r})$. The exchange-correlation energy E_{xc} can thus be represented as

$$E_{xc}^{GGA} = \int n(\mathbf{r}) e_{\mathrm{xc}}(n(\mathbf{r}), |\nabla n(\mathbf{r})|)\mathrm{d}\mathbf{r} \tag{20}$$

Most GGA functionals are formed by imposing some correction term to the LDA functionals. The exchange-correlation energy is calculated as the sum of the exchange and the correlation energy in terms of the electron density and gradient of the electron density. GGA usually yield better results than LDA. Some of the most widely used GGA functionals are PBE[13] and PW91.[14,15]

c) Meta-GGAs: They occupy the third rung of "Jacob's ladder". The second derivative of the density $\nabla^2 n(\mathbf{r})$ is considered. However, due to numerical issues, instead of the $\nabla^2 n(\mathbf{r})$, the kinetic energy density $\tau(\mathbf{r})$ is considered, which is represented as:

$$\tau(\mathbf{r}) = \sum_i \frac{1}{2} |\nabla \phi_i|^2 \qquad (21)$$

Some of the common meta-GGAs include TPSS,[16] M06-L,[17] and revM06-L.[18] TPSS provides better molecular properties for gas phase systems. For main group and transition metal thermochemistry, kinetics, and noncovalent interactions, M06-L is widely used. The revM06-L functional is a reparametrized version of M06-L and it has better across-the-board accuracy and more computational stability for chemical problems. Another meta-GGA that improves the structure and energetics of diversely bonded materials is SCAN.[19]

d) Hybrid functionals: They are the fourth generation of the exchange-correlation functionals. They include some portion of the Hartee-Fock (HF) exchange while calculating the exchange correlation energy. GGA functionals with HF exchange are called hybrid GGA functionals. B3LYP[20] is a hybrid GGA functionals that uses LSDA exchange and correlation, B88 exchange, the LYP correlation functional and HF exchange. MPW1K[21] is another popular hybrid GGA. Meta-GGA functionals with HF exchange are called hybrid meta-GGA functionals. Some examples of hybrid meta-GGA functionals are TPSSh,[16] PW6B95D3,[22] M06,[23] M06-HF,[24] and M11.[25] Hybrid functionals sometimes perform better than LDA and GGA for calculation of gas-phase properties and band gaps in solids.

Some other functionals not included in the “Jacob's ladder” are nonseparable gradient approximation (NGA) and meta-NGA functionals. NGA depends on the same parameters as GGA but differs from GGA in the sense that it does not calculate the exchange and the correlation energy separately. A widely used NGA functional is GAM[26] which is designed to provide better values for parameters relevant for homogeneous catalysis. Just like GGA, if the orbital dependent kinetic energy density is included in an NGA, it yields a meta-NGA. Some popular meta-NGAs for atoms and molecules are MN15.[27] MN15-L.[28] CF22D[29] is a relatively new singly hybrid functional which combines a global hybrid meta-NGA with a damped dispersion term. It has very good performance on thermochemistry, barrier heights, noncovalent interactions, and other properties. There are some functionals that consider the van der Waals dispersion interactions for more accurate modeling. A popular functional designed not only to describe bond breaking and formation in solid state physics and chemistry, but also to include van der Waals dispersion interactions is BEEF-vdW.[30]

1.1.4 Density Functional Theory for Controlled C-H bond activation

Shale gas is an inexpensive and abundant source of small alkanes. They can be transformed into valuable oxygenates. But the chemical inertness of these compounds makes it hard to activate the C-H bond while trapping the partially oxidized products from overoxidation to more thermodynamically favorable products. In nature, copper- and iron-based methane monooxygenases (pMMO and sMMO) perform this transformation by activating dioxygen and methane molecules under ambient conditions for the direct and selective conversion of methane to methanol.[31,32] Immense efforts have been dedicated to developing bio-inspired heterogeneous catalysts to accomplish this in a nonliving context, and Cu-based materials turned out to be attractive due to their capability of using dioxygen as a terminal oxidant. In heterogeneous catalysis, an increasing number of studies show the structural flexibility of the Cu-based active moieties including monomer, dimer, trimer, and small clusters.[33,34,35,36,37,38,39,40,41] Reactions are typically carried out in a stepwise fashion involving catalyst oxidation, methane activation, and methanol extraction. The

physical separation of methane and oxidant streams, and the strong methanol binding on the active sites, serves to inhibit overoxidation. Despite the efforts to study Cu-based methane oxidation, there has been no consensus thus far about the actual structure of the active site(s) or the mechanism(s). The difficulty of answering open questions is mainly due to (1) formation of non-uniform catalytic motif due to structurally ill-defined metal oxide and zeolite supports, (2) consequential ambiguity of the transition state structure, (3) minimal understanding of why, in many cases, only a fraction of deposited catalysts are active for the reaction, and (4) a vast number of tunable variables during the material synthesis and catalysis hindering conclusive insights from a direct comparison of published results. These factors pose a great challenge in identifying comprehensive structure–activity relationships that allow fundamental understanding of the chemistry occurring at the catalytic sites.

DFT is one of the most widely used methods for structural and mechanistic studies of chemical reactions in heterogeneous catalysis. DFT has been a powerful tool for interpretation of a vast amount of experimental data, and in the discovery of new structures and functionalities of new materials.[42,43,44] DFT is mostly used to predict the energies of reaction and the barrier heights of reactions, the qualities which guide the determination of possible reaction mechanisms and can provide insights in designing better catalysts.

In Chapter 2, we propose a class of highly crystalline and porous metal−organic frameworks (MOFs) called zeolitic imidazolate frameworks (ZIFs) to de-convolute the above complications.

1.1.4.1 Zeolitic imidazolate frameworks

ZIFs are a class of MOFs. A MOF is a porous crystalline species made up of an inorganometallic node and an organic-base linker (Figure 2).The nodes and the linkers can be changed to tune the structure of a MOF, and to tune properties essential to catalyze different reactions. ZIFs are topologically isomorphic with zeolites and are made up of tetrahedrally coordinated transition metal ions connected by imidazolate linkers.

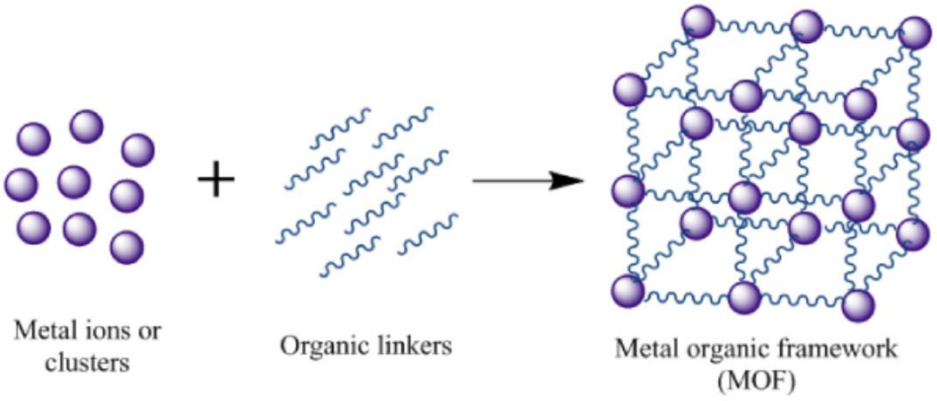

Figure 2: Representation of metal-organic framework (MOF)

MOFs are increasingly regarded as promising model supports for the development of bio-inspired, single-site catalysts with a tailored coordination environment.[45,46,47,48,49] Mononuclear metal ions, as well as metal oxide clusters with uniform structural characteristics can be directly incorporated into the secondary building units (SBUs) during synthesis,[50,51,52,53] anchored onto the nodes, organic linkers, or non-structural modifiers *via* post-synthetic modification,[54,55,56,57,58] or confined inside the pores *via* host-guest interactions.[59,60,61,62] Several successes of MOF-supported copper-oxo clusters for selective methane oxidation have been reported.[63,64,65] The high tunability and structural rigidity of MOFs make it promising to functionally mimic pMMO by anchoring Cu ions into an N-rich environment with a desired configuration. ZIF-8 ($Zn(mim)_2$, also known as MAF-4) is a highly hydrophobic MOF with excellent chemical and thermal stability. The framework contains large cavities (~11.7 Å) interconnected by narrow windows (~3.4 Å for the 6-membered ring and 0.8 Å for the 4-membered ring; see Figure 3).[66,67] Owing to its structural flexibility, gas molecules like N_2 and CH_4 with kinetic diameters of 3.6 and 3.8 Å, respectively, can be adsorbed within the interior of the framework.[68,69,70] Owing to their higher affinity to the organic linkers, catalytically active single metal ions can be introduced into the framework in place of the tetrahedral Zn(II) atoms.

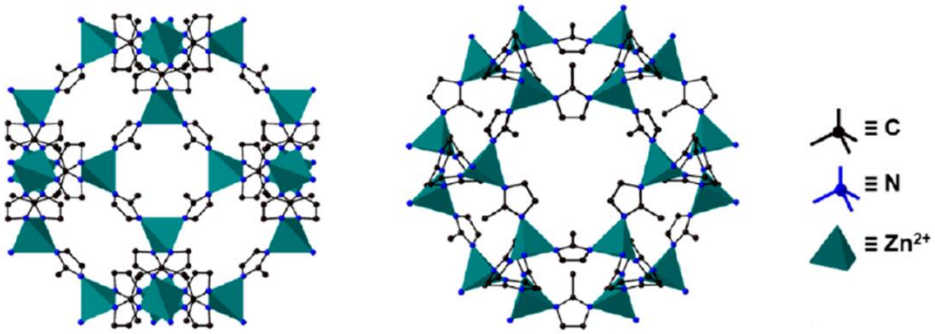

Figure 3: Structure of ZIF-8 with the 4-membered ring viewed along the crystallographic a axis (left) and the 6-membered ring viewed along [111] direction (right).

In Chapter 2, we demonstrate that an enzyme-like mononuclear Cu(II) site can be created inside a zeolitic imidazolate framework, ZIF-8 ($Zn_xCu_{1-x}(mim)_2$, where mim^- is 2-methylimiazolate). The resulting materials, featuring a sodalite topology, are capable of stepwise methane oxidation to partially oxygenated products, with methanol and formaldehyde as the major products. Overoxidation can be completely suppressed such that all products are the ones partially oxygenated. Structural evolution of the active sites was uncovered *via* X-ray absorption spectroscopy and its potential correlation with the evolved reactivity is discussed. We also performed calculations on the mechanistic study of methane oxidation using density functional theory (DFT).

Photochemistry is very important as it tracks down the origin of life, photosynthesis, and the production of essential vitamins. We need quantum mechanical methods which are accurate as well as computationally affordable.

1.2 Direct Dynamics

In direct dynamics, instead of using pre-parameterized analytic functions for energies and couplings, all necessary energies, forces, and couplings for important geometries are directly obtained from electronic structure calculations during the molecular dynamics simulation. Semiclassical methods for classical or quasiclassial molecular dynamics that involves coupled electronic states require a blending of quantum mechanics for the electronic motions with classical or quasiclassical trajectories for the nuclear motions.[71,72,73] There are five types of methods, which differ in their treatment of electronic decoherence. Decoherence refers to the tendency of the time-evolved density matrix to represent a statistical ensemble of states rather than a coherent superposition of wave packets.

1.2.1 Trajectory Surface Hopping

The first general method for treating non-Born-Oppenheimer trajectories is trajectory surface hopping (TSH). In this approach, individual trajectories propagate independently on a potential energy surface (PES) with occasional hops or switches from one surface to another. Tully's fewest switches (TFS) method[74] is one of the most successful of the TSH methods. One can visualize these methods as modeling the accurate time-dependent wave packet by a collection of independent trajectories evolving on different electronic surfaces. Each trajectory stochastically hops between electronic surfaces based on an electronic density matrix that is unique to each trajectory. This density matrix is determined by coherently propagating the solution to the time-dependent electronic Schrödinger equation along the classical trajectory. Differences in the electronic density matrices of two trajectories in the ensemble arise for two reasons: (1) the trajectories have different initial positions and/or momenta, and (2) they hop at different times along their paths. The ensemble-averaged electronic density matrix, which can be

compared to the exact quantum mechanical electronic density matrix, decoheres[75] (i.e., the off-diagonal elements systematically approach zero) due to these factors: the initial wave packet's width and the divergence of trajectories in phase space because of surface hops. Importantly, the electronic density matrix for each individual trajectory remains fully coherent; decoherence only emerges when averaging over the entire ensemble due to the two sources mentioned above.

1.2.2 Self-Consistent Potential Methods

The second broad category of methods involves self-consistent potential (SCP) approaches, in which the nuclei propagate on a time-dependent PES, influenced by the current quantum mechanical electronic density matrix. The simplest form of this method is the semiclassical Ehrenfest (SE) approach,[76,77,78] and more advanced versions include the mean field with surface hopping (MF/SH) method[79] and the self-consistent decay of mixing (SCDM) algorithm.[80] The SE method uses an ensemble of trajectories, incorporating some decoherence due to the initial wave packet spread. However, for each trajectory in the ensemble, the electronic density matrix is propagated with full coherence, like the TSH method. SE trajectories are influenced by all electronic states simultaneously, based on the electronic state density matrix, without hopping between states, which keeps each trajectory fully coherent. In cases where a single region of strong coupling is rapidly traversed, fully coherent nuclear motion is expected, making the SE approach reasonable. However, the lack of decoherence can result in nonphysical behavior in asymptotic regions of the simulation—where coupling is small or absent—as the system moves from reactants to products. This is different from the TSH method, which produces more realistic asymptotic behavior but may be less accurate in describing strongly coupled states.

The SCDM method integrates the physical asymptotic behavior characteristic of TSH methods into a SCP framework. Decoherence, which is previously considered as an effect of ensemble averaging is directly incorporated into the equations of motion for each individual trajectory in an averaged manner, while still propagating each of the trajectories

independently. This adjustment yields a trajectory like those in the SE method but with correct limiting behavior.

1.2.3 Coherent-Passage Methods

TSH methods can also be refined by enhancing their coherence, leading to a class of approaches referred to as coherent passage methods. In these methods, a trial classical path with continuous momenta is used to evolve the system through a region of strong coupling while treating the electronic density matrix fully coherently—without surface hopping or decay of mixing. The electronic transition probabilities from this coherent evolution are then used to determine the outcome of the trajectory, though subsequent passages through this or other strong interaction regions are not treated as coherent with previous ones. Thachuk, Ivanov, and Wardlaw[81] have demonstrated the importance of decoherence between successive passages through strong coupling regions in a low-dimensional problem involving the evolution of a two-state diatomic molecule in a strong electromagnetic field. Their work highlights the significance of balancing coherent evolution through strong coupling regions with decoherence between such passages, which is also relevant in more general cases, though their specific algorithm is not universally applicable. Their findings underscore the potential errors that can arise if coherence is maintained over an entire trajectory .One classical path method inspired by these considerations is the surface hopping method developed by Parlant and Gislason,[82,83] This method addresses some of the decoherence that occurs in other TSH methods due to surface hops in strongly coupled regions, as well as the errors identified by Thachuk, Ivanov, and Wardlaw[81] arising from treating successive passages coherently. Parlant and Gislason called their approach the "exact" surface hopping scheme because it employs the exact time-dependent electronic Schrödinger equation for each complete passage through a region of strong coupling. To avoid confusion with other methods that also use the exact time-dependent Schrödinger equation, and their approach can be referred to as "exact complete passage" trajectory surface hopping (ECP-TSH).

1.2.4 Coupled-Trajectory Schemes

The methods discussed thus far are independent trajectory methods. Another approach involves coupled trajectories, where a swarm of trajectories is evolved simultaneously, with the entire electronic state density matrix influencing the motion of each trajectory. This approach is compelling, as it recognizes that it is the ensemble of trajectories, not individual phase points, that should be interpreted when extracting quantum mechanical transition probabilities from classical mechanics. Notable coupled-trajectory methods include the quantum/classical Liouville methods developed by Martens[84,85] and others, and the full multiple spawning method.[86,87] Like SCDM, these methods explicitly account for dynamical decoherence, but they are more complex than independent-trajectory methods and require significantly more computational effort to fully sample the extended phase space of nuclear coordinates, momenta, and electronic probability amplitudes.

In the context of TSH, the TFS surface hopping scheme allow hops even within a single passage through a strong coupling region, while in the context of SCP, the SCDM scheme permits some decay of mixing at all points along the trajectory, including for the equations governing the probability of switching between decoherent states. As a result, these methods do not adhere to the coherent passage framework. Decoherence can be introduced into trajectory surface hopping, and this does improve the method. However, it cannot be incorporated in a fully consistent manner when propagating on individual surfaces, as surface hopping does, rather than on effective surfaces determined by the density matrix.

1.2.5 Coherent Switching with Decay of Mixing

A more consistent approach for adding decoherence to electronically nonadiabatic dynamics is the coherent switching with decay of mixing (CSDM) method,[88] which can be seen as an implementation of the Liouville–von Neumann equation, the correct equation for quantum mechanical propagation of a subsystem's density matrix. The state to which the system decoheres is referred to as the "pointer state" or "decoherent state". While TSH

involves coherent propagation of a trajectory on a single potential energy surface, with stochastic switching between surfaces, CSDM combines coherent and incoherent propagation on a self-consistent potential while switching the pointer state. The CSDM algorithm draws on the strengths of both semiclassical Ehrenfest and TSH. Like TSH, it predicts physically accurate asymptotic behavior, and like the Ehrenfest method, it allows continuous trajectory propagation (without hops) in regions of strong interaction, making it more robust with respect to the choice of representation.

1.2.6 Curvature Driven TSH, SE, and CSDM

As we know, in direct dynamics, all necessary energies, forces, and couplings for important geometries are directly obtained from electronic structure calculations during the dynamics simulation. These calculations provide electronically adiabatic wave functions ϕ, and the couplings in semiclassical calculations within the adiabatic representation are determined by the nuclear momentum operator. This involves matrix elements of the gradient with respect to nuclear coordinates[89,90], denoted as:

$$\mathbf{d}_{IJ} = \langle \phi_I | \partial / \partial \mathbf{R} | \phi_J \rangle \tag{22}$$

where $\langle ... | ... | ... \rangle$ denotes the electronic matrix element. This matrix element, often called the nonadiabatic coupling (NAC), is a $3N$-dimensional vector, where N is the number of atoms.

In semiclassical methods, electronic wave functions can also be considered time-dependent because:

$$\phi_I = \phi_I\big(\mathbf{r}; \mathbf{R}(t)\big) \tag{23}$$

where $\mathbf{r}$ represents the electronic coordinates, and $\mathbf{R}(t)$ is the nuclear trajectory. A popular semiclassical method is TSH, where only the NAC in the direction of the current velocity $\dot{\mathbf{R}}$ is needed. Thus, the semiclassical equations only require the time-derivative coupling (TDC):

$$\sigma_{IJ} = \langle \phi_I | \mathrm{d}/\mathrm{d}t | \phi_J \rangle = \langle \phi_I | \partial / \partial \mathbf{R} | \phi_J \rangle \cdot \dot{\mathbf{R}} \tag{24}$$

Direct calculation of the TDC is more efficient than calculating the full NAC and provides more accurate numerical integration of TSH equations of motion, especially in cases of trivial crossings.[91,92,93,94] More comprehensive semiclassical methods, like SE dynamics and CSDM dynamics, require all components of the NAC. Since time-derivative evaluations are more efficient, an effective NAC[95] derived from the TDC is formulated, which can be used for SE and CSDM dynamics without full NAC calculations. Tests have shown that using this effective NAC does not introduce significant errors, leading to efficient calculations of TSH, tSE, and tCSDM without requiring NAC computations from electronic structure software. The effective NAC is particularly useful for new or high-level electronic structure methods where NACs may not be available, such as in configuration interaction without state-specific self-consistent orbitals,[96] coupled cluster theory,[97,98] or multiconfiguration pair-density functional theory.[99] Similarly, NACs are often unavailable for machine-learning-based energy calculations. Thus, it would be highly convenient to have approximate NACs that can be derived from energies and energy derivatives. The paper by Shu and Truhlar[100] introduces new algorithms for nonadiabatic dynamics that approximate the TDC and effective NAC from energy curvature (shown in Figure 4).

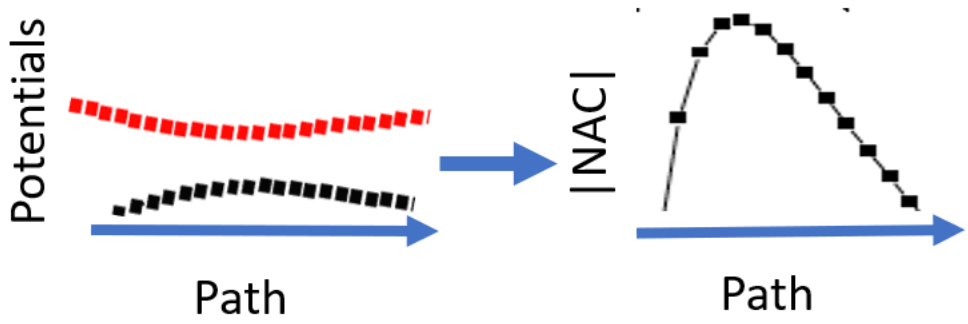

Figure 4: Effective NAC from curvature of energy

They developed new variants of tSE and tCSDM, called curvature-driven semiclassical Ehrenfest (κSE) and curvature-driven coherent switching with decay of mixing (κCSDM). Both methods require only energy and gradient information from electronic structure

calculations. The curvature-approximated TDC is an extension of a previously developed NAC approximation for one-dimensional systems by Baeck and An (BA).[101]

$$\mathbf{d}_{IJ}^{BA} = \langle \phi_I | \mathrm{d}/\mathrm{d}q | \phi_J \rangle \simeq \frac{1}{2}\left[\frac{\mathrm{d}^2(V_I - V_J)}{\mathrm{d}q^2}\frac{1}{V_I - V_J}\right]^{\frac{1}{2}} \tag{25}$$

The CSDM algorithm, based on SE, incorporates non-Markovian decoherence and stochastic pointer-state switches. It retains the advantages of SE's self-consistent potential and robustness, while sharing TSH's ability to stochastically switch to physical final states without discontinuous nuclear momenta. Most importantly, CSDM balances coherence in strong interaction regions with decoherence between them, consistent with the Liouville–von Neumann equation. CSDM has been successfully applied to spin-conserving processes and, more recently, to intersystem crossing processes. To generalize this approach for time dependence, they approximated the one-dimensional time derivative for the TDC, which allows the use of κSE, κCSDM, and κTSH. Since eq (25) represents the one-dimensional derivative with respect to a coordinate in the direction of motion, they extended this concept to a one-dimensional derivative with respect to time:

$$\kappa\mathrm{TDC} \equiv \sigma_{IJ}^{\kappa} = \langle \phi_I | \mathrm{d}/\mathrm{d}t | \phi_J \rangle \simeq \frac{1}{2}\left[\frac{\mathrm{d}^2(V_I - V_J)}{\mathrm{d}t^2}\frac{1}{V_I - V_J}\right]^{\frac{1}{2}}, \text{for } I > J \tag{26}$$

where $(V_I - V_J)$ is the positive local gap between adiabatic potential surfaces. We introduce κ both as a prefix and a superscript to indicate the approximation based on the curvature of the gaps. The use of eq (26) for the TDC is a key feature of κSE and κCSDM. This approach can also be applied to Tully's surface hopping (TSH), yielding κTSH. They have implemented κSE, κCSDM, and κTSH in a new version of SHARC-MN.[102] In this work, the authors introduced a curvature-based TDC approximation and demonstrated how this approximation can be used to derive curvature-driven versions of TSH, the SE method, and the CSDM method for nonadiabatic dynamics. The curvature-based methods, denoted κTSH, κSE, and κCSDM, were tested on ethylene, where results from κCSDM and κTSH-EDC closely matched those from CSDM and TSH-EDC. These curvature-based methods

eliminate the need to compute NAC vectors or time derivatives of the wavefunction n, offering a computational advantage.

In Chapter 2, we employ κCSDM to investigate the nonadiabatic ring-opening dynamics of the 1,3-cyclohexadiene (13CHD) molecule. We have three main goals: (1) to demonstrate the high accuracy and efficiency of the κCSDM algorithm; (2) to optimize the widely discussed conical intersections that mediate the excited-state reaction with dynamic correlation at the level of XMS-CASPT2; (3) to see if the reaction can be well simulated by including only valence states, without including the interleaving Rydberg states, which members of our group have studied[103] previously.

1.3 Fitting of Potential Energy Surfaces

The other way of studying photochemistry is fitting PESs. Dynamics calculations on PESs are orders of magnitude faster than direct dynamics, but accurate PES prediction is computationally very expensive for even small systems.

1.3.1 DDNN

To calculate electronically nonadiabatic dynamics, it is essential to understand state-specific potential energy surfaces and their couplings. This can be achieved using either the adiabatic or diabatic representations. In the adiabatic representation, potential energy surfaces exhibit cuspidal ridges at conical intersections, and the couplings form $3N$-dimensional vectors (where N is the number of atoms) that become singular at these intersections. Conversely, the diabatic representation provides smoother potential energy surfaces and couplings, with couplings represented as scalars.[104,105] Here, the potential energy surfaces and couplings are the diagonal and off-diagonal elements of a diabatic potential energy matrix (DPEM). The adiabatic representation is less suitable for fitting potential energies and couplings to analytic functions, leading to the use of direct dynamics in this representation. This approach requires electronic structure calculations at each step to compute energies, gradients, and couplings (possibly Hessians), making it computationally demanding. By contrast, the diabatic representation is more efficient for

fitting, and the use of resulting fits enables longer simulations and enhanced ensemble averaging. However, using a DPEM necessitates diabatization, because accurate surfaces and couplings typically become available in the adiabatic representation. Often adiabatic-equivalent DPEMs are preferred, which are constructed so that diagonalizing them reproduces the original adiabatic potential energy surfaces. To achieve this, the DPEM elements must be sufficiently smooth to approximate adiabatic couplings through a similarity transformation.

Numerous diabatization techniques exist. A notable method[106] identifies diabatic molecular orbitals and uses system-specific configuration state functions based on these orbitals. The paper by Shu and Truhlar[107] introduces a new machine-learning-based diabatization method that bypasses the need for diabatic molecular orbitals or orbital information. While good adiabatic potentials are still necessary initially, established methods for obtaining these exist. This method does not require couplings from the original adiabatic calculations, relying solely on energy data. Diabatization by ansatz, neural networks[108] have previously been applied in similar contexts. In the approach by Shu and Truhlar[107], the input comprises adiabatic energies and selected DPEM elements at specific geometries where diabatic states are assumed to be known. This is achieved by: (1) assuming the DPEM is diagonal, such as at the equilibrium structure of a closed-shell singlet molecule or photodissociation products, or (2) performing a lower-dimensional diabatization and extrapolating results to higher-dimensional spaces. It is important to note that diabatization is non-unique since a strictly diabatic solution does not exist for real molecules. Any transformation that minimizes coupling from nuclear momentum and kinetic energy—compared to scalar coupling from the electronic Hamiltonian—is valid. A well-suited DPEM will have smooth elements, allowing easy back-transformation to the adiabatic representation if needed, along with straightforward calculation of adiabatic couplings.

Machine learning in chemistry and physics is growing rapidly, with early methods including semiempirical quantum chemistry parameterizations to fit potential energy surfaces. Recently, deep neural networks (DNNs), also called multilayer perceptrons (MLPs), have become valuable tools. Composed of layers of nodes that are weighted, biased, and activated to form the next layer,[109,110] DNNs can model flexible functions for accurate predictions.

The work by Shu and Truhlar[106] proposes a new DNN architecture for diabatization, named the diabatization by deep neural network (DDNN) method, which can compute an adiabatic-equivalent DPEM from adiabatic potential energy surfaces without requiring orbital or coupling data from the original calculations. DDNN leverages the flexibility of diabatic states to align them with adiabatic states in regions where adiabatic behavior is expected. Additionally, it incorporates diabatic results from preliminary lower-dimensional cuts as constraints. In both scenarios, the input consists of adiabatic energies and selected geometries where diabatization is enforced, while the output is a set of analytically fitted DPEMs. This method is especially effective for photochemical studies. If smooth DPEM fits are achieved near conical intersections, where diabatic surfaces intersect and diabatic coupling vanishes, diagonalizing the DPEM will reveal the correct conical intersection topology. Compared to traditional diabatization techniques, DDNN offers a significant advantage in fitting accurate coupled surfaces. Traditional methods determine diabatic states to generate points on a global DPEM, followed by element fitting. Accurate adiabatic energy differences require consistent, precise fits of both diabatic potentials and couplings, which can be challenging. DDNN simplifies this process by using adiabatic energies as the objective during the simultaneous DPEM fitting, eliminating the need for separate, consistent element fits.

However, a notorious drawback for machine-learned potentials is their unreliable behavior when applied to data quite different from that used for training. For example, it's easy for neural-network potentials to acquire unphysical holes or unphysical barriers and/or

to have the wrong asymptotic behavior. Maintaining physical behavior in regions where one or more interatomic distance is very large or very small is hard because one does not usually saturate such regions of space with training data. When poor physical behavior arises, one often resorts to an iterative scheme: fit the surfaces, run trajectories to discover regions of space where the fit is unphysical, add data in the problematic regions, refit, and iterate the steps until no more unphysical behavior is found. However, this is problematic for maintaining physical behavior at large internuclear separation because the amount of space in asymptotic regions is infinite. And it can be troublesome in regions where two or more atoms get very close because the potential is very steep in those regions.

In Chapter 4, we introduce a new step in the machine-learning procedure, namely, a parametrically managed activation function. This is designed so that the potential representation in difficult regions inherits the correct physical behavior of lower-dimensional potentials. We introduce the parametrically managed activation function (PMAF) in the context of the methods of diabatization by deep neural network (DDNN) and permutationally restrained DDNN (PR-DDNN), but the type of approach employed here should also be useful for other uses of neural networks to represent potential energy surfaces. In Chapter 4, we talk about the relevant aspects of the DDNN and PR-DNN schemes, we present our new method named parametrically managed diabatization by deep neural network (PM-DDNN), and we illustrate the new method by using it to obtain improved potential energy surfaces for O + O_2 collisions in the $^3A'$ electronic state manifold.

In Chapter 5, we apply a more powerful version of the method described in Chapter 4 to a larger and more complex system, namely *ortho*-fluorothiophenol (*o*-FTP). The fluorine atom of *o*-FTP introduces a new issue that does not occur in thiophenol because the fluorine atom can form a hydrogen bond with the hydrogen atom of the SH group.[111] In Chapter 5, we present a dual-level parametrically managed neural network (DL-PMNN) to represent the ground-electronic-state potential energy surface of *o*-FTP by using use an energy-and distance-dependent PMAF to guides a higher-level NN fit by using a PMAF with a lower-

level electronic structure method. We illustrate the DL-PMNN methods by running trajectories to observe the dissociation of S-H bond in *o*-FTP.

1.4 Theme of the Thesis

My Ph. D. thesis focuses on modeling heterogeneous catalysis and developing methods for quantum mechanical photochemistry. In Chapter 2, we have modeled several active sites of Cu(II) defect site in ZIF-8, and the mechanistic pathways for catalysis of methane to methanol through DFT calculations in Gaussian, through enzyme biomimicking, enabling the identification and validation of the material for controlled C-H bond activation. There are two ways of studying photochemistry: Direct Dynamics and PES Fitting. For direct dynamics, we have developed and implemented the most computationally inexpensive version of curvature-driven coherent switching with decay of mixing dynamical method ($\boldsymbol{\kappa}$CSDM) in *SHARC-MN*[112] and achieved correct excited state nonadiabatic dynamics of the ring-opening of 1,3-cyclohexadiene, which is presented in Chapter 3. For PES fitting, in Chapter 4, we have developed a physics-based machine learning technique called PM-DDNN in PyTorch, enabling construction of analytical machine-learned smooth ground and excited state PES and extrapolation of the PES for O_3 outside the training region. The PES from PM-DDNN gives excellent results for collision dynamics of $O + O_2$ calculated with *ANT*.[113] In Chapter 5, we benchmarked and developed DFT datasets for studying the photodissociation of *o*-fluorothiophenol. In Chapter 5, we have presented a combined Δ-learning (using a higher and lower level DFT dataset), and physics based NN developed in TensorFlow, called DL-PMNN, to obtain the 33D ground state PES, extrapolated the PES outside the training region, and validated the PES by running trajectories in *SHARC-MN*[112].

Bibliography

[1]Hohenberg, P.; Kohn, W. Inhomogeneous electron gas. *Phys. Rev.* **1964**, *136*, B864.
[2]Kohn, W.; Sham, L. J. Self-consistent equations including exchange and correlation effects. *Phys. Rev.* **1965**, *140*, A1133.
[3]Kohn, W. Nobel Lecture: Electronic structure of matter-wave functions and density functionals. *Rev. Mod. Phys*. **1999**, *71*, 1253

[4]Thomas, L. H. The calculation of atomic elds. *Mathematical Proceedings of the Cam bridge Philosophical Society.* **1927**; pp 542548.
[5]Fermi, E. Atti Accad. Naz. Lincei, Cl. *Sci. Fis. Mat. Nat.* **1927.**
[6]Hartree, D. R. The wave mechanics of an atom with a non-Coulomb central eld. Part I. Theory and methods. *Math. Proc. Camb. Philos. Soc* **2008**, *24*, 89110.
[7]Perdew, J. P.; Schmidt, K. Jacobs ladder of density functional approximations for the exchange-correlation energy. *AIP Conf. Proc*. **2001**; pp 120.
[8]Gell-Mann, M.; Brueckner, K. A. Correlation energy of an electron gas at high density. *Phys. Rev.* **1957**, *106*, 364.
[9]Ceperley, D. M.; Alder, B. J. Ground state of the electron gas by a stochastic method. *Phys. Rev. Lett.* **1980**, *45*, 566.
[10]Perdew, J. P.; Wang, Y. Accurate and simple analytic representation of the electron-gas correlation energy. *Phys. Rev. B: Condens. Matter Mater. Phys.* **1992**, *45*, 13244.
[11]Vosko, S. H.; Wilk, L.; Nusair, M. Accurate spin-dependent electron liquid correlation energies for local spin density calculations: a critical analysis. *Can. J. Phys.* **1980**, *58*, 1200 1211.
[12]Gaspar, R. Uber eine approximation des Hartree-Fockschen potentials durch eine uni verselle potential funktion. *Acta Phys. Acad. Sci. Hung.* **1954**, *3*, 263286.
[13]Perdew, J. P.; Burke, K.; Ernzerhof, M. Generalized gradient approximation made simple. *Phys. Rev. Lett.* **1996**, *77*, 3865.
[14]Perdew, J. P.; Chevary, J. A.; Vosko, S. H.; Jackson, K. A.; Pederson, M. R.; Singh, D. J.; Fiolhais, C. Atoms, molecules, solids, and surfaces: Applications of the generalized gradient approximation for exchange and correlation. *Phys. Rev. B: Condens. Matter Mater. Phys.* **1992**, *46*, 6671
[15]Perdew, J. P.; Chevary, J.; Vosko, S.; Jackson, K. A.; Pederson, M. R.; Singh, D.; Fiolhais, C. Erratum: Atoms, molecules, solids, and surfaces: Applications of the gen eralized gradient approximation for exchange and correlation. *Phys. Rev. B: Condens. Matter Mater. Phys.* **1993**, *48*, 4978.
[16]Tao, J.; Perdew, J. P.; Staroverov, V. N.; Scuseria, G. E. Climbing the density functional ladder: Nonempirical meta generalized gradient approximation designed for molecules and solids. *Phys. Rev. Lett.* **2003**, *91*, 146401.
[17]Zhao, Y.; Truhlar, D. G. A new local density functional for main-group thermochemistry, transition metal bonding, thermochemical kinetics, and noncovalent interactions. *J. Chem. Phys.* **2006**, *125*, 194101.
[18]Wang, Y.; Jin, X.; Yu, H. S.; Truhlar, D. G.; He, X. Revised M06-L functional for improved accuracy on chemical reaction barrier heights, noncovalent interactions, and solid-state physics. *Proc. Nat. Acad. Sci. U.S.A.* **2017**, *114*, 8487-8492.
[19]Sun, J.; Ruzsinszky, A.; Perdew, J. P. Strongly constrained and appropriately normed semilocal density functional. *Phys. Rev. Lett.* **2015**, *115*, 036402.
[20]Lee, C.; Yang, W.; Parr, R. G. Development of the Colle-Salvetti correlation-energy formula into a functional of the electron density. *Phys. Rev. B: Condens. Matter Mater. Phys.* **1988**, *37*, 785.

[21]Lynch, B. J.; Fast, P. L.; Harris, M.; Truhlar, D. G. Adiabatic connection for kinetics. *J. Phys. Chem. A* **2000**, *104*, 4811-4815.
[22]Zhao, Y.; Truhlar, D. G. Design of density functionals that are broadly accurate for thermochemistry, thermochemical kinetics, and nonbonded interactions. *J. Phys. Chem. A* **2005**, *109*, 5656-5667.
[23]Zhao, Y.; Truhlar, D. G. The M06 suite of density functionals for main group thermochemistry, thermochemical kinetics, noncovalent interactions, excited states, and transition elements: two new functionals and systematic testing of four M06-class functionals and 12 other functionals. *Theor. Chem. Acc.* **2008**, *120*, 215241.
[24]Zhao, Y.; Truhlar, D. G. Density functional for spectroscopy: no long-range self interaction error, good performance for Rydberg and charge-transfer states, and better performance on average than B3LYP for ground states. *J. Phys. Chem. A* **2006**, 110, 13126-13130.
[25]Peverati, R.; Truhlar, D. G. Improving the accuracy of hybrid meta-GGA density functionals by range separation. *J. Phys. Chem. Lett.* **2011**, *2*, 2810-2817.
[26]Yu, H. S.; Zhang, W.; Verma, P.; He, X.; Truhlar, D. G. Nonseparable exchange correlation functional for molecules, including homogeneous catalysis involving transition metals. *Phys. Chem. Chem. Phys.* **2015**, *17*, 12146-12160.
[27]Haoyu, S. Y.; He, X., Li, S. L.; Truhlar, D. G. MN15: A Kohn–Sham global-hybrid exchange–correlation density functional with broad accuracy for multi-reference and single-reference systems and noncovalent interactions. *Chem. Sci.* **2016**, *7*, 5032-5051.
[28]Yu, H. S.; He, X.; Truhlar, D. G. MN15-L: A new local exchange-correlation functional for Kohn Sham density functional theory with broad accuracy for atoms, molecules, and solids. *J. Chem. Theory Comput.* **2016**, *12*, 1280-1293.
[29]Liu, Y.; Zhang; C., Liu, Z.; Truhlar, D. G.; Wang, Y.; He, X. Supervised learning of a chemistry functional with damped dispersion. *Nat. Comput. Sci.* **2023**, *3*, 48-58.
[30]Wellendor , J.; Lundgaard, K. T.; Mgelh j, A.; Petzold, V.; Landis, D. D.; Nrskov, J. K.; Bligaard, T.; Jacobsen, K. W. Density functionals for surface science: Exchange-correlation model development with Bayesian error estimation. *Phys. Rev. B* **2012**, *85*, 235149.
[31]Balasubramanian, R.; Smith, S. M.; Rawat, S.; Yatsunyk, L. A.; Stemmler, T. L.; Rosenzweig, A. C., Oxidation of Methane by a Biological Dicopper Centre. *Nature* **2010,** *465*, 115-119.
[32]Cao, L.; Caldararu, O.; Rosenzweig, A. C.; Ryde, U., Quantum Refinement does not Support Dinuclear Copper Sites in Crystal Structures of Particulate Methane Monooxygenase. *Angew. Chem. Int. Ed.* **2018,** *57*, 162-166.
[33]Sushkevich, V. L.; Palagin, D.; van Bokhoven, J. A., The Effect of the Active-Site Structure on the Activity of Copper Mordenite in the Aerobic and Anaerobic Conversion of Methane into Methanol. *Angew. Chem. Int. Ed.* **2018,** *57*, 8906-8910.
[34]Meyet, J.; Searles, K.; Newton, M. A.; Worle, M.; van Bavel, A. P.; Horton, A. D.; van Bokhoven, J. A.; Coperet, C., Monomeric Copper(II) Sites Supported on Alumina Selectively Convert Methane to Methanol. *Angew. Chem. Int. Ed.* **2019,** *58*, 9841-9845.

[35]Woertink, J. S.; Smeets, P. J.; Groothaert, M. H.; Vance, M. A.; Sels, B. F.; Schoonheydt, R. A.; Solomon, E. I., A $[Cu_2O]^{2+}$ Core in Cu-ZSM-5, the Active Site in the Oxidation of Methane to Methanol. *Proc. Natl. Acad. Sci. U.S.A.* **2009,** *106*, 18908.
[36]Smeets, P. J.; Hadt, R. G.; Woertink, J. S.; Vanelderen, P.; Schoonheydt, R. A.; Sels, B. F.; Solomon, E. I., Oxygen Precursor to the Reactive Intermediate in Methanol Synthesis by Cu-ZSM-5. *J. Am. Chem. Soc.* **2010,** *132*, 14736-14738.
[37]Sushkevich, V. L.; Palagin, D.; Ranocchiari, M.; van Bokhoven, J. A., Selective Anaerobic Oxidation of Methane Enables Direct Synthesis of Methanol. *Science* **2017,** *356*, 523-527.
[38]Grundner, S.; Markovits, M. A. C.; Li, G.; Tromp, M.; Pidko, E. A.; Hensen, E. J. M.; Jentys, A.; Sanchez-Sanchez, M.; Lercher, J. A., Single-Site Trinuclear Copper Oxygen Clusters in Mordenite for Selective Conversion of Methane to Methanol. *Nat. Commun.* **2015,** *6*, 7546-7554.
[39]Tomkins, P.; Mansouri, A.; Bozbag, S. E.; Krumeich, F.; Park, M. B.; Alayon, E. M. C.; Ranocchiari, M.; van Bokhoven, J. A., Isothermal Cyclic Conversion of Methane into Methanol over Copper-Exchanged Zeolite at Low Temperature. *Angew. Chem. Int. Ed.* **2016,** *55*, 5467-5471.
[40]Sun, L.; Wang, Y.; Wang, C.; Xie, Z.; Guan, N.; Li, L., Water-Involved Methane-Selective Catalytic Oxidation by Dioxygen over Copper Zeolites. *Chem* **2021,** *7*, 1557-1568.
[41]Pappas, D. K.; Martini, A.; Dyballa, M.; Kvande, K.; Teketel, S.; Lomachenko, K. A.; Baran, R.; Glatzel, P.; Arstad, B.; Berlier, G.; Lamberti, C.; Bordiga, S.; Olsbye, U.; Svelle, S.; Beato, P.; Borfecchia, E., The Nuclearity of the Active Site for Methane to Methanol Conversion in Cu-Mordenite: A Quantitative Assessment. *J. Am. Chem. Soc.* **2018,** *140*, 15270-15278.
[42]Nørskov, J. K.; Bligaard, T.; Rossmeisl, J.; Christensen, C. H. Towards the Computational Design of Solid Catalysts. *Nat. Chem.* **2009**, *1* (1), 37–46.
[43]Ishikawa, A. Heterogeneous Catalyst Design by Generative Adversarial Network and First-Principles Based Microkinetics. *Sci. Rep.* **2022**, *12* (1), 11657.
[44]Jinnouchi, R.; Asahi, R. Predicting Catalytic Activity of Nanoparticles by a DFTAided Machine-Learning Algorithm. *J. Phys. Chem. Lett.* **2017**, *8* (17), 4279–4283.
[45]Bour, J. R.; Wright, A. M.; He, X.; Dinca, M., Bioinspired Chemistry at MOF Secondary Building Units. *Chem. Sci.* **2020,** *11*, 1728-1737.
[46]Liu, J.; Goetjen, T. A.; Wang, Q.; Knapp, J. G.; Wasson, M. C.; Yang, Y.; Syed, Z. H.; Delferro, M.; Notestein, J. M.; Farha, O. K.; Hupp, J. T., MOF-Enabled Confinement and Related Effects for Chemical Catalyst Presentation and Utilization. *Chem. Soc. Rev.* **2022,** *51*, 1045-1097.
[47]Ji, Z.; Wang, H.; Canossa, S.; Wuttke, S.; Yaghi, O. M., Pore Chemistry of Metal–Organic Frameworks. *Adv. Funct. Mater.* **2020,** *30*, 2000238.
[48]Cai, G.; Yan, P.; Zhang, L.; Zhou, H.-C.; Jiang, H.-L., Metal–Organic Framework-Based Hierarchically Porous Materials: Synthesis and Applications. *Chem. Rev.* **2021,** *121*, 12278-12326.

[49]Guillerm, V.; Eddaoudi, M., The Importance of Highly Connected Building Units in Reticular Chemistry: Thoughtful Design of Metal–Organic Frameworks. *Acc. Chem. Res.* **2021,** *54*, 3298-3312.
[50]Guo, P.; Froese, C.; Fu, Q.; Chen, Y.-T.; Peng, B.; Kleist, W.; Fischer, R. A.; Muhler, M.; Wang, Y., CuPd Mixed-Metal HKUST-1 as a Catalyst for Aerobic Alcohol Oxidation. *J. Phys. Chem. C* **2018,** *122*, 21433-21440.
[51]Xiao, D. J.; Bloch, E. D.; Mason, J. A.; Queen, W. L.; Hudson, M. R.; Planas, N.; Borycz, J.; Dzubak, A. L.; Verma, P.; Lee, K.; Bonino, F.; Crocella, V.; Yano, J.; Bordiga, S.; Truhlar, D. G.; Gagliardi, L.; Brown, C. M.; Long, J. R., Oxidation of Ethane to Ethanol by N_2O in a Metal-Organic Framework with Coordinatively Unsaturated Iron(II) Sites. *Nat. Chem.* **2014,** *6*, 590-595.
[52]Osadchii, D. Y.; Olivos-Suarez, A. I.; Szécsényi, Á.; Li, G.; Nasalevich, M. A.; Dugulan, I. A.; Crespo, P. S.; Hensen, E. J. M.; Veber, S. L.; Fedin, M. V.; Sankar, G.; Pidko, E. A.; Gascon, J., Isolated Fe Sites in Metal Organic Frameworks Catalyze the Direct Conversion of Methane to Methanol. *ACS Catal.* **2018,** *8*, 5542-5548.
[53]Sun, C.; Skorupskii, G.; Dou, J.-H.; Wright, A. M.; Dincă, M., Reversible Metalation and Catalysis with a Scorpionate-like Metallo-ligand in a Metal–Organic Framework. *J. Am. Chem. Soc.* **2018,** *140*, 17394-17398.
[54]He, X.; Looker, B. G.; Dinh, K. T.; Stubbs, A. W.; Chen, T.; Meyer, R. J.; Serna, P.; Román-Leshkov, Y.; Lancaster, K. M.; Dincă, M., Cerium(IV) Enhances the Catalytic Oxidation Activity of Single-Site Cu Active Sites in MOFs. *ACS Catal.* **2020,** *10,* 7820-7825.
[55]Yang, Y.; Zhang, X.; Kanchanakungwankul, S.; Lu, Z.; Noh, H.; Syed, Z. H.; Farha, O. K.; Truhlar, D. G.; Hupp, J. T., Unexpected "Spontaneous" Evolution of Catalytic, MOF-Supported Single Cu(II) Cations to Catalytic, MOF-Supported Cu(0) Nanoparticles. *J. Am. Chem. Soc.* **2020,** *142*, 21169-21177.
[56]Manna, K.; Zhang, T.; Lin, W., Postsynthetic Metalation of Bipyridyl-Containing Metal–Organic Frameworks for Highly Efficient Catalytic Organic Transformations. *J. Am. Chem. Soc.* **2014,** *136*, 6566-6569.
[57]Zhang, X.; Vermeulen, N. A.; Huang, Z.; Cui, Y.; Liu, J.; Krzyaniak, M. D.; Li, Z.; Noh, H.; Wasielewski, M. R.; Delferro, M.; Farha, O. K., Effect of Redox "Non-Innocent" Linker on the Catalytic Activity of Copper-Catecholate-Decorated Metal–Organic Frameworks. *ACS Appl. Mater. Interfaces* **2018,** *10*, 635-641.
[58]Yuan, S.; Qin, J. S.; Li, J.; Huang, L.; Feng, L.; Fang, Y.; Lollar, C.; Pang, J.; Zhang, L.; Sun, D.; Alsalme, A.; Cagin, T.; Zhou, H. C., Retrosynthesis of Multi-Component Metal−Organic Frameworks. *Nat. Commun.* **2018,** *9*, 808.
[59]Yang, Y.; Noh, H.; Ma, Q.; Wang, R.; Chen, Z.; Schweitzer, N. M.; Liu, J.; Chapman, K. W.; Hupp, J. T., Engineering Dendrimer-Templated, Metal–Organic Framework-Confined Zero-Valent, Transition-Metal Catalysts. *ACS Appl. Mater. Interfaces* **2021,** *13*, 36232-36239.

[60]Luo, Y.; Fan, S.; Yu, W.; Wu, Z.; Cullen, D. A.; Liang, C.; Shi, J.; Su, C., Fabrication of $Au_{25}(SG)_{18}$–ZIF-8 Nanocomposites: A Facile Strategy to Position $Au_{25}(SG)_{18}$ Nanoclusters Inside and Outside ZIF-8. *Adv. Mater.* **2018,** *30*, 1704576.
[61]Buru, C. T.; Farha, O. K., Strategies for Incorporating Catalytically Active Polyoxometalates in Metal–Organic Frameworks for Organic Transformations. *ACS Appl. Mater. Interfaces* **2020,** *12*, 5345-5360.
[62]Ji, S.; Chen, Y.; Zhao, S.; Chen, W.; Shi, L.; Wang, Y.; Dong, J.; Li, Z.; Li, F.; Chen, C.; Peng, Q.; Li, J.; Wang, D.; Li, Y., Atomically Dispersed Ruthenium Species Inside Metal-Organic Frameworks: Combining the High Activity of Atomic Sites and the Molecular Sieving Effect of MOFs. *Angew. Chem. Int. Ed.* **2019,** *58*, 4271-4275.
[63]Ikuno, T.; Zheng, J.; Vjunov, A.; Sanchez-Sanchez, M.; Ortuño, M. A.; Pahls, D. R.; Fulton, J. L.; Camaioni, D. M.; Li, Z.; Ray, D.; Mehdi, B. L.; Browning, N. D.; Farha, O. K.; Hupp, J. T.; Cramer, C. J.; Gagliardi, L.; Lercher, J. A., Methane Oxidation to Methanol Catalyzed by Cu-Oxo Clusters Stabilized in NU-1000 Metal–Organic Framework. *J. Am. Chem. Soc.* **2017,** *139*, 10294-10301.
[64]Zheng, J.; Ye, J.; Ortuño, M. A.; Fulton, J. L.; Gutiérrez, O. Y.; Camaioni, D. M.; Motkuri, R. K.; Li, Z.; Webber, T. E.; Mehdi, B. L.; Browning, N. D.; Penn, R. L.; Farha, O. K.; Hupp, J. T.; Truhlar, D. G.; Cramer, C. J.; Lercher, J. A., Selective Methane Oxidation to Methanol on Cu-Oxo Dimers Stabilized by Zirconia Nodes of an NU-1000 Metal–Organic Framework. *J. Am. Chem. Soc.* **2019,** *141*, 9292-9304.
[65]Ji, S.; Chen, Y.; Zhao, S.; Chen, W.; Shi, L.; Wang, Y.; Dong, J.; Li, Z.; Li, F.; Chen, C.; Peng, Q.; Li, J.; Wang, D.; Li, Y., Atomically Dispersed Ruthenium Species Inside Metal-Organic Frameworks: Combining the High Activity of Atomic Sites and the Molecular Sieving Effect of MOFs. *Angew. Chem. Int. Ed.* **2019,** *58*, 4271-4275.
[66]Park, K. S.; Ni, Z.; Côté, A. P.; Choi, J. Y.; Huang, R.; Uribe-Romo, F. J.; Chae, H. K.; O'Keeffe, M.; Yaghi, O. M., Exceptional Chemical and Thermal Stability of Zeolitic Imidazolate Frameworks. *Proc. Natl. Acad. Sci. U.S.A.* **2006,** *103*, 10186-10191.
[67]Huang, X. C.; Lin, Y. Y.; Zhang, J. P.; Chen, X. M., Ligand-Directed Strategy for Zeolite-Type Metal–Organic Frameworks: Zinc(II) Imidazolates with Unusual Zeolitic Topologies. *Angew. Chem. Int. Ed.* **2006,** *45*, 1557-1559.
[68]Fairen-Jimenez, D.; Galvelis, R.; Torrisi, A.; Gellan, A. D.; Wharmby, M. T.; Wright, P. A.; Mellot-Draznieks, C.; Duren, T., Flexibility and Swing Effect on the Adsorption of Energy-Related Gases on ZIF-8: Combined Experimental and Simulation Study. *Dalton Trans.* **2012,** *41*, 10752-62.
[69]Fairen-Jimenez, D.; Moggach, S. A.; Wharmby, M. T.; Wright, P. A.; Parsons, S.; Düren, T., Opening the Gate: Framework Flexibility in ZIF-8 Explored by Experiments and Simulations. *J. Am. Chem. Soc.* **2011,** *133*, 8900-8902.
[70]Hobday, C. L.; Woodall, C. H.; Lennox, M. J.; Frost, M.; Kamenev, K.; Düren, T.; Morrison, C. A.; Moggach, S. A., Understanding the Adsorption Process in ZIF-8 Using High Pressure Crystallography and Computational Modelling. *Nat. Commun.* **2018,** *9*, 1429.
[71]Tully, J. Mixed quantum–classical dynamics. *Faraday Discuss.* **1998**, *110*, 407-419.

[72]Hack, M. D.; Truhlar, D. G. Nonadiabatic trajectories at an exhibition. *J. Phys. Chem. A* **2000,** *104*, 7917-7926.
[73]Jasper, A. W.; Zhu, C.; Nangia, S.; Truhlar, D. G. Introductory lecture: Nonadiabatic effects in chemical dynamics. *Faraday Discuss.* **2004,** *127*, 1-22.
[74]Tully, J. C. Molecular dynamics with electronic transitions. *J. Chem. Phys.* **1990,** *93*, 1061-1071.
[75] Shu, Y.; Truhlar, D. G. Decoherence and its role in electronically nonadiabatic dynamics. *J. Chem. Theory Comput.* **2023,** *19*, 380-395.
[76]Meyera), H. D.; Miller, W. H. A classical analog for electronic degrees of freedom in nonadiabatic collision processes. *J. Chem. Phys.* **1979,** *70*, 3214-3223.
[77]García-Vela, A.; Gerber, R. B.; Imre, D. G. Mixed quantum wave packet/classical trajectory treatment of the photodissociation process ArHCl→ Ar+ H+ Cl. *J. Chem. Phys.* **1992,** *97*, 7242-7250.
[78]Hack, M. D.; Jasper, A. W.; Volobuev, Y. L.; Schwenke, D. W.; Truhlar, D. G. Do semiclassical trajectory theories provide an accurate picture of radiationless decay for systems with accessible surface crossings?. *J. Phys. Chem. A* **2000,** *104*, 217-232.
[79]Prezhdo, O. V.; Rossky, P. J. Evaluation of quantum transition rates from quantum-classical molecular dynamics simulations. *J. Chem. Phys.* **1997,** *107*, 5863-5878.
[80]Zhu, C.; Jasper A. W.; Truhlar, D. G. Non-Born–Oppenheimer trajectories with self-consistent decay of mixing. *J. Chem. Phys.* **2004,** *120*, 5543-5557.
[81]Thachuk, M.; Ivanov, M. Y.; Wardlaw, D. M. A semiclassical approach to intense-field above-threshold dissociation in the long wavelength limit. II. Conservation principles and coherence in surface hopping. *J. Chem. Phys.* **1998,** *109*, 5747-5760.
[82]Parlant, G.; Gislason, E. A. An exact trajectory surface hopping procedure: comparison with exact quantal calculations. *J. Chem. Phys.* **1989,** *91*, 4416-4418.
[83]Parlant, G.; Alexander, M. H. Trajectory surface-hopping study of electronically inelastic collisions of CN (A 2Π) with He: Comparison with exact quantum calculations. *J. Chem. Phys.* **1990,** *92*, 2287-2295.
[84]Martens, C. C.; Fang, J. Y. Semiclassical-limit molecular dynamics on multiple electronic surfaces. *J. Chem. Phys.* **1997,** *106*, 4918-4930.
[85]Donoso, A.; Martens, C. C. Simulation of coherent nonadiabatic dynamics using classical trajectories. *J. Phys. Chem. A* **1998,** *102*, 4291-4300.
[86]Martínez, T. J.; Ben-Nun, M.; Levine, R. D. Molecular collision dynamics on several electronic states. *J. Phys. Chem. A* **1997,** *101*, 6389-6402.
[87]Hack, M. D.; Wensmann, A. M.; Truhlar, D. G.; Ben-Nun, M.;Martínez, T. J. Comparison of full multiple spawning, trajectory surface hopping, and converged quantum mechanics for electronically nonadiabatic dynamics. *J. Chem. Phys.* **2001,** *115*, 1172-1186.
[88]Zhu, C.; Nangia, S.; Jasper, A. W.; Truhlar, D. G. Coherent switching with decay of mixing: an improved treatment of electronic coherence for non-Born–Oppenheimer trajectories. *J. Chem. Phys.* **2004**, *121*, 7658-7670.

[89]Tully, J. C. Nonadiabatic Processes in Molecular Collisions. In Dynamics of Molecular Collisions; Part, B., Miller, W. H., Eds.; Plenum/Springer: New York, **1976**, pp 217−267.
[90]Tully, J. C.; Thompson, D. L. Nonadiabatic Dynamics. In Modern Methods for Multidimensional Dynamics Computations in Chemistry; World Scientific: Singapore, **1998**, pp 34−72.
[91]Granucci, G.; Persico, M.; Toniolo, A. Direct Semiclassical simulation of photochemical processes with semiempirical wave functions. *J. Chem. Phys.* **2001**, *114*, 10608−10615.
[92]Mandal, A.; Yamijala, S. S.; Huo, P. Quasi-diabatic representation for nonadiabatic propagation. *J. Chem. Theory Comput.* **2018**, *14*, 1828−1840.
[93]Zhou, W.; Mandal, A.; Huo, P. Quasi-Diabatic Scheme for Nonadiabatic On-the-Fly Simulations. *J. Phys. Chem. Lett.* **2019**, *10*, 7062−7070.
[94]Meek, G. A.; Levine, B. G. Accurate and efficient evaluation of transition probabilities at unavoided crossings in ab initio multiple spawning. *Chem. Phys.* **2015**, *460*, 117−124.
[95]Shu, Y.; Zhang, L.; Sun, S.; Truhlar, D. G. Time-Derivative Couplings for Self-Consistent Electronically Nonadiabatic Dynamics. *J. Chem. Theory Comput.* **2020**, *16*, 4098−4106.
[96]Shavitt, I. The Method of Configuration Interaction. In Methods of Electronic Structure Theory; Schaefer, H. F., III, Ed.; Plenum: New York, **1976**; pp 189−275.
[97]Cizek, J. On the Use of the Cluster Expansion and the Technique of Diagrams in Calculations of Correlation Effects in Atoms and Molecules. *Adv. Chem. Phys.* **1969**, *14*,35−89.
[98]Koch, H.; Jørgensen, P. Coupled cluster response functions. *J. Chem. Phys.* **1990**, *93*, 3333−3344.
[99]Li Manni, G.; Carlson, R. K.; Luo, S.; Ma, D.; Olsen, J.; Truhlar, D. G.; Gagliardi, L. Multiconfiguration Pair-Density Functional Theory. *J. Chem. Theory Comput.* **2014**, *10*, 3669−3680.
[100]Shu, Y.; Zhang, L.; Chen, X.; Sun, S.; Huang, Y.; Truhlar, D. G. Nonadiabatic dynamics algorithms with only potential energies and gradients: Curvature-driven coherent switching with decay of mixing and curvature-driven trajectory surface hopping. *J. Chem. Theory Comput.* **2022,** *18*, 1320-1328.
[101]Baeck, K. K.; An, H. Practical Approximation of the Non Adiabatic Coupling Terms for Same-Symmetry Interstate Crossings by Using Adiabatic Potential Energies Only. *J. Chem. Phys.* **2017**, *146*, 064107.
[102]Shu, Y.; Zhang, L.; Truhlar, D. G. SHARC-MN, version 1.1; University of Minnesota: Minneapolis, **2021**. https://comp.chem. umn.edu/sharc-mn.
[103]Ning, J.; Truhlar, D. G. The valence and Rydberg states of dienes. *Phys. Chem. Chem. Phys.* **2020**, *22*, 6176-6183.
[104]Tully, J. C. Nonadiabatic Dynamics. In Modern Methods for Multidimensional Dynamics Computations in Chemistry, Thompson, D. L.; World Scientific: Singapore, **1998**; 34−72.
[105]Jasper, A. W.; Kendrick, B. K.; Mead, C. A.; Truhlar, D. G.. Non Born-Oppenheimer Chemistry: Potential Surfaces, Couplings, and Dynamics. In Modern Trends in Chemical

Reaction Dynamics: Experiment and Theory (Part 1), Yang, X.; Liu, K.; World Scientific: Singapore, **2004**; 329−391.
[106]Nakamura, H.; Truhlar, D. G. Extension of the Fourfold Way for Calculation of Global Diabatic Potential Energy Surfaces of Complex, Multi-Arrangement, Non-Born-Oppenheimer Systems: Application to HNCO (S0,S1). *J. Chem. Phys.* **2003**, *118*, 6816−6829.
[107]Shu, Y.; Truhlar, D. G. Diabatization by machine intelligence. *J. Chem. Theory Comput.* **2020,** *16*, 6456-6464.
[108]Lenzen, T.; Manthe, U. Neural Network Based Coupled Diabatic Potential Energy Surfaces for Reactive Scattering. *J. Chem. Phys.* **2017,** 147, 084105.
[109]Gurney, K. An Introduction to Neural Networks; Routledge: London, **1997.**
[110]Bishop, C. M. Pattern Recognition and Machine Learning; Springer: New Delhi, **2006.**
[111]Han, S.; You, H. S.; Kim, S. Y.; Kim, S. K. Dynamic role of intermolecular hydrogen bonding in nonadiabatic chemistry revealed in the UV photodissociation reactions of 2-fluorothiophenol and 2-chlorothiophenol. *J. Phys. Chem. A* **2014**, *118*, 6940−6949.
[112]Shu, Y.; Zhang, L.; Truhlar, D. G. *SHARC-MN*–v1.2; University of Minnesota, Minneapolis, **2022**; https://comp.chem.umn.edu/sharc-mn
[113]Shu, Y.; Zhang, L.; Zheng, J.; Li, Z.-H.; Jasper, A. W.; Bonhommeau, D. A.; Valero, R.; Meana-Pañeda, R.; Mielke, S. L.; Truhlar, D. G. *ANT 2023*; University of Minnesota, Minneapolis, 2023.10.5281/zenodo.7807406

Chapter 2 Bioinspired Cu(II) Defect Sites in ZIF-8 for Selective Methane Oxidation

In part from

Yang, Y.; Kanchanakungwankul; S.; Bhaumik, S.; Ma, Q.; Ahn, S.; Truhlar, D. G.; Hupp, J. T. Bioinspired Cu (II) Defect Sites in ZIF-8 for Selective Methane Oxidation. *J. Am. Chem. Soc.* **2023,** *145*, 22019-22030.

2.1 Introduction

The intensive exploration of shale gas within the past decade is reshaping the traditional chemical industry.[114,115] Shale gas, as an inexpensive and abundant source of small alkanes (methane, ethane, and propane), can be transformed into more valuable oxygenates including alcohols and ketones as chemical feedstocks for basic commodities.[116] However, the chemical inertness of these alkanes poses a significant challenge in activating the C–H bond while trapping the partially oxygenated products from overoxidation to more thermodynamically stable products, CO and CO_2.[117,118] In nature, copper- and iron-based methane monooxygenases (pMMO and sMMO) have perform this transformation by activating dioxygen and methane molecules under ambient conditions for the direct and selective conversion of methane to methanol.[119,120] Immense efforts have been dedicated to developing bio-inspired heterogeneous catalysts to accomplish this in a nonliving context, and Cu-based materials turned out to be attractive due to their capability of using dioxygen as a terminal oxidant. In pMMO, multiple Cu sites are present in different domains, and the recent report from Ross *et al.* identified the monomeric Cu center ligated by histidine residues and carboxylate groups as the active site, with a second monomeric Cu site that is 2 nm away acting as a promoter.[121,122]

In heterogeneous catalysis, an increasing number of studies show the structural flexibility of the Cu-based active moieties including monomer, dimer, trimer, and small clusters.[123,124,125,126,127,128,129,130,131] Reactions are typically carried out in a stepwise fashion involving catalyst oxidation, methane activation, and methanol extraction. The physical separation of methane and oxidant streams, as well as strong methanol binding on the active sites, serve to inhibit overoxidation. Despite the efforts to study Cu-based methane oxidation, there has been no consensus thus far about the actual structure of the active site(s) or the mechanism(s). The difficulty of answering open questions is mainly due to (1) structurally ill-defined metal oxide and zeolite supports lead to the formation of non-uniform catalytic motifs, (2) consequential ambiguity of the transition state structure, (3) minimal understanding of why, in many cases, only a fraction of deposited catalysts are active for the reaction, and (4) a vast number of tunable variables during the material

synthesis and catalysis hindering conclusive insights from a direct comparison of published results. These factors pose a great challenge in identifying comprehensive structure–activity relationships that allow fundamental understanding of the chemistry occurring at the catalytic sites.

In the present article we propose highly crystalline and porous metal−organic frameworks (MOFs) to de-convolute the above complications. MOFs are increasingly regarded as promising model supports for the development of bio-inspired, single-site catalysts with a tailored coordination environment.[132,133,134,135,136] Mononuclear metal ions, as well as metal oxide clusters with uniform structural characteristics can be directly incorporated into the secondary building units (SBUs) during synthesis,[137,138,139,140] anchored onto the nodes, organic linkers, or non-structural modifiers *via* post-synthetic modification,[141,142,143,144,145] or confined inside the pores *via* host-guest interactions.[146,147,148,149] Several successes of MOF-supported copper-oxo clusters for selective methane oxidation have been reported.[150,151,152] The high tunability and structural rigidity of MOFs make it promising to functionally mimic pMMO by anchoring Cu ions into an N-rich environment with a desired configuration.

In this work, we demonstrate that an enzyme-like mononuclear Cu(II) site can be created inside a zeolitic imidazolate framework, ZIF-8 ($Zn_xCu_{1-x}(mim)_2$, where mim^- is 2-methylimiazolate). The resulting materials, featuring a sodalite topology, are capable of stepwise methane oxidation to partially oxygenated products, with methanol and formaldehyde as the major products. Overoxidation can be completely suppressed such that all products are the ones partially oxygenated. Structural evolution of the active sites was uncovered *via* X-ray absorption spectroscopy and its potential correlation with the evolved reactivity is discussed. We also performed calculations on the mechanistic study of methane oxidation using density functional theory (DFT).

2.2 Results and Discussion

2.2.1 Synthesis and Structural Characterization

The direct incorporation of Cu(II) ions into ZIF-8 was carried out following a modified procedure from Schejin *et al.*[153] (see the Supporting Information for details). ZIF-8 ($Zn(mim)_2$, also known as MAF-4) is a highly hydrophobic MOF with excellent chemical and thermal stability. The framework contains large cavities (~11.7 Å) interconnected by narrow windows (~3.4 Å for the 6-membered ring and 0.8 Å for the 4-membered ring; see Figure 5).[154,155] Owing to its structural flexibility, gas molecules like N_2 and CH_4 with kinetic diameters of 3.6 and 3.8 Å, respectively, can be adsorbed within the interior of the framework.[156,157,158] Owing to their higher affinity to the organic linkers, catalytically active single metal ions can be introduced into the framework in place of the tetrahedral Zn(II) atoms.[153,159,160] Specifically, monomeric Cu(II) ions were doped into ZIF-8 by mixed-metal synthesis and the resulting materials are denoted as Cu_x-ZIF (x is the molar fraction of Cu). Successful Cu incorporation was signified by the bulk color difference between white ZIF-8 and grey Cu_x-ZIF, in agreement with the literature.[153] Cu content was quantified by means of inductively coupled plasma–optical emission spectroscopy (ICP-OES) measurements. Due to the higher binding affinity of Cu(II) towards the mim^{1-} linker, and the latent preference of Cu(II) for a five-coordinate rather than a four-coordinate (tetrahedral) ligand environment, incorporation of Cu(II) into ZIF-8 unavoidably generates defect sites, and the lattice eventually loses its crystallinity with an excess amount of Cu.[161]

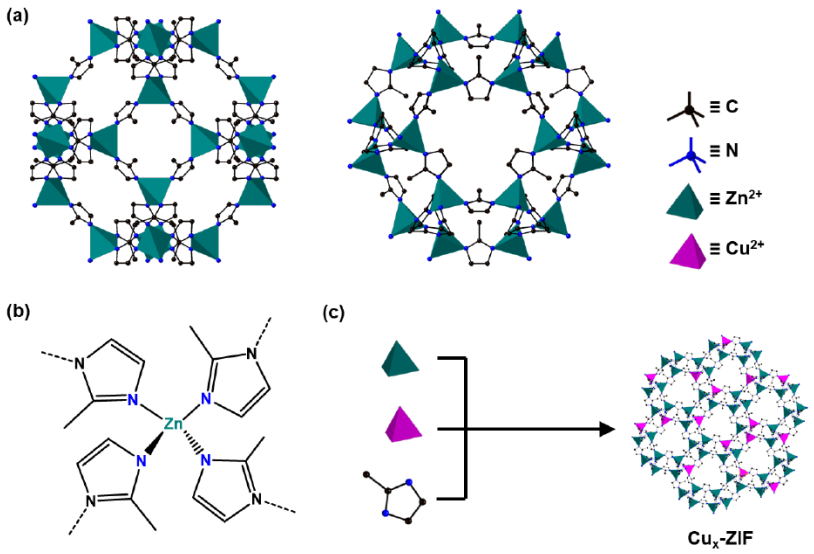

Figure 5: (a) Structure of ZIF-8 with the 4-membered ring viewed along the crystallographic *a* axis (left) and the 6-membered ring viewed along [111] direction (right). (b) Coordination environment of tetrahedral Zn(II) atoms in ZIF-8; (c) Synthesis scheme for Cu_x-ZIF. Hydrogen atoms are omitted for clarity.

By varying the Cu:Zn feeding ratio, Cu loading is controlled at 10%, 20%, and 50%, respectively. The resulting materials exhibit bulk crystallinity, as shown by powder X-ray diffraction (PXRD) patterns (Figure S1). The presence of Cu(II) was further confirmed by diffuse reflectance ultraviolet–visible spectroscopy (DRUV-Vis) as shown in Figure S1**.** All ZIF-8 samples feature a major absorption peak at 220 nm, characteristic of the intraligand charge transfer. The absence of an absorption band around 370 nm indicates the absence of aggregation to form ZnO particles. Pure Zn-based ZIF-8 also has a weak absorption at 300 nm, attributable to ligand-to-metal charge transfer (LMCT).[162] No absorbance is observed in the visible region, in agreement with the white color. In contrast, Cu-ZIF-8 showed distinct absorption between 600-850 nm that can be assigned to a d-d transition of Cu(II) ions, verifying Cu(II) incorporation into the framework.[153] Cu(II) ions coordinated by amine groups have been reported to have a d-d transition band around 605 nm, while a pure oxygen-based coordination environment (like that for hexaaquacopper(II)) typically results in a d-d transition band centered at 850 nm.[146] Distinct bands at 257 nm and 320 nm were also observed, attributable, respectively, to

LMCT from oxygen- and nitrogen-based ligands to a single Cu center.[124,163] The broad absorption at 465 nm for Cu-doped ZIF-8 has been assigned to a Cu(II) d-d transition.[153] Although these measurements do not reveal the exact coordination environment of Cu(II), they are consistent with an N-rich ligand environment in Cu_x-ZIF.

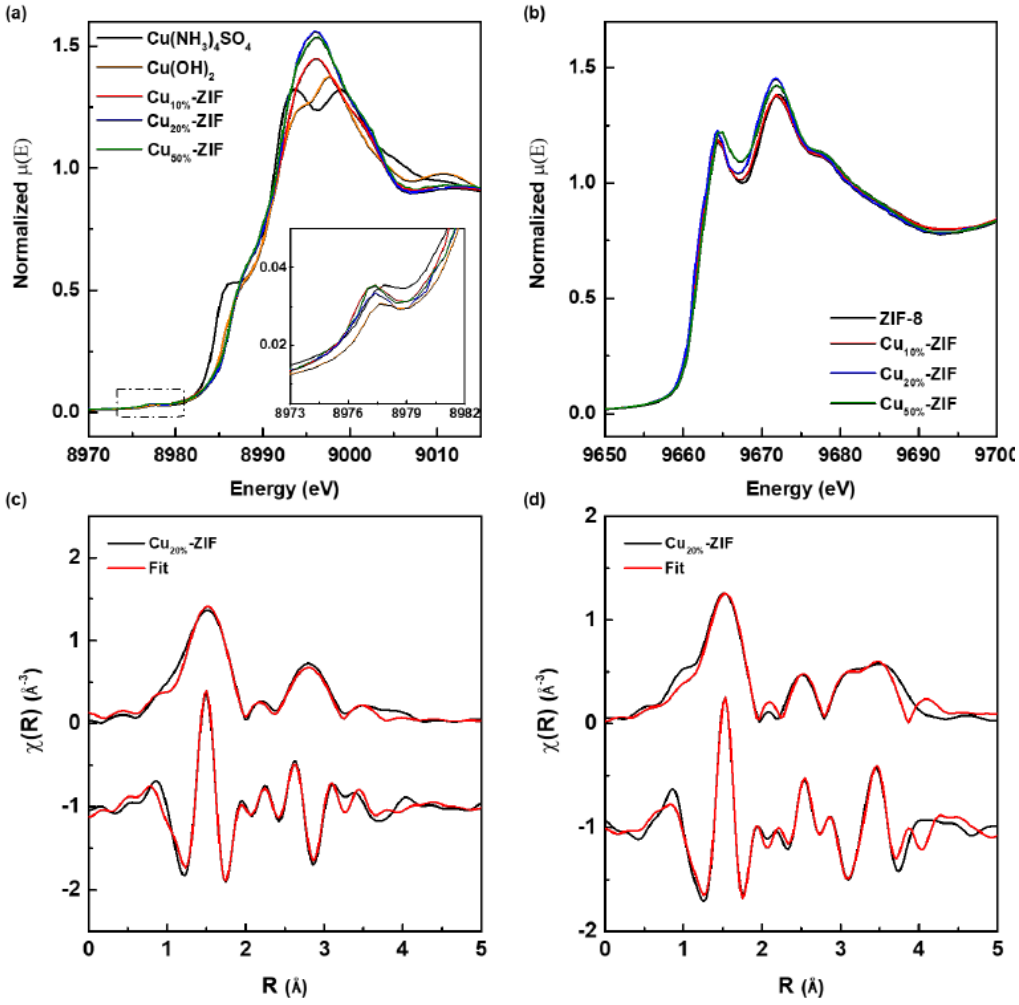

Figure 6: (a, b) Normalized XANES spectra and (c, d) k^2-weighted EXAFS $\chi(R)$ spectra of the as-prepared $Cu_{20\%}$-ZIF at Cu K-edge (left) and Zn K-edge (right). The inset of (a) shows the pre-edge feature corresponding to the 1s-to-3d electronic transition of Cu(II).

X-ray absorption spectroscopy (XAS) including X-ray absorption near-edge structure (XANES) and extended X-ray absorption fine structures (EXAFS) were used to probe the local structure of Cu sites inside ZIF-8, as shown in Figure 6. $Cu_{20\%}$-ZIF

exhibited the 1s-to-4p transition at 8986.2 eV, closely matching that of Cu(II) standards and verifying an oxidation state of +2. The 1s-to-3d spin-forbidden transition was observed at 8977.5 eV, which is indicative of a non-centrosymmetric coordination environment. The relatively higher white line intensity compared to the references suggests a larger coordination number, presumably due to the presence of labile H_2O ligand(s). The local environment is therefore likely distorted square pyramidal or octahedral, as found in supported Cu(II) species in zeolites.[164,165,166] In the *R*-space EXAFS spectrum, a prominent peak between 1 and 2 Å can be attributed to Cu−N or Cu−O scattering, with a coordination number (CN) of 5.7. Signals between 2 and 3 Å are fitted to Cu−C scatterings from the MOF backbone. Incorporation of Cu ions into ZIF-8 does not alter XAS at the Zn K-edge, and thus the chemical environment around Zn(II) remains nearly identical. Heterometallic ZIF-8 with different Cu loadings showed identical XANES spectra at the Zn K-edge, which also overlap with that from monometallic Zn-based ZIF-8. Fitting of $Cu_{20\%}$-ZIF in *R*-space gives CN_{Zn-N} of 3.9, in agreement with the crystallographic structure of pristine ZIF-8. The CNs from the Cu−C and Zn−C scatterings deviate from the theoretical model of ZIF-8, possibly due to the structural disorder from Cu(II) incorporation. Similar XANES and EXAFS spectra were obtained for all Cu-doped materials, which suggests successful, sequential incorporation of single Cu(II) ions into the framework as identical moieties (fitting parameters are shown in Table S1).

2.2.2 Reactivity of Heterometallic ZIF-8 in Selective Methane Oxidation

$Cu_{20\%}$-ZIF was tested over five consecutive cycles to determine the activity and stability of immobilized Cu(II) species. In the 1st cycle, methanol, formaldehyde, and CO_2 were produced with a negligible amount of dimethyl ether. The total product yield reached 1.0 $mmol/mol_{Cu}$ (0.78 μmol/g-catalyst), with a selectivity for methanol and formaldehyde of 68%. A significant decrease in activity was observed in the subsequent two cycles. From the 3rd cycle, the reactivity reached a relatively stable state (around 0.3 $mmol/mol_{Cu}$) and overoxidation was completely suppressed; 100% selectivity for methanol and formaldehyde was achieved (Figure 7).

The rigidity of the catalyst was testified by the retention of porosity, crystallinity, and morphology after five cycles (Figure S2). The sudden change in the catalytic performance from the 3rd cycle may indicate significant structural evolution during the run. However, catalyst poisoning due to inefficient product desorption cannot be excluded – the huge diffusion barrier might inhibit water vapor from penetrating the highly hydrophobic ZIF framework and recovering the Cu sites embedded inside the ZIF crystallites, thereby restricting catalytic activity to Cu(II) sited in the outermost pores of the ZIF crystallites.[167]

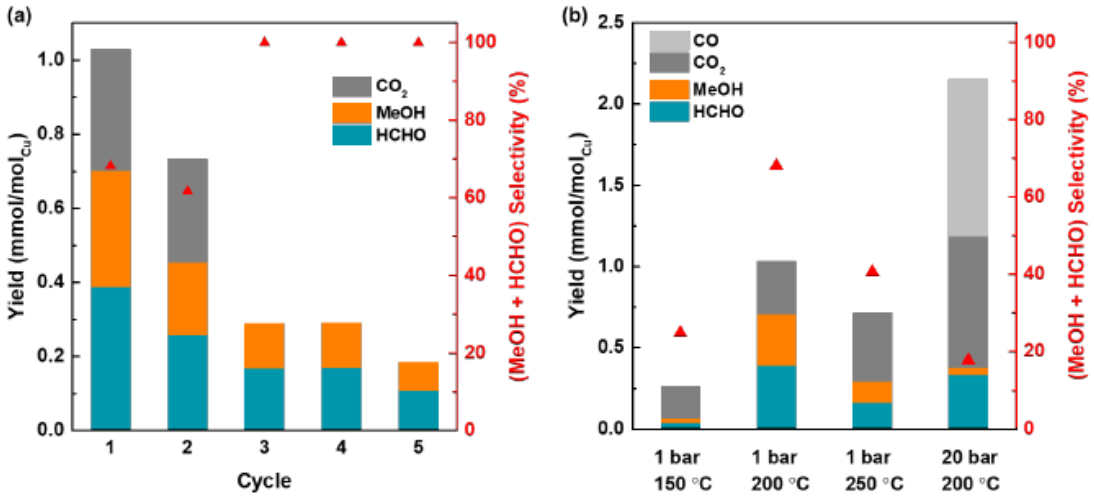

Figure 7: (a) Reactivity over five catalytic cycles of $Cu_{20\%}$-ZIF and the selectivity to methanol and formaldehyde (the catalyst was activated in 1 bar oxygen at 200 °C for 3 h; then 1 bar methane was loaded at 200 °C for 3 h, and finally products were extracted with 15% H_2O and 85% He for 3 h at 135 °C); (b) effect of reaction temperature and pressure during the methane activation step.

2.2.3 Origin of Reactivity in Selective Methane Oxidation

In Cu-exchanged zeolites, Cu(II)-oxo moieties, like $[Cu{-}OH]^+$, $[Cu{-}O{-}Cu]^{2+}$, $[Cu_3(\mu\text{-}O)_3]^{2+}$ act as the active site for methane activation and hydroxylation;[124,125,166] in Cu-ZIF-8, Cu-oxo species at defective sites are expected to behave similarly. The formation of point defects in ZIF-8, including metal/linker vacancies and dangling linkers has proven to be thermodynamically favorable.[168,169] A putative single $Cu^{II}{-}OH$ site (labeled site A) and a site with two neighboring monomeric $Cu^{2+}{-}OH$ and $Cu^{II}{-}OH_2$ interacting by hydrogen

bonding (labeled site B) are depicted in Figure 8, and their relative abundance should depend on the synthesis method and Cu loading. In Cu_x-ZIF, assuming a uniform distribution of Cu throughout the crystallite, at low Cu loading, site A might be predominant, while high Cu loading is necessary for the enrichment of site B. The missing-linker or dangling-linker defects in Cu-ZIF-8 can create metal sites with labile ligands, which can be removed under thermal treatment and leave an open coordination site available for substrate binding and activation. If a labile ligand (OH or H_2O) is removed to create an open coordination site, site A can have Cu^I connecting with three imidazolate ligands without labile OH ligand before O_2 activation involving in methane oxidation. This has also been proposed in other works[8,170,171,172] for pMMO and PHM, which can catalyze methane oxidation in biological systems.

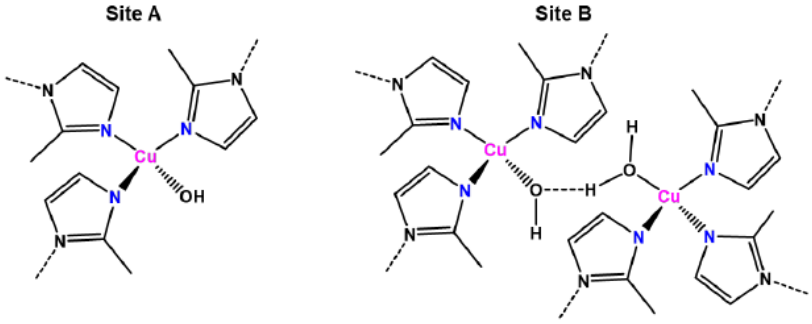

Figure 8: Possible structure of active sites in heterometallic ZIF-8 created by missing-linker or dangling-linker defects. Additional water molecules on Cu are omitted here for clarity.

To evaluate the active fraction of Cu under reaction conditions, the stoichiometries for forming MeOH, HCHO, and CO_2 from CH_4 are calculated based on the number of electrons involved (2, 4, and 8 e^-, respectively) paired with the Cu(II)/Cu(I) redox chemistry. In the first cycle, only 0.5% Cu^{II} participates in the reaction to produce the observed products. There are two possible reasons for the extremely low fraction of active Cu^{II} sites: (1) The majority monomeric Cu(II) species, as identified by XAS and DRUV-Vis, are simply unreactive. Despite the high degree of structural uniformity of MOF-based catalysts, it is the minority forms of oligomeric Cu-oxo species that are responsible for selective methane oxidation. (2) As mentioned above, the inefficient product extraction by

water vapor only recovers a minor fraction of the active sites, and 0.5% may be a huge underestimation of the intrinsic reactivity. Based on scanning electron microscope (SEM) images, the average size of ZIF crystallites is around 700 nm. If we consider all products are extracted from the surface Cu^{II} (1.5% of the total Cu sites) during the first cycle, the corresponding fraction of Cu involved in the reaction would be 33%, with a turnover number of 67 $mmol_{CH_4}/mol_{Cu}$ and productivity of 45 $mmol_{MeOH+HCHO}/mol_{Cu}$ (which would be the highest TON reported for MOF-supported Cu catalyst so far). Relatively low Cu utilization fractions (typically below 10%) have also been reported for other MOF-based systems.[150,151,173] Nevertheless, the diffusion of water vapor into ZIF-8 can be enhanced with hydrophilic linkers (*e.g.*, 3-methyl-1,2,4-triazolate) to facilitate product desorption.[174] An optimal hydrophobicity of the framework is anticipated to achieve a balance between methane uptake and water uptake.

C−H activation of the methane molecule has been demonstrated to be involved in the rate-limiting step for Cu-based catalysts.[175] In both stoichiometric and catalytic processes, an increase in methane pressure improved the methanol productivity significantly, with less prominent impact on the yield of overoxidized CO_2, resulting in an increase in selectivity.[129,151,176,177] The rate (productivity) dependence is attributed to the enhanced diffusion and concentration of methane around the active sites as well as an increased chemical potential of methane.[178,179] In addition, a moderate reaction temperature has been found to be necessary to achieve C−H activation while minimizing overoxidation. Thus, we further investigated the impact of methane loading conditions on the reaction outcome. After activation by 1 bar O_2 at 200 °C, the catalyst was loaded with methane under different temperature and pressure conditions. We observed an unprecedented change in product distribution as well as productivity. As shown in Figure 7, increasing the methane pressure from 1 bar to 20 bar improves the total productivity by a factor of two, suggesting an increase in the number of activated CH_4 molecules. In contrast to previous reports, however, it also decreases the overall selectivity because significant amounts of CO and CO_2 were generated. The selectivity for oxygenates decreased to 17%, dominated by the diminishing methanol production. On the other hand, increasing or decreasing the

reaction temperature leads to decreases in both the reactivity and selectivity. At 250 ℃, a slight decrease in the total productivity and a higher tendency for overoxidation to CO_2 were observed. At 150 ℃, the total product yield decreased from 1.0 to 0.3 $mmol/mol_{Cu}$, suggesting insufficient methane activation at the lower temperature. The yield of oxygenates dropped drastically, with a selectivity of 25%. Overall, methane activation at 200 ℃ and 1 bar turned out to be the optimal condition for our system, resulting in the highest apparent yield (0.7 $mmol_{MeOH+HCHO}/mol_{Cu}$) and selectivity (68%) for methanol and formaldehyde.

2.2.4 Structure Probing During the Reaction

As shown in Figure 9, Cu K-edge XANES of $Cu_{20\%}$-ZIF after catalysis exhibited an edge position closely matching to that of references, suggesting the oxidation state is Cu^{II}. However, a pre-edge feature at 8985 eV was observed; such a feature was also prominent in CuO. As the catalyst was recycled, the intensity of this feature increased, validating the gradual formation of CuO species. This indicates the detachment of single Cu^{2+} ions from the framework and their further agglomeration.[180] Linear combination fitting (LCF) was utilized to quantify isolated versus agglomerated Cu^{2+} using pristine $Cu_{20\%}$-ZIF and CuO as standards (the *R*-factor is below 0.3%). After the first cycle ($Cu_{20\%}$-ZIF-Cat), only 9% Cu^{2+} agglomerates; however, as the material is recycled five times ($Cu_{20\%}$-ZIF-Cat-5X), 27% Cu^{2+} is identified as agglomerated species. The structural evolution after the reaction was also observed in *R*-space. While the Cu−O scattering centered at 1.5 Å shows negligible change after catalysis, the intensity of the signal at 2.8 Å previously assigned to the background scatterings of Cu with the ZIF framework decreased significantly, with a shoulder emerging at 2.5 Å. As the catalyst is recycled, the back-scattering signal from MOF almost disappeared, while the signal at 2.5 Å became predominant. The 2.5 Å signal has been observed for Cu-exchanged zeolites and assigned to the Cu−Cu scattering from Cu-O-Cu moieties.[175] Fitting results of $Cu_{20\%}$-ZIF-Cat-5X agree with the presence of CuO phase; the first scattering peak is fit to Cu−O with CN of 3.51 ± 0.08, and the second peak is fit to Cu−Cu with CN of 2.7 ± 0.8 (Table S1). Considering the absence of CuO peaks

(35.5º and 38.8º) in PXRD as well as the relatively low intensity and CN compared to bulk CuO (CN_{Cu-Cu} = 4) in Cu *R*-space, we speculate the presence of small CuO entities (e.g., subnanometer clusters) in the spent catalyst.

Given the excellent thermal stability of Cu-doped ZIF-8 under air (up to 400 °C),[181,182] a negligible change in the N_2 uptake after catalysis (Figure S2), and the identical coordination environment around Zn after catalysis (Figure 9), structural collapse of the framework is excluded. Instead, we speculate a diffusion scheme similar to Cu-exchanged zeolites − the high mobility of Cu^{2+} ions at the defect sites allows them to diffuse through the pores and form agglomerate species.[166,183] Analogous to the mobilization and transport of Cu^{2+} to $[AlO_4]^-$ sites in zeolites, the dangling imidazolate linker might act to facilitate the diffusion process.[175]

In situ XANES confirmed the irreversible formation of a CuO phase during O_2 activation (see Figure 10; however, negligible change was observed following CH_4 loading and H_2O extraction steps, presumably due to the low fraction of Cu involved in the Cu^{2+}/Cu^+ redox cycle). Combined with the observed catalytic behaviors as the catalyst was recycled, active-site sintering from single Cu^{2+} to small CuO clusters might be responsible for the deactivation. Moreover, it cannot be excluded that the rigid ZIF framework might constrain the sintering to some extent and contribute to the relatively stable performance from the third run onward.

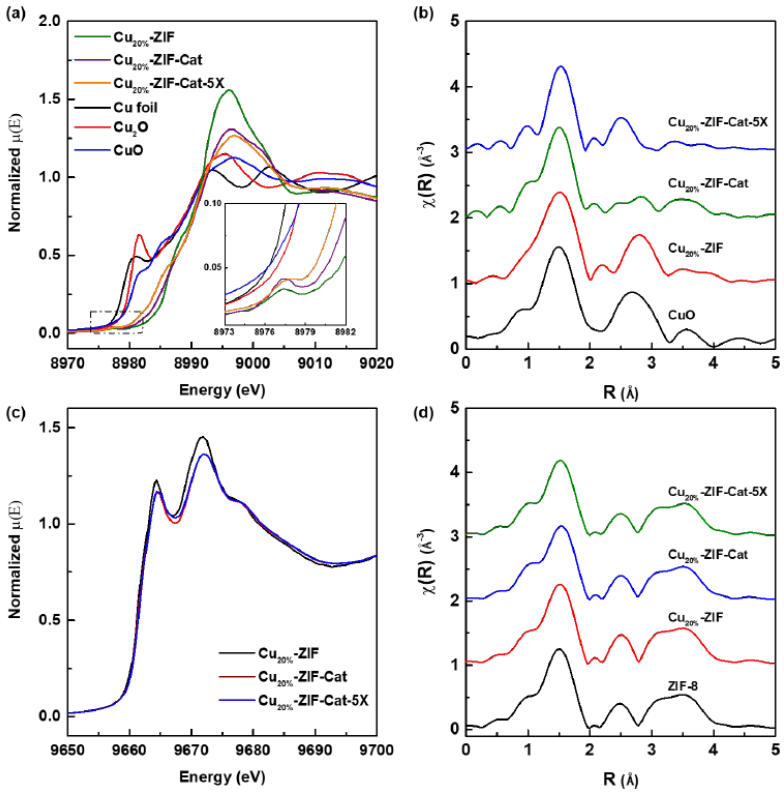

Figure 9: XANES and *R*-space spectra of $Cu_{20\%}$-ZIF before and after catalysis at Cu K-edge (top) and Zn K-edge (bottom).

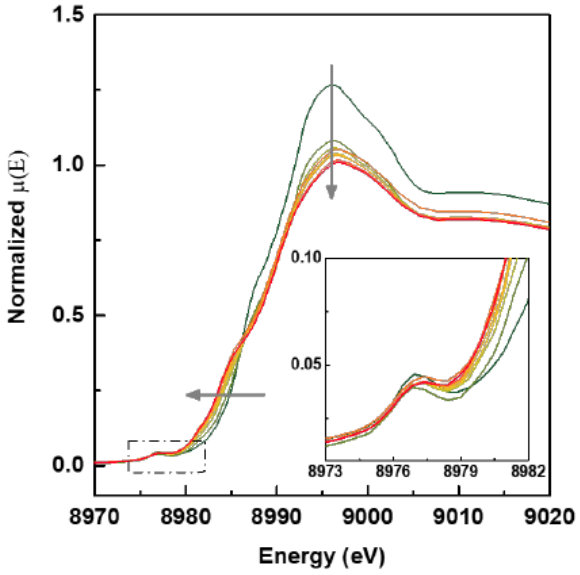

Figure 10: *In situ* Cu K-edge XANES of $Cu_{20\%}$-ZIF during the O_2 activation step. The arrows indicate the signal evolution direction (from green to red).

2.2.5 Mechanistic Study of Oxidation of Methane to Methanol by Cu-ZIF-8 Active Sites

Density functional calculations were performed with the revM06-L exchange–correlation functional[184] to study the possible reaction pathways in the oxidation of methane to methanol by Cu-ZIF-8 active sites (see the Supporting Information for computational details). First, we modeled the smallest unit of the ZIF-8 structure with 35 atoms and four 5-membered rings (imidazolate ligand) where Zn^{II} is tetracoordinated with nitrogen atoms of imidazolate ligand. Then, motivated by the experimental structural characterization, we modeled the Cu-ZIF-8 structure where Cu^{II} replaces Zn^{II} as shown in Figure 11.

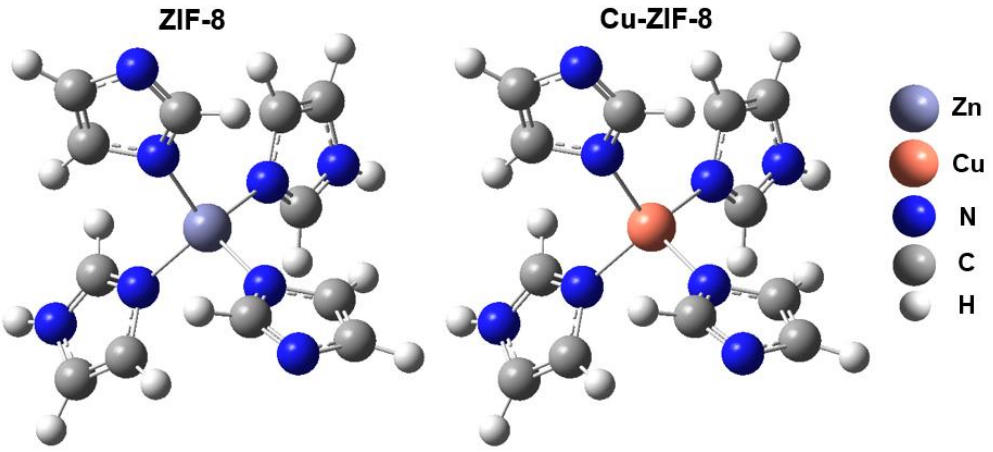

Figure 11: The structures of ZIF-8 with Zn tetracoordinated with N atoms of imidazolate ligands (left) and Cu-ZIF-8 with Cu^{II} replacing Zn^{II} in the ZIF-8 structure (right).

As discussed above, incorporating Cu^{II} in ZIF-8 can generate defective sites that may create metal sites with labile ligands, which can later be removed to produce active sites for substrate binding and activation. The structures in Figure 8 were proposed as possible active sites for methane oxidation by monocopper (type-A site) or by two neighboring copper – $Cu^{II}OH$ and $Cu^{II}OH_2$ interacting by hydrogen bonding (type-B site). These two structures may be favored based on low and high Cu loading, respectively. For the computations, we only studied the mechanism of methane oxidation based on type-A sites because we believe that the reaction mechanism would be similar for type-B sites.

A type-A site can be either LCu^{I} or $LCu^{II}OH$, where L represents the three imidazolate ligands tying the structure to the network. We created these structures from the Cu-ZIF-8 structure in Figure 11. In both biological and nonbiological systems, activation by O_2 can produce either or a singlet or a triplet intermediate as the ground state.[185,] Therefore, for all mechanistic studies in this work, we consider both singlet and triplet pathways.

To determine whether LCu^{I} or $LCu^{II}OH$ would be more easily activated, the Gibbs free energy of the reaction (ΔG) is calculated. The results are shown in Scheme 1. We see that activation of Cu^{I} (that was generated by removing a ligand) is favorable, but the activation of Cu^{II} is not. The scheme shows that O_2 activation of LCu^{I} forms a side-on

$LCu^{II}OO\bullet$ singlet species or an end-on $LCu^{II}OO\bullet$ triplet species, as observed in previous studies. A negative ΔG for both singlet (ΔG = –33 kcal/mol) and triplet (ΔG = –41 kcal/mol) pathways indicates that activation can proceed in either spin state.

Scheme 1. Reactants and products for O_2 activation of LCu^{I} and $LCu^{II}OH$ through the singlet and triplet pathways.

Reactant	Product	
	Side-on-Singlet	End-on-Triplet
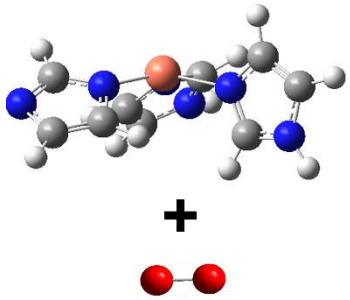	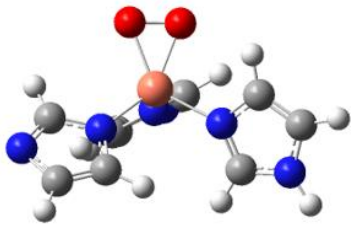	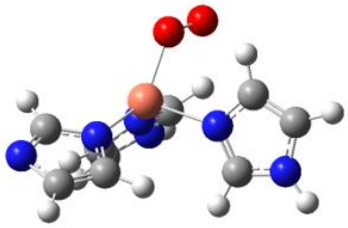
$LCu^{I} + O_2$	$LCu^{II}OO\bullet$ ΔG = -33 kcal/mol	$LCu^{II}OO\bullet$ ΔG = -41 kcal/mol
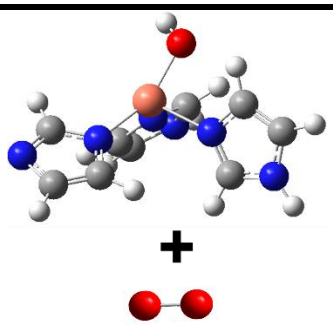	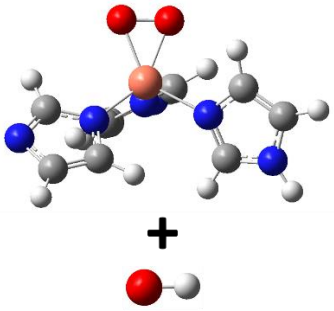	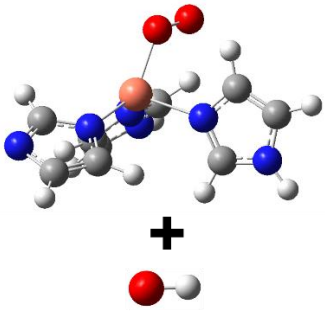
$LCu^{II}OH + O_2$	$LCu^{II}OO\bullet + \bullet OH$ ΔG = 37 kcal/mol	$LCu^{II}OO\bullet + \bullet OH$ ΔG = 29 kcal/mol

Once LCu^{I} activation is achieved with O_2, the catalytic reaction occurs in four steps. The first step is hydrogen atom abstraction from CH_4 by $LCu^{II}OO\bullet$, producing $LCu^{II}OOH\ldots\bullet CH_3$. The notation "…" represents a van der Waals interaction. In the second step, OH is transferred back to methyl, producing $LCu^{II}O\bullet\ldots CH_3OH$, where … indicates noncovalent complexation. These two steps (steps 1 and 2) account for the formation of the first methanol molecule. Since a radical is transferred first from the substrate to the catalyst and then the radical is transferred back to the substrate, these two steps denote a

rebound mechanism. A second rebound sequence between $LCu^{II}O\bullet$ and CH_4 (steps 3 and 4) leads to the formation of $LCu^{I}\ldots CH_3OH$. These two steps (steps 3 and 4) account for restoration of the original catalyst and production of the second methanol molecule. We calculated the free energy of activation ($\Delta G^{\ddagger}$) and the free energy of reaction (ΔG) for each of the four steps. (As usual, the sign convention is that reactions with more negative ΔG and less positive $\Delta G^{\ddagger}$ are more favorable.) The energetics for both the singlet mechanism (steps S1-S4) and the triplet mechanism (steps T1-T4) are in Table 1 and Figure 12. The structures are shown in Schemes 2 and 3. Once CH_3OH is produced, it can undergo oxidation to produce HCHO, which is shown in the experiments to be another product of the oxidation of CH_4, but the present theoretical analysis is limited to the production of methanol.

Table 1: Energetics (kcal/mol at 200 °C and 1 bar) of steps in the singlet and triplet catalytic cycles of oxidation of CH_4 by O_2-activated LCu^{I}

	Steps of singlet pathway	$\Delta G^{\ddagger}$	ΔG
S1	$(LCu^{II}OO\bullet\ldots CH_4) + CH_4 \xrightarrow{TS1} (LCu^{II}OOH\ldots\bullet CH_3) + CH_4$	39	34
S2	$(LCu^{II}OOH\ldots\bullet CH_3) + CH_4 \xrightarrow{TS2} (LCu^{II}O\bullet\ldots CH_3OH) + CH_4$	21	-42
S3	$(LCu^{II}O\bullet\ldots CH_4) + CH_3OH \xrightarrow{TS3} (LCu^{II}OH\ldots\bullet CH_3) + CH_3OH$	10	-8
S4	$(LCu^{II}OH\ldots\bullet CH_3) + CH_3OH \xrightarrow{TS4} (LCu^{I}\ldots CH_3OH) + CH_3OH$	37	-42
	Steps of triplet pathway	$\Delta G^{\ddagger}$	ΔG
T1	$(LCu^{II}OO\bullet\ldots CH_4) + CH_4 \xrightarrow{TS1} (LCu^{II}OOH\ldots\bullet CH_3) + CH_4$	44	40
T2	$(LCu^{II}OOH\ldots\bullet CH_3) + CH_4 \xrightarrow{TS2} (LCu^{II}O\bullet\ldots CH_3OH) + CH_4$	19	-46
T3	$(LCu^{II}O\bullet\ldots CH_4) + CH_3OH \xrightarrow{TS3} (LCu^{II}OH\ldots\bullet CH_3) + CH_3OH$	14	-3
T4	$(LCu^{II}OH\ldots\bullet CH_3) + CH_3OH \xrightarrow{TS4} (LCu^{I}\ldots CH_3OH) + CH_3OH$	48	27

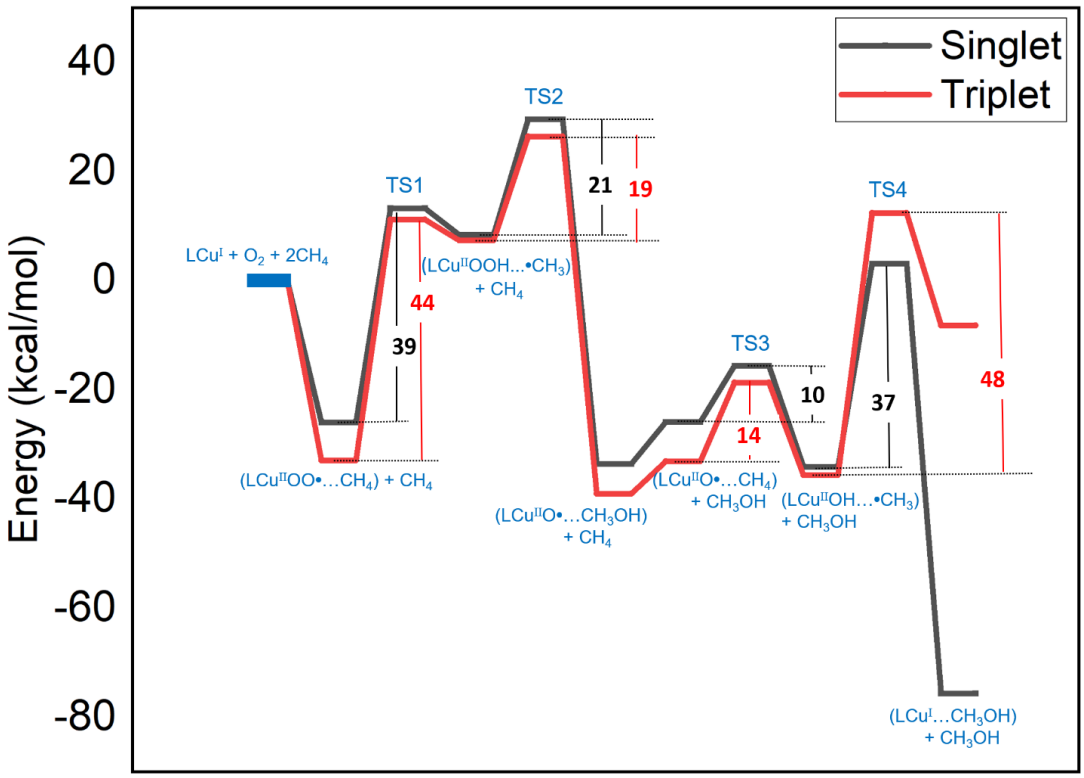

Figure 12: Free energy diagram (in kcal/mol) for the reaction with O_2 and CH_4 of Cu-ZIF-8 labeled as LCu^{I}.

Scheme 2. Stationary points and saddle points for the reactions of O_2-activated LCu^I with CH_4 through the singlet pathway.

	Reactant	Transition State	Product
	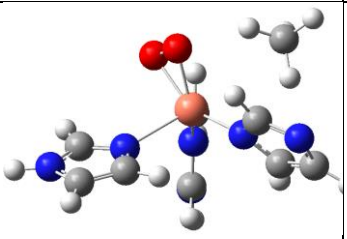	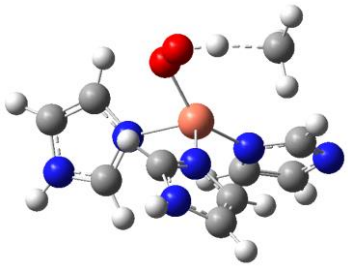	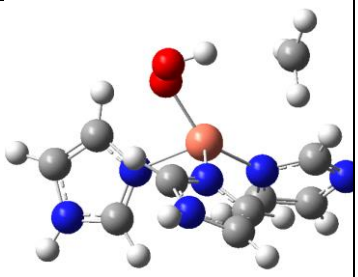
S1	($LCu^{II}OO\bullet\ldots CH_4$)	TS1	($LCu^{II}OOH\ldots\bullet CH_3$)
	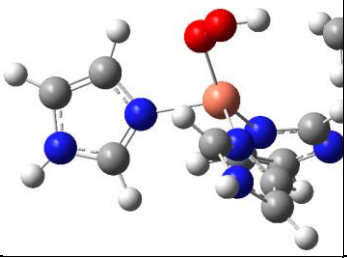	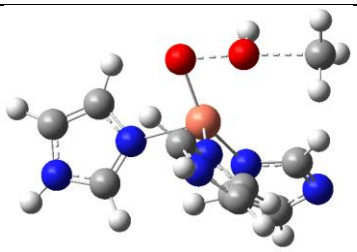	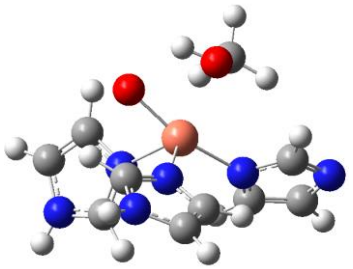
S2	($LCu^{II}OOH\ldots\bullet CH_3$)	TS2	($LCu^{II}O\bullet\ldots CH_3OH$)
	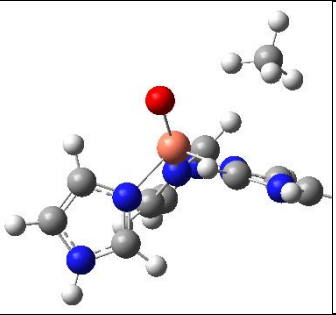	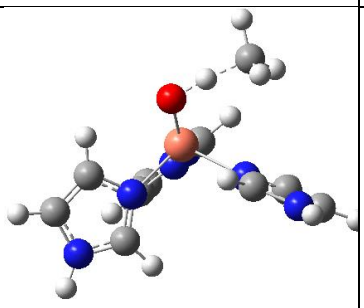	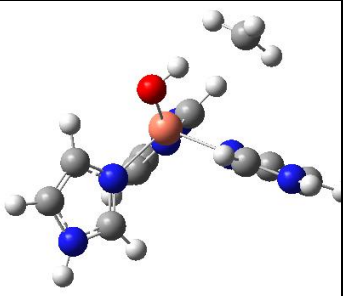
S3	($LCu^{II}O\bullet\ldots CH_4$)	TS3	($LCu^{II}OH\ldots\bullet CH_3$)
	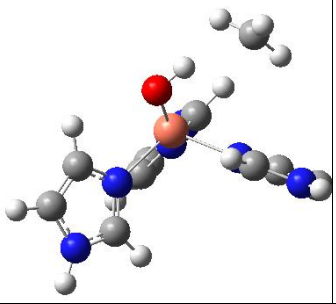	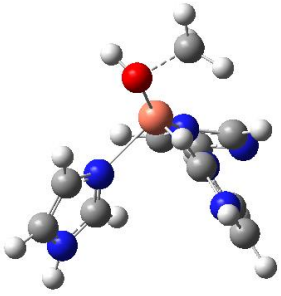	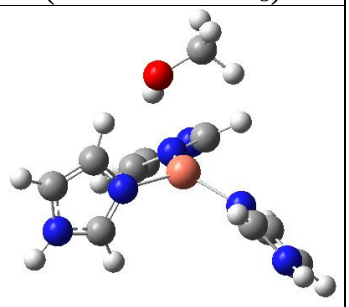
S4	($LCu^{II}OH\ldots\bullet CH_3$)	TS4	($LCu^{I}\ldots CH_3OH$)

Scheme 3. Stationary points and saddle points for the reactions of O_2-activated LCu^I with CH_4 through the triplet pathway.

	Reactant	Transition State	Product
	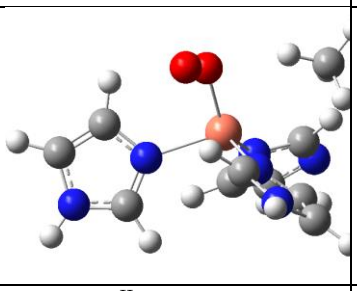	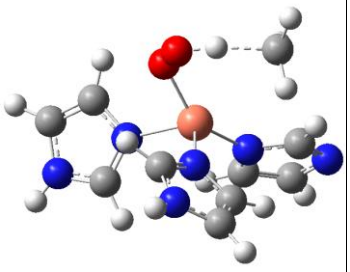	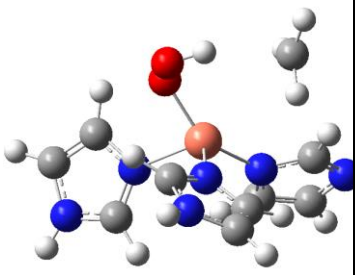
T1	($LCu^{II}OO$•…CH_4)	TS1	($LCu^{II}OOH$…•CH_3)
	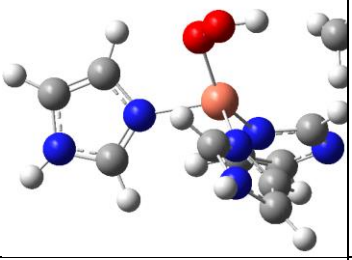	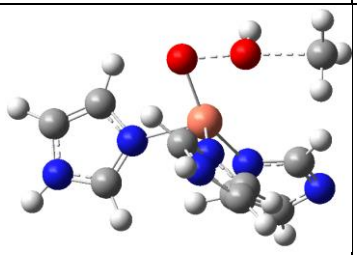	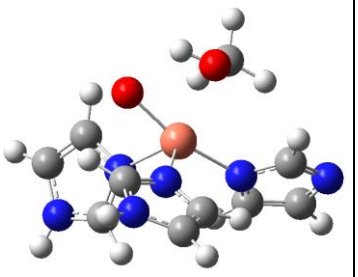
T2	($LCu^{II}OOH$…•CH_3)	TS2	($LCu^{II}O$•…CH_3OH)
	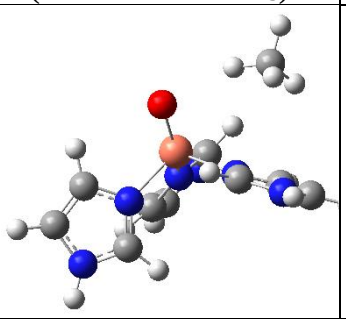	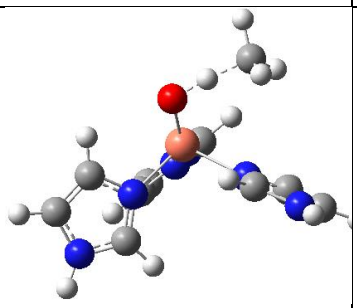	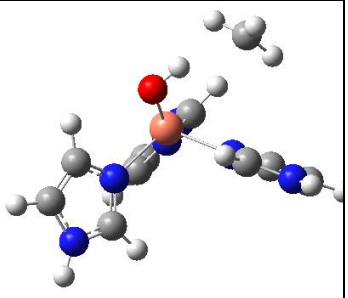
T3	($LCu^{II}O$•…CH_4)	TS3	($LCu^{II}OH$…•CH_3)
	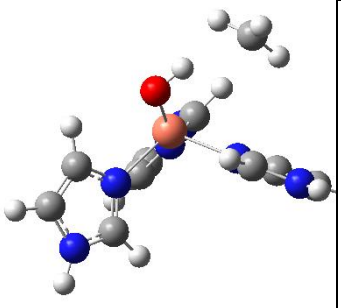	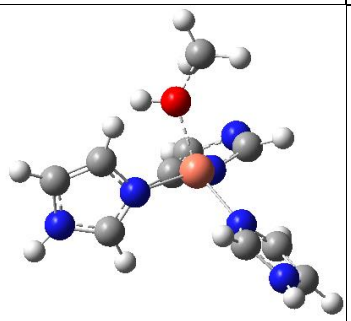	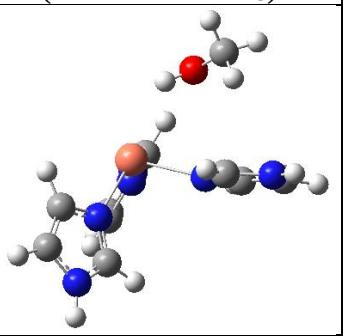
T4	($LCu^{II}OH$…•CH_3)	TS4	(LCu^{I}…CH_3OH)

In the first cycle of addition of CH_4, the $LCu^{II}OO\bullet$ species abstracts a hydrogen atom from CH_4 to form $LCu^{II}OOH\cdots\bullet CH_3$ (represented by S1 and T1 in Table 1). The $\Delta G^{\ddagger}$ for S1 is 5 kcal/mol less positive than that for T1; thus, S1 is favored over T1. The reaction pathway proceeds through the intermolecular rebound reaction of $LCu^{II}OOH$ and $\bullet CH_3$ to form $LCu^{II}O\bullet\cdots CH_3OH$ (represented by S2 and T2 in Table 1). The $\Delta G^{\ddagger}$ for T2 is 2 kcal/mol less positive than S2, and the ΔG for T2 is 4 kcal/mol more negative than S2. Thus, T2 is preferred over S2. Until the first molecule of methanol is produced, the triplet and the singlet pathways are very competitive with S1 being favorable over T1, and T2 being favorable over S2.

In the second cycle of addition of CH_4, $LCu^{II}O\bullet$ abstracts a hydrogen atom from CH_4 to form $LCu^{II}OH\cdots\bullet CH_3$ (represented by S3 and T3 in Table 1). The $\Delta G^{\ddagger}$ for S3 is 4 kcal/mol less positive than T3, and the ΔG for S3 is 5 kcal/mol more negative than T3. Thus, S3 is preferred over T3. The reaction then proceeds through the intermolecular rebound reaction of $LCu^{II}OH$ and $\bullet CH_3$ to form $LCu^{I}\cdots CH_3OH$ (represented by S4 and T4 in Table 1). The $\Delta G^{\ddagger}$ for S4 is 11 kcal/mol less positive than T4, and the ΔG for S4 is 69 kcal/mol more negative than T4. Thus, S4 is favored over T4. For producing the second molecule of methanol, the singlet pathway is favored over the triplet pathway.

The mechanistic pathways shown in Figure 12 correspond to the production of CH_3OH in the experiments. Considering ΔG and $\Delta G^{\ddagger}$ for all the steps, the overall methane-to-methanol conversion seems to favor the singlet pathway. Our study includes $LCu^{II}OO\bullet$ and $LCu^{II}O\bullet$ as intermediates, both of which have been proposed as active species for hydrogen abstraction in a previous study[186].

2.3 Concluding Remarks

We report a facile strategy to construct a bio-inspired, thermally stable Cu-based catalyst supported by ZIF-8. The catalyst converts methane at 200 ℃ under 1 bar to methanol and formaldehyde with a ~70% selectivity, with the remainder being CO_2. Recycling tests showed 100% selectivity for methanol and formaldehyde from the third run onward. A

subset of the sites was found to be active for selective methane oxidation. The copper center is coordinated with up to four imidazolate ligands, but catalysis is attributed to copper sites with three imidazolate ligands. Density functional calculations show LCu^{I} is preferred to $LCu^{II}OH$ for conversion of methane to methanol. The catalytic cycles involve O_2-activated LCu^{I} reacting with two molecules of methane through subsequent hydrogen abstraction reactions and rebound reactions to produce two molecules of CH_3OH.

For the singlet and triplet pathways, the hydrogen abstraction results in H**…**C hydrogen bond formation (shown in S1 and S3 in Scheme 2, and T1 and T3 in Scheme 3), further followed by intermolecular rebound reactions (shown in S2 and S4 in Scheme 2, and T2 and T4 in Scheme 3) to produce two molecules of methanol. The Gibbs free energy barriers indicate that the methane conversion to methanol is more likely to follow the singlet pathway.

A continuous structural evolution from monomeric Cu^{II} to agglomerate CuO species induced by O_2 activation was observed through XAS, which might be correlated to the gradual stabilization of the reactivity and selectivity during recycling. We also infer that preferential concentration of Cu^{II} sites on the surface of ZIF-8 *via* post-synthetic transmetallation or hydrophilicity modulation of the ZIF support will be advantageous to improve the Cu utilization fraction in Cu-doped ZIF systems.

2.4 Supporting Information

EXPERIMENTAL DETAILS

Chemicals

Zinc(II) nitrate hexahydrate ($Zn(NO_3)_2{\cdot}6H_2O$), copper(II) nitrate hemi(pentahydrate) ($Cu(NO_3)_2{\cdot}2.5H_2O$), 2-methylimidazole (Hmim), and isopropanol (IPA) were purchased from Sigma Aldrich Chemicals Company, Inc. (Milwaukee, WI) and were used as received. Nitric acid, Cu and Zn ICP standards were purchased from Sigma Aldrich. Ultrapure deionized water (18.2 MB•cm resistivity) was obtained from a Millipore Milli-Q-Biocel A10 instrument (Millipore Inc., Billerica, MA).

X-Ray Absorption Spectroscopy

Cu K-edge (8979 eV) and Zn K-edge (9659 eV) X-ray absorption spectra were collected on the 5-BM-D bending magnet beamline of DND-CAT, at the Advanced Photon Source, Argonne National Laboratory. A Si (111) double-crystal monochromator was used for energy selection. The incident X-ray beam intensity was detuned to 50% of its maximum to minimize the presence of harmonics. Data was acquired in transmission/fluorescence mode using ionization chamber detectors (FMB-Oxford)/the PIPS detector (Canberra). A metal foil spectrum was acquired with each sample measurement for energy calibration. *Ex situ* samples were evenly dispersed onto Scotch tape, which was then folded to optimize the sample thickness, and the measurements were conducted at room temperature under open air. For the *in-situ* measurements, the Linkam THMS600 cell (Linkam scientific instruments Ltd., UK) was used. The powder sample was loaded into the through slot (2.5×6 mm2) of an aluminum coin (1 mm thick) and firmly pressed. The sample-loaded coin was placed onto the heating platen in the cell and kept in place with a stainless-steel retainer, and the stage was capped off airtight. Thermocouples were embedded in the heating platen below the aluminum coin and temperature was controlled with the THMS94 controller. The cell was first flushed with 20 sccm He for 10 minutes at room temperature. Then the temperature was ramped to 200 ℃ with a heating rate of 20 ℃/min under 20 sccm 20% O_2 and held for 1 h. After another He purging, 20 sccm CH_4 was introduced into the cell at 200 ℃ and held for 1 h. Then the cell was cooled down to 135 ℃ with He, and 3% water vapor carried by He was fed into the cell at 135 ℃ for 1 h. Afterwards, the chamber was cooled to room temperature under dry He. *In situ* XANES spectra were collected in fluorescence mode at various times to monitor the valence state of Cu species. Data analysis was performed using the Athena/Artemis/Hephaestus software package, which makes use of IFEFFIT.

Synthesis

The direct incorporation of Cu(II) ions into ZIF-8 was carried out following a modified procedure from Schejin *et al*.[187] A solution of Zinc(II) nitrate hexahydrate ($Zn(NO_3)_2{\cdot}6H_2O$) and copper(II) nitrate hemi(pentahydrate) ($Cu(NO_3)_2{\cdot}2.5H_2O$) (total 1

mmol), and a solution of Hmim (660 mg, 8 mmol), each in 11 mL IPA, were prepared separately. Then, the Cu/Zn solution with a desired Cu^{2+}: Zn^{2+} ratio was transferred to a three-neck flask and purged with N_2 for 10 min. Hmim solution was added dropwise by a syringe pump and the mixture was left at room temperature under N_2 for 1 h with vigorous stirring. The obtained grey powder was washed with excess IPA three times and dried under high vacuum at 120 ℃ overnight using a Micromeritics Smart VacPrep (SVP) instrument. $Cu_{10\%}$-ZIF, $Cu_{20\%}$-ZIF, and $Cu_{50\%}$-ZIF were obtained with a feeding ratio ($\frac{Cu}{Cu+Zn}$) of 15%, 25% and 50%, respectively.

Selective Methane Oxidation

The reactivities of as-synthesized materials were tested in a plug-flow reactor following a stepwise procedure. 100 mg catalyst diluted with high purity SiO_2 was packed on quartz wool in a stainless-steel reactor. The reactor temperature was controlled with a K-type thermocouple inserted into the catalyst bed. Water vapor was introduced through a bubbler located inside a hot box. The bubbler temperature was controlled by the hot box and further monitored with a K-type thermocouple attached to the bubbler. During the reactivity test, the material was first activated by 50 sccm O_2 at 200 ℃ for 3 h, followed by He purging for 30 min. Then 50 sccm CH_4 was fed into the reactor for 3 h. The reactor was cooled down to 135 ℃ under He and lastly, 15% water vapor carried by 50 sccm He was introduced to extract methanol and other oxidized products from the catalyst bed at 135 ℃ for 3 h. The temperature and pressure of CH_4 treatment step were varied to evaluate their impact on the catalytic performance. The oxidation products were identified and quantified using an online mass spectrometer (MS) and by monitoring the signals at *m/z* 28, 29, 31, 44, 45, characteristic for CO, formaldehyde, methanol, CO_2, and dimethyl ether, respectively. The He signal (*m/z* =4) was used as an internal standard. Yield and selectivity were determined by integrating the product concentrations as a function of time.

Characterization

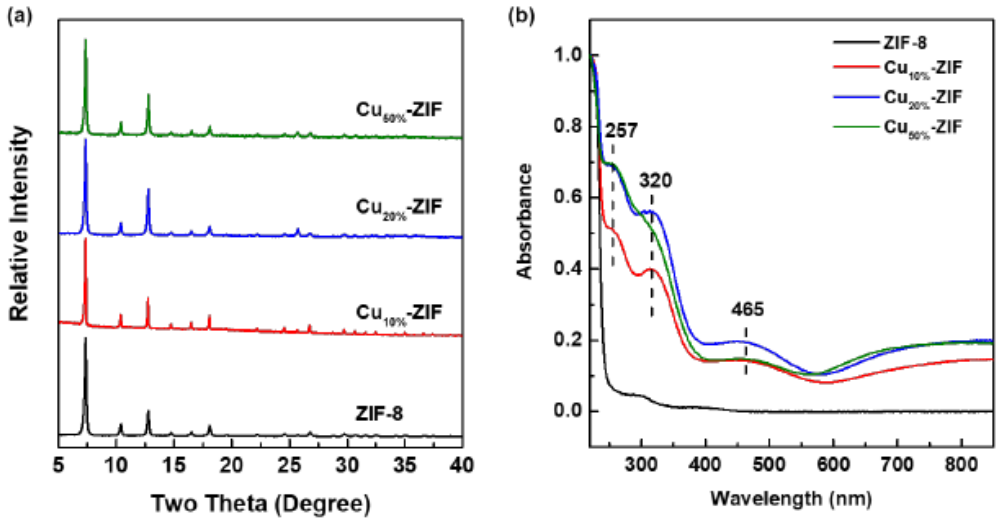

Figure S1. (a) PXRD patterns and (b) DRUV-Vis spectra of as-synthesized Cu(II)-doped ZIF-8. UV-Vis signals were normalized at 220 nm.

Table S1. Fitting Parameters of As-Synthesized Cu-ZIF-8

Sample	**Path**	**CN**	**R (Å)**	**σ² (Å2)**	χ_r^2	***R*-factor**	**Δ*E* (eV)**
$Cu_{20\%}$-ZIF	Cu-N/O	5.7(3)	1.984(5)	0.0037(7)	130.91	0.0224	3.8(5)
	Cu-C1	9(1)	3.11(1)	0.005(1)			
	Cu-C2	14(2)	3.52(1)	0.006(1)			
	Zn-N	3.9(2)	1.996(4)	0.0035(6)	136.63	0.0228	6.7(3)
	Zn-C1	4.7(6)	3.01(1)	0.002(1)			
	Zn-C2	5(1)	3.32(2)	0.011(4)			
	Zn-N-C	25(2)	4.211(9)	0.007(1)			
$Cu_{50\%}$-ZIF	Cu-N/O	6.4(4)	1.981(8)	0.0057(8)	113.88	0.0265	2.8(9)
	Cu-C1	7(1)	3.10(1)	0.004(2)			
	Cu-C2	16(2)	3.51(1)	0.008(2)			
	Zn-N	4.2(2)	1.987(4)	0.0040(6)	90.30	0.0226	5.4(3)
	Zn-C1	5.8(8)	3.02(1)	0.008(2)			
	Zn-C2	3.7(9)	3.40(2)	0.005(3)			
	Zn-N-C	22(4)	4.184(9)	0.007(3)			
$Cu_{50\%}$-ZIF-Cat-5X	Cu-O/N	3.51(8)	1.940(2)	0.0032(3)	19.55	0.0045	4.9(2)
	Cu-Cu	2.7(3)	2.922(8)	0.009(1)			

*CN: coordination number; R: bond distance; σ²: Debye-Waller factor; χ_r^2: reduced Chi-square; ΔE: energy shift.

Catalysis

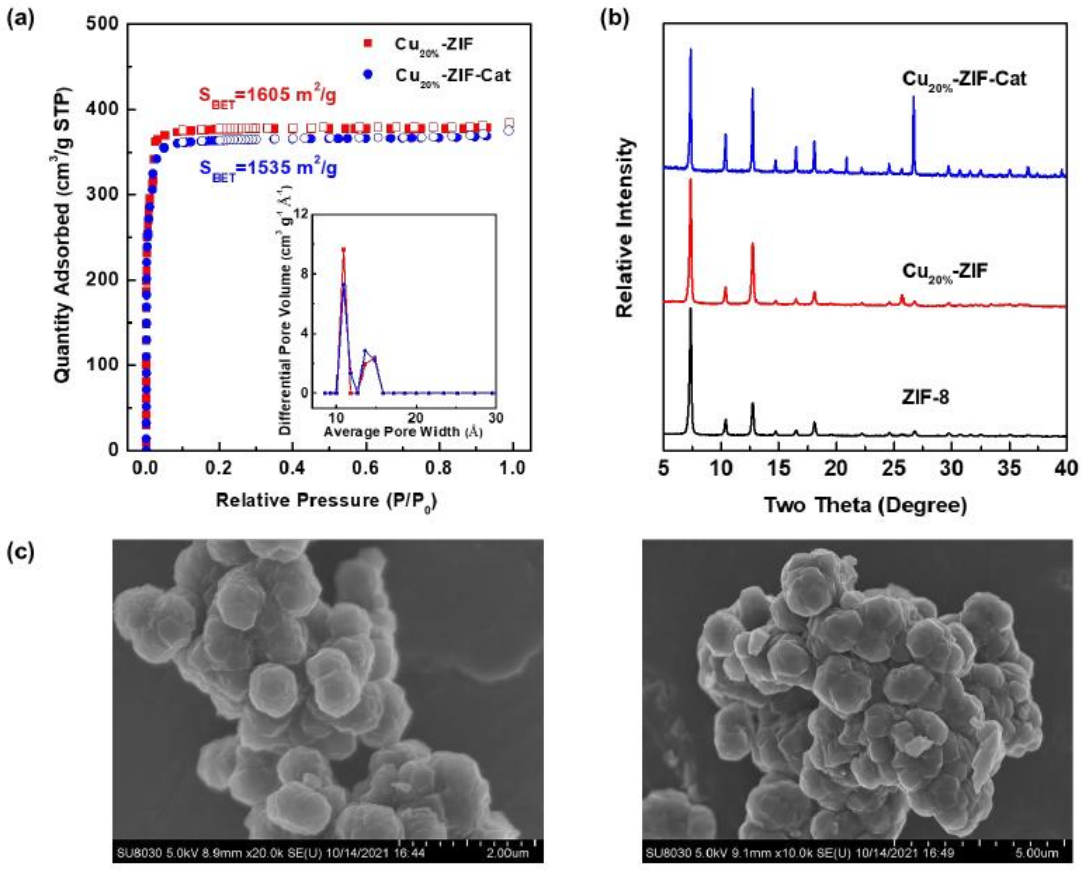

Figure S2. $Cu_{20\%}$-ZIF before and after catalysis (5 cycles): (a) N_2 adsorption-desorption isotherms at 77 K; closed symbols in the isotherm represent points collected during adsorption, and open symbols represent points collected during desorption. (b) PXRD patterns (the sharp peak at 27º comes from high-purity SiO_2 used during catalysis), and (c) scanning electron microscope (SEM) images.

CALCULATIONS

Computational Details

Density functional calculations were carried out in a locally modified version of *Gaussian 16*.[188] We used the def2-TZVP basis set[189,190] for Cu and Zn atoms and the def2-SVP basis set[3,4] for C, H, and O atoms. Geometry optimizations were performed with the revM06-L

exchange correlation density functional.[191] Frequency calculations were performed at the same level of theory to characterize the stationary points as intermediates or transition states and to calculate free energies. The minimum energy path was calculated at the same level of theory to verify the species linked by each transition state (TS). All free energies are calculated for a temperature of 200 °C and a pressure of 1 bar.

We first ran calculations on the triplets. All triplet calculations, which are always unrestricted, were stable. Special care was required for the singlet pathways. For TS1, TS2, and TS3, we used the wave function and geometry from the checkpoint files of optimized triplet TS structures as initial guesses to do `opt freq` unrestricted singlet calculations for TS1, TS2, and TS3. This yields unrestricted singlet calculations that converged for both geometry optimization and `stable=opt` stability check. Note that the TS energies are significantly lower when one obtains stable open-shell singlets than when one obtains unstable closed-shell singlets. (The energies are 14, 10, and 50 kcal/mol lower for TS1, TS2, and TS3 for stable open-shell singlets than for unstable closed-shell singlets). We ran intrinsic-reaction-coordinate (IRC) calculations (i.e., following the steepest-descent reaction path in isoinertial coordinates) starting at TS1, TS2, and TS3 and used the geometry from IRC calculations to optimize the reactants and products as open-shell singlets, except for the reactant of TS1 which is a closed-shell singlet. For TS4, we obtained restricted singlet calculations that converged for both geometry optimization and stable=opt stability check. We ran the IRC calculations starting at the TS and used the geometry from IRC calculations to optimize the product as a closed-shell singlet; stable=opt calculations show that these results are stable.

Thermodynamic Calculations

The Gibbs free energy of reaction (ΔG) and Gibbs free energy of activation ($\Delta G^{\ddagger}$) were calculated at 200 ºC with standard pressure of 1 atm (and with no solvent because the oxidation reaction is experimentally studied in the gas phase at 200 ºC). As usual, the sign convention is that reactions with more negative ΔG and less positive $\Delta G^{\ddagger}$ are more favorable. ΔG and $\Delta G^{\ddagger}$ are defined as

$$\Delta G = \sum (E + G_{\mathrm{RVE}}(T))_{\mathrm{products}} - \sum (E + G_{\mathrm{RVE}}(T))_{\mathrm{reactants}} \quad (1)$$

$$\Delta G^{\ddagger} = \sum (E + G_{\mathrm{RVE}}(T))_{\mathrm{transition\ state}} - \sum (E + G_{\mathrm{RVE}}(T))_{\mathrm{reactants}} \quad (2)$$

where T is the temperature, E is the total electronic energy including nuclear repulsion, and G_{RVE} is the contribution to G from vibration, rotation, and electronic degeneracy. The Gibbs free energies (G) of all optimized structures at 200 ºC are shown in **Table S2** and reaction profiles for steps 1 and 2 of each pathway are shown in Figure S3.

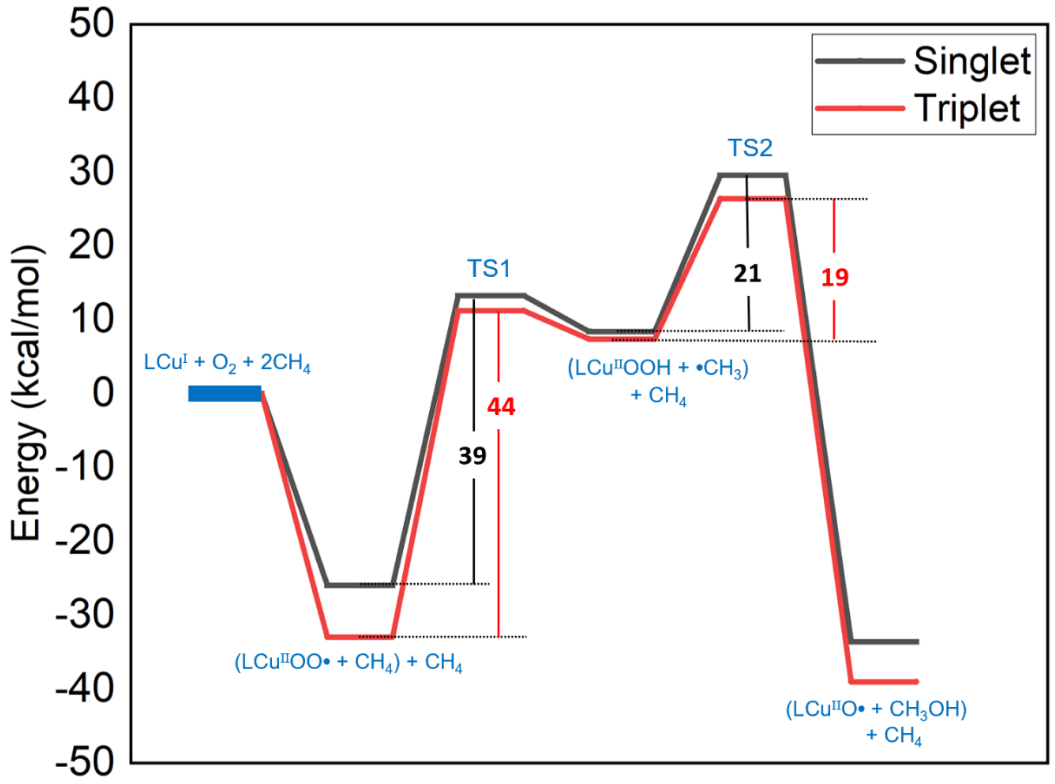

Figure S3. Comparison of the first two steps of the singlet and triplet mechanisms.

Table S2. Gibbs free energy (G) of all structures along the singlet and triplet pathways at 200 ºC and 1 atm.

	Structure	***G* (a.u.)**	
1	LCu^{I}	-2317.668791	
2	LCu^{II}OH	-2393.392292	
3	O_2	-150.113872	

4	OH	-75.644801	
5	CH_4	-40.434214	
6	CH_3OH	-115.552949	
	Singlet Pathway		***G* relative to structure 21 (kcal/mol)**
7	($LCu^{II}OO\bullet\ldots CH_4$)	-2508.258251	13.0
8	TS1	-2508.195709	52.3
9	($LCu^{II}OOH\ldots\bullet CH_3$)	-2508.203459	47.4
10	TS2	-2508.169766	68.6
11	($LCu^{II}O\bullet\ldots CH_3OH$)	-2508.270405	5.4
	Singlet Pathway		***G* relative to structure 16 (kcal/mol)**
12	($LCu^{II}O\bullet\ldots CH_4$)	-2433.139406	49.7
13	TS3	-2433.122999	60.0
14	($LCu^{II}OH\ldots\bullet CH_3$)	-2433.152507	41.5
15	TS4	-2433.093238	78.7
16	($LCu^{I}\ldots CH_3OH$)	-2433.218651	0.0
	Triplet Pathway		***G* relative to structure 21 (kcal/mol)**
17	($LCu^{II}OO\bullet\ldots CH_4$)	-2508.269388	6.1
18	TS1	-2508.198981	50.2
19	($LCu^{II}OOH\ldots\bullet CH_3$)	-2508.205106	46.4
20	TS2	-2508.174826	65.4
21	($LCu^{II}O\bullet\ldots CH_3OH$)	-2508.279041	0.0
	Triplet Pathway		***G* relative to structure 16 (kcal/mol)**
22	($LCu^{II}O\bullet\ldots CH_4$)	-2433.150874	42.5
23	TS3	-2433.127924	56.9
24	($LCu^{II}OH\ldots\bullet CH_3$)	-2433.154968	40.0
25	TS4	-2433.078466	88.0
26	($LCu^{I}\ldots CH_3OH$)	-2433.111250	67.4

Structures along the reaction path

Electronic configuration of Cu: $[Ar]3d^{10}4s^{1}$

Electronic configuration of Cu^{I} : $[Ar]3d^{10}$

Electronic configuration of Cu^{II} : $[Ar]3d^{9}$

Selected bond distances of the optimized structures are shown in **Table S3**. Up to the production of the first molecule of methanol, we provide two Cu-O distances: one for the

closest oxygen and the other for the farthest oxygen. The Cu-C distance can be correlated with the open-shell nature of the structures having a methyl center with an unpaired electron.

LCu^{I} reacts with O_2 to form a side-on $LCu^{II}OO\bullet$ singlet species or an end-on $LCu^{II}OO\bullet$ triplet species, which reacts with CH_4 to form a singlet or triplet $LCu^{II}OO\bullet\ldots CH_4$. The singlet $LCu^{II}OO\bullet\ldots CH_4$ i.e., the van der Waals (vdW) complex of side-on $LCu^{II}OO\bullet$ singlet species and CH_4 has two similar Cu-O distances (as shown in **Table S3**). The triplet $LCu^{II}OO\bullet\ldots CH_4$ i.e., the vdW complex of end-on $LCu^{II}OO\bullet$ triplet species and CH_4 has one longer Cu-O distance (as shown in **Table S3**). In the singlet $LCu^{II}OO\bullet\ldots CH_4$, the Cu center has one unpaired electron, and the other unpaired electron is over the two oxygen centers. The two unpaired electrons occupy the same spatial orbital to give a closed-shell singlet. In the triplet $LCu^{II}OO\bullet\ldots CH_4$, the Cu center has one unpaired electron, and the oxygen center has one unpaired electron. They combine to form a triplet $LCu^{II}OO\bullet\ldots CH_4$.

Then $LCu^{II}OO\bullet$ abstracts a hydrogen atom from CH_4 to produce $LCu^{II}OOH\ldots\bullet CH_3$ (Big Cu-C distances shown in **Table S3** imply the unpaired electrons are in different spatial orbitals). In $LCu^{II}OOH\ldots\bullet CH_3$, the Cu center has one unpaired electron, and the methyl center has one unpaired electron. They combine to produce an open-shell singlet or a triplet $LCu^{II}OOH\ldots\bullet CH_3$. The open-shell singlet TS1 connects open-shell singlet $LCu^{II}OO\bullet\ldots CH_4$ to open-shell singlet $LCu^{II}OOH\ldots\bullet CH_3$. The triplet TS1 connects triplet $LCu^{II}OO\bullet\ldots CH_4$ to triplet $LCu^{II}OOH\ldots\bullet CH_3$.

Then OH rebounds to form $LCu^{II}O\bullet\ldots CH_3OH$. In $LCu^{II}O\bullet\ldots CH_3OH$, the Cu center has one unpaired electron, and the oxygen center has one unpaired electron. They combine to form an open-shell singlet or a triplet $LCu^{II}O\bullet\ldots CH_3OH$. The open-shell singlet TS2 connects open-shell singlet $LCu^{II}OOH\ldots\bullet CH_3$ to open-shell singlet $LCu^{II}O\bullet\ldots CH_3OH$. The triplet TS2 connects triplet $LCu^{II}OOH\ldots\bullet CH_3$ to triplet $LCu^{II}O\bullet\ldots CH_3OH$. The first molecule of methanol is produced at this point.

Next, the second CH_4 molecule reacts with $LCu^{II}O\bullet$ to form $LCu^{II}O\bullet\ldots CH_4$. In $LCu^{II}O\bullet\ldots CH_4$, the Cu center has one unpaired electron, and the oxygen center has one unpaired electron. They combine to form an open-shell singlet or a triplet $LCu^{II}O\bullet\ldots CH_4$.

Then $LCu^{II}O\bullet$ abstracts a hydrogen atom from CH_4 to produce $LCu^{II}OH\ldots\bullet CH_3$ (Big Cu-C distances shown in **Table S3** imply the unpaired electrons are in different spatial orbitals). In $LCu^{II}OH\ldots\bullet CH_3$, the Cu center has one unpaired electron, and the methyl center has one unpaired electron. They combine to form an open-shell singlet or triplet $LCu^{II}OH\ldots\bullet CH_3$. The open-shell singlet TS3 connects open-shell singlet $LCu^{II}O\bullet\ldots CH_4$ to open-shell singlet $LCu^{II}OH\ldots\bullet CH_3$. The triplet TS3 connects triplet $LCu^{II}O\bullet\ldots CH_4$ to triplet $LCu^{II}OH\ldots\bullet CH_3$.

Then OH rebounds to form $LCu^{II}O\bullet\ldots CH_3OH$. For singlet, the final product $LCu^{I}\ldots CH_3OH$ is a closed shell singlet. A closed-shell singlet TS4 connects open-shell singlet $LCu^{II}OH\ldots\bullet CH_3$ to closed-shell singlet $LCu^{I}\ldots CH_3OH$. The triplet TS4 connects triplet $LCu^{II}OH\ldots\bullet CH_3$ to triplet $LCu^{I}\ldots CH_3OH$. The second molecule of methanol is produced at this point. For singlets, TS4 and the final product $LCu^{I}\ldots CH_3OH$ are found to be closed shell singlets. Cu^{I} is a closed-shell singlet and CH_3OH is a closed-shell singlet. This is consistent with the final singlet product ($LCu^{I}\ldots CH_3OH$) being a closed-shell singlet. An interesting geometrical difference between the singlet and the triplet pathway is observed for TS4 with regards to the Cu-C distance. The Cu-C distance for the closed-shell singlet TS4 is 2.14 Å, which is much lower than the Cu-C distance (3.31 Å) for the triplet TS4 (shown in **Table S3**). From **Table S3**, we can see that Cu-O distance between Cu^{II} and the closest O is in the range 1.78–1.88 Å. However, the Cu-O distances between Cu^{I} and the closest O are larger (2.74 Å and 3.19 Å); in terms of Cu-O distance, the Cu in TS4 resembles Cu^{II} more than Cu^{I}. We know that Cu^{II} has one unpaired electron. Since the Cu-C distance for singlet TS4 is very low (2.14 Å), the unpaired electron on methyl in TS4 can combine with the unpaired electron on Cu center and occupy the same spatial orbital, giving rise to a closed-shell singlet. This is a geometrical validation of our closed-shell singlet TS4. For the singlet pathway, the mechanism goes through the open-shell singlets

until the closed-shell singlet TS4, which gives the closed-shell singlet final product $LCu^{I}…CH_3OH$.

Our mechanistic pathway (as shown in Figure 12) can be written as:

$$LCu^{I} + O_2 + 2CH_4 \rightarrow (LCu^{I}…CH_3OH) + CH_3OH \quad (I)$$

The ΔG of reaction (I) is -75.6 kcal/mol for the singlet pathway and -8.2 kcal/mol for the triplet pathway. Reaction (I) can be compared with

$$LCu^{I} + O_2 + 2CH_4 \rightarrow LCu^{I} + 2CH_3OH \quad (II)$$

The ΔG of reaction (II) is -77.6 kcal/mol. The comparison between the ΔG of reaction (I) and that of reaction (II) shows that the final singlet product of (I) is energetically very close to that of (II), and it shows the reasonableness of the singlet pathway for the overall methane-to-methanol conversion. As discussed in the manuscript proper, the singlet pathway is preferred over the triplet pathway based on the ΔG and $\Delta G^{‡}$ values of all the steps.

Table S3: Bond distances of structures along the singlet and triplet pathways

	Singlet Pathway	**Cu-O (**Å) (Closest O)	**Cu-O (**Å**)** (Farthest O)	**Cu-C (**Å**)**
7	($LCu^{II}OO\bullet\ldots CH_4$)	1.86	1.87	3.52
8	TS1	1.88	2.78	3.46
9	($LCu^{II}OOH\ldots\bullet CH_3$)	1.88	2.84	3.56
10	TS2	1.86	2.25	3.80
11	($LCu^{II}O\bullet\ldots CH_3OH$)	1.88	2.25	3.11
	Singlet Pathway			
12	($LCu^{II}O\bullet\ldots CH_4$)	1.79	-	4.50
13	TS3	1.82	-	3.52
14	($LCu^{II}OH\ldots\bullet CH_3$)	1.84	-	3.14
15	TS4	1.92	-	2.15
16	($LCu^{I}\ldots CH_3OH$)	2.74		3.39
	Triplet Pathway			
17	($LCu^{II}OO\bullet\ldots CH_4$)	1.93	2.82	4.06
18	TS1	1.89	2.79	3.46
19	($LCu^{II}OOH\ldots\bullet CH_3$)	1.88	2.84	3.55
20	TS2	1.87	2.24	3.84
21	($LCu^{II}O\bullet\ldots CH_3OH$)	1.87	2.24	3.12
	Triplet Pathway			
22	($LCu^{II}O\bullet\ldots CH_4$)	1.78	-	4.41
23	TS3	1.81	-	3.57
24	($LCu^{II}OH\ldots\bullet CH_3$)	1.84	-	3.39
25	TS4	1.96	-	3.31
26	($LCu^{I}\ldots CH_3OH$)	3.19	-	4.00

Bibliography

[114] Yuan, J.; Luo, D.; Feng, L., A Review of the Technical and Economic Evaluation Techniques for Shale Gas Development. *Appl. Energ.* **2015,** *148*, 49-65.

[115] Kerr, R. A., Natural Gas from Shale Bursts onto the Scene. *Science* **2010,** *328*, 1624-1626.

[116] Hammond, C.; Conrad, S.; Hermans, I., Oxidative Methane Upgrading. *ChemSusChem* **2012,** *5*, 1668-1686.

[117] Wang, V. C. C.; Maji, S.; Chen, P. P. Y.; Lee, H. K.; Yu, S. S. F.; Chan, S. I., Alkane Oxidation: Methane Monooxygenases, Related Enzymes, and Their Biomimetics. *Chem. Rev.* **2017,** *117*, 8574-8621.

[118] Dinh, K. T.; Sullivan, M. M.; Serna, P.; Meyer, R. J.; Dincă, M.; Román-Leshkov, Y., Viewpoint on the Partial Oxidation of Methane to Methanol Using Cu- and Fe-Exchanged Zeolites. *ACS Catal.* **2018,** *8*, 8306-8313.

[119] Balasubramanian, R.; Smith, S. M.; Rawat, S.; Yatsunyk, L. A.; Stemmler, T. L.; Rosenzweig, A. C., Oxidation of Methane by a Biological Dicopper Centre. *Nature* **2010,** *465*, 115-119.

[120] Cao, L.; Caldararu, O.; Rosenzweig, A. C.; Ryde, U., Quantum Refinement does not Support Dinuclear Copper Sites in Crystal Structures of Particulate Methane Monooxygenase. *Angew. Chem. Int. Ed.* **2018,** *57*, 162-166.

[121] Ross, M. O.; MacMillan, F.; Wang, J.; Nisthal, A.; Lawton, T. J.; Olafson, B. D.; Mayo, S. L.; Rosenzweig, A. C.; Hoffman, B. M., Particulate Methane Monooxygenase Contains Only Mononuclear Copper Centers. *Science* **2019,** *364*, 566.

[122] Jodts, R. J.; Ross, M. O.; Koo, C. W.; Doan, P. E.; Rosenzweig, A. C.; Hoffman, B. M., Coordination of the Copper Centers in Particulate Methane Monooxygenase: Comparison between Methanotrophs and Characterization of the CuC Site by EPR and ENDOR Spectroscopies. *J. Am. Chem. Soc.* **2021,** *143*, 15358-15368.

[123] Sushkevich, V. L.; Palagin, D.; van Bokhoven, J. A., The Effect of the Active-Site Structure on the Activity of Copper Mordenite in the Aerobic and Anaerobic Conversion of Methane into Methanol. *Angew. Chem. Int. Ed.* **2018,** *57*, 8906-8910.

[124] Meyet, J.; Searles, K.; Newton, M. A.; Worle, M.; van Bavel, A. P.; Horton, A. D.; van Bokhoven, J. A.; Coperet, C., Monomeric Copper(II) Sites Supported on Alumina Selectively Convert Methane to Methanol. *Angew. Chem. Int. Ed.* **2019,** *58*, 9841-9845.

[125] Woertink, J. S.; Smeets, P. J.; Groothaert, M. H.; Vance, M. A.; Sels, B. F.; Schoonheydt, R. A.; Solomon, E. I., A $[Cu_2O]^{2+}$ Core in Cu-ZSM-5, the Active Site in the Oxidation of Methane to Methanol. *Proc. Natl. Acad. Sci. U. S. A.* **2009,** *106*, 18908.

[126] Smeets, P. J.; Hadt, R. G.; Woertink, J. S.; Vanelderen, P.; Schoonheydt, R. A.; Sels, B. F.; Solomon, E. I., Oxygen Precursor to the Reactive Intermediate in Methanol Synthesis by Cu-ZSM-5. *J. Am. Chem. Soc.* **2010,** *132*, 14736-14738.

[127] Sushkevich, V. L.; Palagin, D.; Ranocchiari, M.; van Bokhoven, J. A., Selective Anaerobic Oxidation of Methane Enables Direct Synthesis of Methanol. *Science* **2017,** *356*, 523-527.

[128] Grundner, S.; Markovits, M. A. C.; Li, G.; Tromp, M.; Pidko, E. A.; Hensen, E. J. M.; Jentys, A.; Sanchez-Sanchez, M.; Lercher, J. A., Single-Site Trinuclear Copper Oxygen Clusters in Mordenite for Selective Conversion of Methane to Methanol. *Nat. Commun.* **2015,** *6*, 7546-7554.

[129] Tomkins, P.; Mansouri, A.; Bozbag, S. E.; Krumeich, F.; Park, M. B.; Alayon, E. M. C.; Ranocchiari, M.; van Bokhoven, J. A., Isothermal Cyclic Conversion of Methane into Methanol over Copper-Exchanged Zeolite at Low Temperature. *Angew. Chem. Int. Ed.* **2016,** *55*, 5467-5471.

[130] Sun, L.; Wang, Y.; Wang, C.; Xie, Z.; Guan, N.; Li, L., Water-Involved Methane-Selective Catalytic Oxidation by Dioxygen over Copper Zeolites. *Chem* **2021,** *7*, 1557-1568.

[131] Pappas, D. K.; Martini, A.; Dyballa, M.; Kvande, K.; Teketel, S.; Lomachenko, K. A.; Baran, R.; Glatzel, P.; Arstad, B.; Berlier, G.; Lamberti, C.; Bordiga, S.; Olsbye, U.; Svelle, S.; Beato, P.; Borfecchia, E., The Nuclearity of the Active Site for Methane to Methanol Conversion in Cu-Mordenite: A Quantitative Assessment. *J. Am. Chem. Soc.* **2018,** *140*, 15270-15278.

[132] Bour, J. R.; Wright, A. M.; He, X.; Dinca, M., Bioinspired Chemistry at MOF Secondary Building Units. *Chem. Sci.* **2020,** *11*, 1728-1737.

[133] Liu, J.; Goetjen, T. A.; Wang, Q.; Knapp, J. G.; Wasson, M. C.; Yang, Y.; Syed, Z. H.; Delferro, M.; Notestein, J. M.; Farha, O. K.; Hupp, J. T., MOF-Enabled Confinement and Related Effects for Chemical Catalyst Presentation and Utilization. *Chem. Soc. Rev.* **2022,** *51*, 1045-1097.

[134] Ji, Z.; Wang, H.; Canossa, S.; Wuttke, S.; Yaghi, O. M., Pore Chemistry of Metal–Organic Frameworks. *Adv. Funct. Mater.* **2020,** *30*, 2000238.

[135] Cai, G.; Yan, P.; Zhang, L.; Zhou, H.-C.; Jiang, H.-L., Metal–Organic Framework-Based Hierarchically Porous Materials: Synthesis and Applications. *Chem. Rev.* **2021,** *121*, 12278-12326.

[136] Guillerm, V.; Eddaoudi, M., The Importance of Highly Connected Building Units in Reticular Chemistry: Thoughtful Design of Metal–Organic Frameworks. *Acc. Chem. Res.* **2021,** *54*, 3298-3312.

[137] Guo, P.; Froese, C.; Fu, Q.; Chen, Y.-T.; Peng, B.; Kleist, W.; Fischer, R. A.; Muhler, M.; Wang, Y., CuPd Mixed-Metal HKUST-1 as a Catalyst for Aerobic Alcohol Oxidation. *J. Phys. Chem. C* **2018,** *122*, 21433-21440.

[138] Xiao, D. J.; Bloch, E. D.; Mason, J. A.; Queen, W. L.; Hudson, M. R.; Planas, N.; Borycz, J.; Dzubak, A. L.; Verma, P.; Lee, K.; Bonino, F.; Crocella, V.; Yano, J.; Bordiga, S.; Truhlar, D. G.; Gagliardi, L.; Brown, C. M.; Long, J. R., Oxidation of Ethane to Ethanol by N_2O in a Metal-Organic Framework with Coordinatively Unsaturated Iron(II) Sites. *Nat. Chem.* **2014,** *6*, 590-5.

[139] Osadchii, D. Y.; Olivos-Suarez, A. I.; Szécsényi, Á.; Li, G.; Nasalevich, M. A.; Dugulan, I. A.; Crespo, P. S.; Hensen, E. J. M.; Veber, S. L.; Fedin, M. V.; Sankar, G.; Pidko, E. A.; Gascon, J., Isolated Fe Sites in Metal Organic Frameworks Catalyze the Direct Conversion of Methane to Methanol. *ACS Catal.* **2018,** *8*, 5542-5548.

[140] Sun, C.; Skorupskii, G.; Dou, J.-H.; Wright, A. M.; Dincă, M., Reversible Metalation and Catalysis with a Scorpionate-like Metallo-ligand in a Metal–Organic Framework. *J. Am. Chem. Soc.* **2018,** *140*, 17394-17398.

[141] He, X.; Looker, B. G.; Dinh, K. T.; Stubbs, A. W.; Chen, T.; Meyer, R. J.; Serna, P.; Román-Leshkov, Y.; Lancaster, K. M.; Dincă, M., Cerium(IV) Enhances the Catalytic Oxidation Activity of Single-Site Cu Active Sites in MOFs. *ACS Catal.* **2020,** *10*, 7820-7825.

[142] Yang, Y.; Zhang, X.; Kanchanakungwankul, S.; Lu, Z.; Noh, H.; Syed, Z. H.; Farha, O. K.; Truhlar, D. G.; Hupp, J. T., Unexpected "Spontaneous" Evolution of Catalytic, MOF-Supported Single Cu(II) Cations to Catalytic, MOF-Supported Cu(0) Nanoparticles. *J. Am. Chem. Soc.* **2020,** *142*, 21169-21177.

[143] Manna, K.; Zhang, T.; Lin, W., Postsynthetic Metalation of Bipyridyl-Containing Metal–Organic Frameworks for Highly Efficient Catalytic Organic Transformations. *J. Am. Chem. Soc.* **2014,** *136*, 6566-6569.

[144] Zhang, X.; Vermeulen, N. A.; Huang, Z.; Cui, Y.; Liu, J.; Krzyaniak, M. D.; Li, Z.; Noh, H.; Wasielewski, M. R.; Delferro, M.; Farha, O. K., Effect of Redox "Non-Innocent" Linker on the Catalytic Activity of Copper-Catecholate-Decorated Metal–Organic Frameworks. *ACS Appl. Mater. Interfaces* **2018,** *10*, 635-641.

[145]Yuan, S.; Qin, J. S.; Li, J.; Huang, L.; Feng, L.; Fang, Y.; Lollar, C.; Pang, J.; Zhang, L.; Sun, D.; Alsalme, A.; Cagin, T.; Zhou, H. C., Retrosynthesis of Multi-Component Metal−Organic Frameworks. *Nat. Commun.* **2018,** *9*, 808.

[146] Yang, Y.; Noh, H.; Ma, Q.; Wang, R.; Chen, Z.; Schweitzer, N. M.; Liu, J.; Chapman, K. W.; Hupp, J. T., Engineering Dendrimer-Templated, Metal–Organic Framework-Confined Zero-Valent, Transition-Metal Catalysts. *ACS Appl. Mater. Interfaces* **2021,** *13*, 36232-36239.

[147] Luo, Y.; Fan, S.; Yu, W.; Wu, Z.; Cullen, D. A.; Liang, C.; Shi, J.; Su, C., Fabrication of $Au_{25}(SG)_{18}$–ZIF-8 Nanocomposites: A Facile Strategy to Position $Au_{25}(SG)_{18}$ Nanoclusters Inside and Outside ZIF-8. *Adv. Mater.* **2018,** *30*, 1704576.

[148] Buru, C. T.; Farha, O. K., Strategies for Incorporating Catalytically Active Polyoxometalates in Metal–Organic Frameworks for Organic Transformations. *ACS Appl. Mater. Interfaces* **2020,** *12*, 5345-5360.

[149] Ji, S.; Chen, Y.; Zhao, S.; Chen, W.; Shi, L.; Wang, Y.; Dong, J.; Li, Z.; Li, F.; Chen, C.; Peng, Q.; Li, J.; Wang, D.; Li, Y., Atomically Dispersed Ruthenium Species Inside Metal-Organic Frameworks: Combining the High Activity of Atomic Sites and the Molecular Sieving Effect of MOFs. *Angew. Chem. Int. Ed.* **2019,** *58*, 4271-4275.

[150] Ikuno, T.; Zheng, J.; Vjunov, A.; Sanchez-Sanchez, M.; Ortuño, M. A.; Pahls, D. R.; Fulton, J. L.; Camaioni, D. M.; Li, Z.; Ray, D.; Mehdi, B. L.; Browning, N. D.; Farha, O. K.; Hupp, J. T.; Cramer, C. J.; Gagliardi, L.; Lercher, J. A., Methane Oxidation to Methanol Catalyzed by Cu-Oxo Clusters Stabilized in NU-1000 Metal–Organic Framework. *J. Am. Chem. Soc.* **2017,** *139*, 10294-10301.

[151] Zheng, J.; Ye, J.; Ortuño, M. A.; Fulton, J. L.; Gutiérrez, O. Y.; Camaioni, D. M.; Motkuri, R. K.; Li, Z.; Webber, T. E.; Mehdi, B. L.; Browning, N. D.; Penn, R. L.; Farha, O. K.; Hupp, J. T.; Truhlar, D. G.; Cramer, C. J.; Lercher, J. A., Selective Methane Oxidation to Methanol on Cu-Oxo Dimers Stabilized by Zirconia Nodes of an NU-1000 Metal–Organic Framework. *J. Am. Chem. Soc.* **2019,** *141*, 9292-9304.

[152] Ji, S.; Chen, Y.; Zhao, S.; Chen, W.; Shi, L.; Wang, Y.; Dong, J.; Li, Z.; Li, F.; Chen, C.; Peng, Q.; Li, J.; Wang, D.; Li, Y., Atomically Dispersed Ruthenium Species Inside Metal-Organic Frameworks: Combining the High Activity of Atomic Sites and the Molecular Sieving Effect of MOFs. *Angew. Chem. Int. Ed.* **2019,** *58*, 4271-4275.

[153] Schejn, A.; Aboulaich, A.; Balan, L.; Falk, V.; Lalevée, J.; Medjahdi, G.; Aranda, L.; Mozet, K.; Schneider, R., Cu^{2+}-doped Zeolitic Imidazolate Frameworks (ZIF-8): Efficient and Stable Catalysts for Cycloadditions and Condensation Reactions. *Catal. Sci. Technol.* **2015,** *5*, 1829-1839.

[154] Park, K. S.; Ni, Z.; Côté, A. P.; Choi, J. Y.; Huang, R.; Uribe-Romo, F. J.; Chae, H. K.; O'Keeffe, M.; Yaghi, O. M., Exceptional Chemical and Thermal Stability of Zeolitic Imidazolate Frameworks. *Proc. Natl. Acad. Sci. U.S.A.* **2006,** *103*, 10186-10191.

[155] Huang, X. C.; Lin, Y. Y.; Zhang, J. P.; Chen, X. M., Ligand-Directed Strategy for Zeolite-Type Metal–Organic Frameworks: Zinc(II) Imidazolates with Unusual Zeolitic Topologies. *Angew. Chem. Int. Ed.* **2006,** *45*, 1557-1559.

[156] Fairen-Jimenez, D.; Galvelis, R.; Torrisi, A.; Gellan, A. D.; Wharmby, M. T.; Wright, P. A.; Mellot-Draznieks, C.; Duren, T., Flexibility and Swing Effect on the Adsorption of Energy-Related Gases on ZIF-8: Combined Experimental and Simulation Study. *Dalton Trans.* **2012,** *41*, 10752-62.

[157] Fairen-Jimenez, D.; Moggach, S. A.; Wharmby, M. T.; Wright, P. A.; Parsons, S.; Düren, T., Opening the Gate: Framework Flexibility in ZIF-8 Explored by Experiments and Simulations. *J. Am. Chem. Soc.* **2011,** *133*, 8900-8902.

[158] Hobday, C. L.; Woodall, C. H.; Lennox, M. J.; Frost, M.; Kamenev, K.; Düren, T.; Morrison, C. A.; Moggach, S. A., Understanding the Adsorption Process in ZIF-8 Using High Pressure Crystallography and Computational Modelling. *Nat. Commun.* **2018,** *9*, 1429.

[159] Li, R.; Ren, X.; Ma, H.; Feng, X.; Lin, Z.; Li, X.; Hu, C.; Wang, B., Nickel-Substituted Zeolitic Imidazolate Frameworks for Time-Resolved Alcohol Sensing and Photocatalysis under Visible Light. *J. Mater. Chem. A* **2014,** *2*, 5724-5729.

[160] Dai, Y.; Xing, P.; Cui, X.; Li, Z.; Zhang, X., Coexistence of Cu(II) and Cu(I) in Cu Ion-Doped Zeolitic Imidazolate Frameworks (ZIF-8) for the Dehydrogenative Coupling of Silanes with Alcohols. *Dalton Trans.* **2019,** *48*, 16562-16568.

[161] Zhang, Y.; Xie, Z.; Wang, Z.; Feng, X.; Wang, Y.; Wu, A., Unveiling the Adsorption Mechanism of Zeolitic Imidazolate Framework-8 with High Efficiency for Removal of Copper Ions from Aqueous Solutions. *Dalton Trans.* **2016,** *45*, 12653-12660.

[162] Wang, T.; Wang, Y.; Sun, M.; Hanif, A.; Wu, H.; Gu, Q.; Ok, Y. S.; Tsang, D. C. W.; Li, J.; Yu, J.; Shang, J., Thermally Treated Zeolitic Imidazolate Framework-8 (ZIF-8) for Visible Light Photocatalytic Degradation of Gaseous Formaldehyde. *Chem. Sci.* **2020,** *11*, 6670-6681.

[163] Hafez, R. S.; El-Khiyami, S., Effect of Copper (II) Nitrate $3H_2O$ on the Crystalline, Optical and Electrical Properties of Poly(Vinyl Alcohol) Films. *J. Polym. Res.* **2020,** *27*, 26.

[164] Borfecchia, E.; Lomachenko, K. A.; Giordanino, F.; Falsig, H.; Beato, P.; Soldatov, A. V.; Bordiga, S.; Lamberti, C., Revisiting the Nature of Cu Sites in the Activated Cu-SSZ-13 Catalyst for SCR Reaction. *Chem. Sci.* **2015,** *6*, 548-563.

[165] Borfecchia, E.; Lomachenko, K. A.; Giordanino, F.; Falsig, H.; Beato, P.; Soldatov, A. V.; Bordiga, S.; Lamberti, C., Revisiting the Nature of Cu Sites in the Activated Cu-SSZ-13 Catalyst for SCR Reaction. *Chem. Sci.* **2015,** *6*, 548-563.

[166] Ikuno, T.; Grundner, S.; Jentys, A.; Li, G.; Pidko, E. A.; Fulton, J. L.; Sanchez-Sanchez, M.; Lercher, J. A., Formation of Active Cu-oxo Clusters for Methane Oxidation in Cu-Exchanged Mordenite. *J. Phys. Chem. C* **2019**, *123*, 8759-8769

[167] Zhang, K.; Lively, R. P.; Zhang, C.; Koros, W. J.; Chance, R. R., Investigating the Intrinsic Ethanol/Water Separation Capability of ZIF-8: An Adsorption and Diffusion Study. *J. Phys. Chem. C* **2013,** *117*, 7214-7225.

[168] Han, C.; Verploegh, R. J.; Sholl, D. S., Assessing the Impact of Point Defects on Molecular Diffusion in ZIF-8 Using Molecular Simulations. *J. Phys. Chem. Lett.* **2018,** *9*, 4037-4044.

[169] Zhang, C.; Han, C.; Sholl, D. S.; Schmidt, J. R., Computational Characterization of Defects in Metal–Organic Frameworks: Spontaneous and Water-Induced Point Defects in ZIF-8. *J. Phys. Chem. Lett.* **2016,** *7*, 459-464.

[170] Chufán, E. E.; Prigge, S. T.; Siebert, X.; Eipper, B. A.; Mains, R. E.; Amzel, L. M., Differential Reactivity between Two Copper Sites in Peptidylglycine α-Hydroxylating Monooxygenase. *J. Am. Chem. Soc.* **2010**, *132*, 15565-15572.

[171] Liu, J. J. ; Diaz, D. E. ; Quist, D. A. ; Karlin, K. D., Copper(I)-Dioxygen Adducts and Copper Enzyme Mechanisms. *Isr. J. Chem.* **2016,** *56* (9-10), 738-755.

[172] Cowley, R. E. ; Tian, L ; Solomon, E. I., Mechanism of O_2 activation and substrate hydroxylation in noncoupled binuclear copper monooxygenases. *Proc. Natl. Acad. Sci. U.S.A.* **2016,** *113*, 12035-12040.

[173] Baek, J.; Rungtaweevoranit, B.; Pei, X.; Park, M.; Fakra, S. C.; Liu, Y.-S.; Matheu, R.; Alshmimri, S. A.; Alshehri, S.; Trickett, C. A.; Somorjai, G. A.; Yaghi, O. M., Bioinspired Metal–Organic Framework Catalysts for Selective Methane Oxidation to Methanol. *J. Am. Chem. Soc.* **2018,** *140*, 18208-18216.

[174] Li, Y.M.; Yuan, J.; Ren, H.; Ji, C.Y.; Tao, Y.; Wu, Y.; Chou, L.Y.; Zhang, Y.-B.; Cheng, L., Fine-Tuning the Micro-Environment to Optimize the Catalytic Activity of Enzymes Immobilized in Multivariate Metal–Organic Frameworks. *J. Am. Chem. Soc.* **2021,** *143*, 15378-15390.

[175] Dinh, K. T.; Sullivan, M. M.; Narsimhan, K.; Serna, P.; Meyer, R. J.; Dinca, M.; Roman-Leshkov, Y., Continuous Partial Oxidation of Methane to Methanol Catalyzed by Diffusion-Paired Cu Dimers in Copper-Exchanged Zeolites. *J. Am. Chem. Soc.* **2019,** *141*, 11641-11650

[176] Brezicki, G.; Kammert, J. D.; Gunnoe, T. B.; Paolucci, C.; Davis, R. J., Insights into the Speciation of Cu in the Cu-H-Mordenite Catalyst for the Oxidation of Methane to Methanol. *ACS Catal.* **2019,** *9*, 5308-5319.

[177] Sushkevich, V. L.; van Bokhoven, J. A., Kinetic Study and Effect of Water on Methane Oxidation to Methanol over Copper-Exchanged Mordenite. *Catal. Sci. Technol.* **2020,** *10*, 382-390.

[178] Zheng, J.; Lee, I.; Khramenkova, E.; Wang, M.; Peng, B.; Gutierrez, O. Y.; Fulton, J. L.; Camaioni, D. M.; Khare, R.; Jentys, A.; Haller, G. L.; Pidko, E. A.; Sanchez-Sanchez, M.; Lercher, J. A., Importance of Methane Chemical Potential for Its Conversion to Methanol on Cu-Exchanged Mordenite. *Chem. Eur. J.* **2020,** *26*, 7563-7567.

[179] Takemoto, T.; Tabata, K.; Teng, Y.; Nakayama, A.; Suzuki, E., The Effects of Reaction Pressures on the Production of Methanol through the Selective Oxidation of Methane in CH4–O_2–NO_x (x=1 or 2). *Appl. Catal. A-Gen.* **2001,** *205*, 1, 51-59.

[180] Tiwari, N.; Kumar, S.; Kamal, C.; Chakrabarti, A.; Prajapat, C. L.; Mishra, P. K.; Mondal, P.; Jha, S. N.; Bhattacharyya, D., Structural Investigations of (Ni,Cu) Co–Doped ZnO Nanocrystals by X-ray Absorption Spectroscopy. *ChemistrySelect* **2018,** *3*, 5644-5651.

[181] Ahmad, A.; Iqbal, N.; Noor, T.; Hassan, A.; Khan, U. A.; Wahab, A.; Raza, M. A.; Ashraf, S., Cu-Doped Zeolite Imidazole Framework (ZIF-8) for Effective Electrocatalytic CO_2 Reduction. *J. CO_2 Util.* **2021,** *48*, 101523.

[182] Xie, Z.; Liang, S.; Cai, X.; Ding, B.; Huang, S.; Hou, Z.; Ma, P. a.; Cheng, Z.; Lin, J., O_2-Cu/ZIF-8@Ce_6/ZIF-8@F127 Composite as a Tumor Microenvironment-Responsive Nanoplatform with Enhanced Photo-/Chemodynamic Antitumor Efficacy. *ACS Appl. Mater. Interfaces* **2019,** *11*, 31671-31680.

[183] Pappas, D. K.; Borfecchia, E.; Dyballa, M.; Pankin, I. A.; Lomachenko, K. A.; Martini, A.; Signorile, M.; Teketel, S.; Arstad, B.; Berlier, G.; Lamberti, C.; Bordiga, S.; Olsbye, U.; Lillerud, K. P.; Svelle, S.; Beato, P., Methane to Methanol: Structure–Activity Relationships for Cu-CHA. *J. Am. Chem. Soc.* **2017,** *139*, 14961-14975.

[184] Wang, Y.; Jin, X.; Yu, H. S.; Truhlar, D. G.; He, X., Revised M06-L Functional for Improved Accuracy on Chemical Reaction Barrier Heights, Noncovalent Interactions, and Solid-State Physics. *Proc. Natl. Acad. Sci. U. S. A.* **2017**, *114*, 8487-8492.

[185] Elwell, C. E.; Gagnon, N. L.; Neisen, B. D.; Dhar, D.; Spaeth, A. D.; Yee, G. M.; Tolman, W. B. Copper–Oxygen Complexes Revisited: Structures, Spectroscopy, and Reactivity. *Chem. Rev.* **2017**, *117*, 2059–2107.

[186] Kulkarni, A. R.; Zhao, Z.; Siahrostami, S.; Nørskov, J. K.; Studt, F., Monocopper Active Site for Partial Methane Oxidation in Cu-Exchanged 8MR Zeolites. *ACS Catal.* **2016,** *6*, 6531-6536

[187] Schejn, A.; Aboulaich, A.; Balan, L.; Falk, V.; Lalevée, J.; Medjahdi, G.; Aranda, L.; Mozet, K.; Schneider, R., Cu^{2+}-doped Zeolitic Imidazolate Frameworks (ZIF-8): Efficient and Stable Catalysts for Cycloadditions and Condensation Reactions. *Catal. Sci. Technol.* **2015,** *5*, 1829-1839.

[188] Frisch, M. J., Trucks, G. W., Schlegel, H. B., Scuseria, G. E., Robb, M. A., Cheeseman, J. R., Scalmani, G., Barone, V., Petersson, G. A., Nakatsuji, H., Li, X., Caricato, M., Marenich, A. V., Bloino, J., Janesko, B. G., Gomperts, R., Mennucci, B., Hratchian, H. P., Ortiz, J. V., Izmaylov, A. F., Sonnenberg, J. L., Williams, Ding, F., Lipparini, F., Egidi, F., Goings, J., Peng, B., Petrone, A., Henderson, T., Ranasinghe, D., Zakrzewski, V. G., Gao, J., Rega, N., Zheng, G., Liang, W., Hada, M., Ehara, M., Toyota, K., Fukuda, R., Hasegawa, J., Ishida, M., Nakajima, T., Honda, Y., Kitao, O., Nakai, H., Vreven, T., Throssell, K., Montgomery Jr., J. A., Peralta, J. E., Ogliaro, F., Bearpark, M. J., Heyd, J. J., Brothers, E. N., Kudin, K. N., Staroverov, V. N., Keith, T. A., Kobayashi, R., Normand, J., Raghavachari, K., Rendell, A. P., Burant, J. C., Iyengar, S. S., Tomasi, J., Cossi, M., Millam, J. M., Klene, M., Adamo, C., Cammi, R., Ochterski, J. W., Martin, R. L., Morokuma, K., Farkas, O., Foresman, J. B. & Fox, D. J. *Gaussian 16, Rev. A.03*. (Gaussian, Inc., 2016)

[189] Weigend, F.; Ahlrichs, R., Balanced Basis Sets of Split Valence, Triple Zeta Valence and Quadruple Zeta Valence Quality for H to Rn: Design and Assessment of Accuracy. *Phys. Chem. Chem. Phys.* **2005**, *7*, 3297-3305.

[190] Weigend, F., Accurate Coulomb-Fitting Basis Sets for H to Rn. *Phys. Chem. Chem. Phys.* **2006**, *8*, 1057-1065.

[191] Wang, Y.; Jin, X.; Yu, H. S.; Truhlar, D. G.; He, X., Revised M06-L Functional for Improved Accuracy on Chemical Reaction Barrier Heights, Noncovalent Interactions, and Solid-State Physics. *Proc. Natl. Acad. Sci. U. S. A.* **2017**, *114*, 8487-8492.

Chapter 3 Nonadiabatic Dynamics of 1,3-Cyclohexadiene by Curvature-Driven Coherent Switching with Decay of Mixing

In part from

Zhang, L.; Shu, Y.; Bhaumik S.; Chen X.; Sun, S.; Huang, Y.; Truhlar, D. G. Nonadiabatic Dynamics of 1, 3-cyclohexadiene by Curvature-Driven Coherent Switching with Decay of Mixing. *J. Chem. Theory Comput.* **2022,** *18,* 7073-7081.

3.1 Introduction

The photoinduced electrocyclic ring-opening of 1,3-cyclohexadiene (13CHD) and its derivatives has been very widely studied both theoretically and experimentally, as amply documented in reviews[192,193] and as seen many recent papers[194,195,196,197,198,199,200,201,202,203,204,205,206,207] employing state-of-the-art methods. The ability to simulate this well understood reaction accurately provides a stiff test of theoretical methods, and the present study applies this test to the recently proposed[208] curvature-driven coherent switching with decay of mixing (κCSDM) method.

Coherent switching with decay of mixing (CSDM) is a nonadiabatic dynamics algorithm[209,210] that combines most of the advantages of trajectory surface hopping (TSH)[211,212,213] and semiclassical Ehrenfest dynamics (SE)[214,215,216,217] with a Liouville-von Neumann treatment[218,219] of electronic decoherence. With non-Markovian decoherence added to coherent equation of motion based on the self-consistent potential of SE, it balances coherence and decoherence, and the decoherence allows it to describe the asymptote behaviors of trajectories after passing through a strong interaction region. CSDM is robust on the choice of electronic state representation (adiabatic or diabatic);[220] and it does not suffer discontinuous nuclear momenta or frustrated hops as occur in TSH. A computational drawback of the original version of CSDM is that it requires an explicit computation of the nonadiabatic coupling vector (NAC) in the nuclear equation of motion. Involving the NAC in the nonadiabatic dynamics algorithms brings in several difficulties including spurious long-range coupling and failure to conserve angular momentum and center of mass motion;[221] and the use of the NAC limits efficient computations to electronic structure methods for which analytical NACs are available. Recently we showed how the NAC may be replaced by an effective NAC calculated from the time derivative of the electronic wave function,[222] and even more recently we developed the κCSDM method, which only requires information about the adiabatic potential energy surfaces and their gradients.[223]

In this work, we will employ κCSDM to investigate the nonadiabatic ring-opening dynamics of the 13CHD molecule. We have three main goals: (1) to demonstrate the high

accuracy and efficiency of the κCSDM algorithm; (2) to optimize the widely discussed conical intersections that mediate the excited-state reaction with dynamic correlation at the level of XMS-CASPT2; (3) to see if the reaction can be well simulated by including only valence states, without including the interleaving Rydberg states, which we have studied[224] previously.

3.2 Computational details

Geometry optimization and frequency calculation for ground-state 13CHD were performed by MN15/may-cc-pVTZ using *Gaussian16*.[225,226,227] We also obtained a ring-opening path as a function of the C1-C2 bond length (C1 and C2 are defined as shown in the left panel of Figure 13) in which selected key geometries are joined by linear synchronous transit[228] (LST) paths.

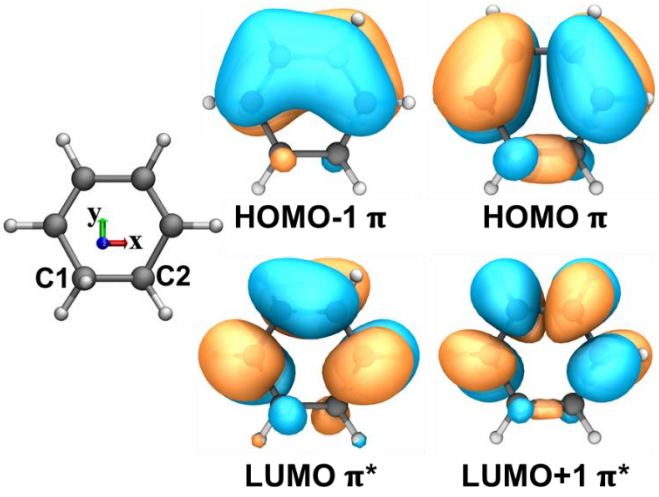

Figure 13. The valence active orbitals.

For the ground-state minimum geometry and geometries of the relaxed-scan path, we investigated the first three singlet states with extended multistate complete-active-space second-order perturbation theory (XMS-CASPT2)[229] using 3-state state-averaged complete active space self-consistent-field calculations (SA(3)-CASSCF) as reference wave functions; these calculations were performed with the BAGEL program.[230] The active space consists of four active electrons in four valence orbitals (4e,4o), see the right panel of Figure 13. The orbital and density fitting basis sets used are def2-TZVP and def2-universal-JKFIT, respectively.[231] A real level shift of 0.3 E_h is used to avoid possible

intruder states in all XMS-CASPT2 calculations.

The geometries for S_0/S_1 and S_1/S_2 minimum energy conical intersections (MECIs) are optimized with CIOpt code.[232] We found two local minima along the S_1/S_2 conical intersection seam, and we will denote these as S_1/S_2 local-minimum-energy conical intersections (LMECIs). We found one minimum on the S_0/S_1 conical intersection seam, and we label it S_0/S_1 MECI.

The electronically nonadiabatic trajectory calculations are performed with the κCSDM method as implemented in the SHARC-MN[233] program. A total of 500 initial coordinates and velocities were sampled from the ground-state Wigner distribution, then vertically excited to the S_1 or S_2 excited state. The trajectories initiated in the S_1 state are denoted as Set1, and the trajectories initiated in the S_2 state are denoted as Set2. The trajectories of Set1 are representative of an experiment initiated with white light. The Set2 trajectories do not correspond to experiment because Set2 has only a small oscillator strength, but the Set2 trajectories are computed to answer the "what if' question of what would happen if one could initially excite the dark state.

The nuclear motions were propagated with a time step of 0.1 fs, with 200 electronic substeps for each nuclear step. Trajectories were terminated after 100 fs.

3.3 Results and discussion

3.3.1 Structure

At the ground-state minimum geometry of 13CHD, XMS-CASPT2 predicts the excitation energies of two valence excited states as 4.95 and 6.38 eV. This agrees well with experimental values[192,234,235,236] of 4.94 and 6.0 eV respectively, and this good agreement validates that we have a reasonable active space and basis set.

The four active orbitals of 13CHD are shown in Figure 13 right panel. The antisymmetric S_1 state is dominated by a HOMO → LUMO single excitation, while the symmetric S_2 has a mixed character involving HOMO→ LUMO double excitation as well as HOMO – 1 → LUMO single excitation. This agrees with previous work[192,196] indicating that the S_1 state is important for providing oscillator strength into the excited-state manifold, and the S_2 state is the state that makes the ring opening orbital-symmetry-allowed. This picture is in complete accord with the classic work of van der Lugt and

Oosterhoff[237,238] who first explained the role of orbital symmetry in photochemical electrocyclic reactions in terms of a mechanism by which "a molecule in the [spectroscopically observed] antisymmetric excited state very rapidly reaches the well in the symmetric excited state before interconversion to the ground state with emission of light has occurred," and it is the symmetric excited state that leads to ring opening.

The hexatriene (HT) structure has configuration interaction (CI) coefficients that are similar to those of 13CHD, but it involves different orbitals in the configuration state functions. The energy levels and CI coefficients for 13CHD and HT are shown in Table 2.

Table 2: Energies (eV), dominant configurations, and CI coefficients of the three valence states considered here are the ground-state minimum-energy geometries of 13CHD and of HT (the occupation numbers of the dominant configurations correspond to orbitals in Figure 13 and Figure S1 of the SI in the same order).

State	Exp.	SA(3)-XMS-CASPT2(4e,4o)/def2-TZVP					
		13CHD			HT		
		Energy	Dominant config.	CI coeff.	Energy	Dominant config.	CI coeff.
S_0	0.00	0.00	22 00	0.955	1.13	22 00	0.955
S_1	4.94	4.95	21 10	0.979	6.09	21 10	0.965
S_2	6.30	6.38	20 20	0.618	7.48	20 20	0.589
			12 10	0.507		12 10	0.519
			21 01	0.397		21 01	0.394
			02 20	0.277		02 20	0.257
			20 02	0.219		20 02	0.219

[a]Geometries are optimized with MN15/may-cc-pVTZ.

Previous discussions of the potential energy surfaces have qualitatively indicated that one might expect two S_1/S_2 conical intersections to be involved,[197,198,201,239] although limited optimizations of these structures have been reported at a level containing external correlation beyond CASSCF. In the present work we did find two S_1/S_2 LMECIs, an inner one and an outer one, and we optimized them. The inner S_1/S_2 LMECI involves a shorter C1-C2 bond than does the outer S_1/S_2 LMECI, and these two geometries correspond to two local minima of the S_1/S_2 seam. We also optimized the S_0/S_1 MECI. These structures are

given in Table 3 along with reactant and product structures and the energies of the three states at each of the optimized structures.

Table 3: The lowest three state energies for ground-state minimum, S_0/S_1 MECI and S_1/S_2 LMECI geometries and C1-C2 bond length.

	CHD[a]	S_1/S_2 inner LMECI[b]	S_0/S_1 MECI[b]	S_1/S_2 outer LMECI[b]	HT[a]
C1–C2 bond (Å)	1.523	2.033/1.986[d]	2.132/2.137[d]	2.344	3.448
C6–C1–H7–H8 (deg)[c]	55.5	26.9	26.4	16.7	0.15
C3–C2–H9–H10 (deg)[c]	55.5	26.6	13.7	15.3	0.15
Energy of S_0 (eV)	0	2.5927	3.5186	2.4870	1.1279
Energy of S_1 (eV)	4.9537	4.0672	3.5186	4.2257	6.0858
Energy of S_2 (eV)	6.3836	4.0672	5.8348	4.2257	7.4779

[a]Geometries of stable structures are optimized with MN15/maug-cc-pVTZ.

[b]MECI and LMECI structures are optimized with XMS-CASPT2(4e,4o)/def2-TZVP based on a SA(3)-CASSCF(4e,4o) reference wave function

[c]The pyramidalization angle A-B-C-D is defined as 90° minus the angle between the A-B bond and the vector normal to the BCD plane.

[d]Values after the solidus were obtained by Mori and Kato[241] using MS-CASPT2(6e,6o)/6-31G*.

We first consider the nonadiabatic ring-opening mechanism from the point of view of the optimized structures. As in previous qualitative pictures, the S_0/S_1 MECI is lower in energy than both S_1/S_2 LMECIs, and it occurs at an intermediate C1-C2 distance.[197,198,201,239] Lining up the stationary points in order of their C1-C2 bond distances gives the ordered list: 13CHD, inner S_1/S_2 LMECI, S_0/S_1 MECI, outer S_1/S_2 LMECI, and HT with C1-C2 bond distances of 1.52, 2.03, 2.13, 2.34, and 3.45 Å respectively.

Mori and Kato[240] have also reported one S_0/S_1 and one (the inner) S_1/S_2 MECI geometry as obtained by MS-CASPT2(6e,6o)/6-31G*. Although caution is advised because MS-CASPT2 is less reliable than XMS-CASPT2 at and near conical intersections and because they used a smaller basis set, the C1-C2 bond distances from their calculations are 1.986 and 2.137 Å for the S_1/S_2 LMECI and S_0/S_1 MECI, respectively, which are quite close with our results.

The three optimized MECIs not only share similar C1-C2 bond lengths, but they also have two less pyramidalized groups (C3C2H2, and C6C2H2) as compared to ground-state minimum geometry of 13CHD. The pyramidalization angles for the conical intersections are in the range 14–28 deg, as compared to 55.5 deg for the reactant. The optimized conical intersections are compared in Figure 14. For the electronic states of the S_0/S_1 MECI and the S_1/S_2 LMECIs, the main configurations and their configuration interaction coefficients are presented in Table 4.

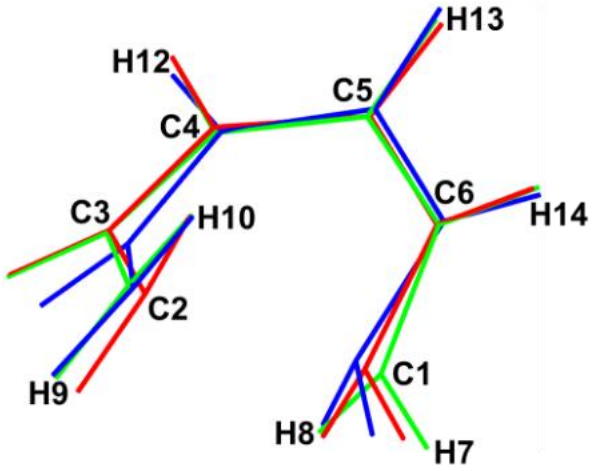

Figure 14: Inner S_1/S_2 (red) , S_0/S_1 (blue) and outer S_1/S_2 (green) MECI geometries at SA(3)-XMS-CASPT2(4e,4o)/def2-TZVP. The energies and C–C bond distances of these conical intersections are given in Table 3.

Table 4: Dominant configurations and corresponding CI coefficients of the S_0/S_1 MECI and two S_1/S_2 LMECI geometries, the occupation numbers of the dominant configurations correspond to orbitals in Figure S1 of the SI in the same order.

State	S_0/S_1 MECI		S_1/S_2 inner LMECI		S_1/S_2 outer LMECI	
	Dominant config.	CI coeff.	Dominant config.	CI coeff.	Dominant config.	CI coeff.
S_0	2110	0.947	2200	0.865	2200	0.905
			2020	0.430	2020	0.326
S_1	2200	0.965	2200	0.421	2200	0.315
			2020	0.839	2020	0.871
S_2	2020	0.946	2110	0.988	2110	0.984

To provide quantitative potential energy profile along the nonadiabatic ring-opening coordinate, we computed paths in which selected points are joined by linear synchronous transit (LST) paths. Six geometries are selected as nodes in the LST paths:

A: a 13CHD structure with a short C1-C2 distance,

B: the 13CHD ground-state minimum-energy geometry,

C: the inner S_1/S_2 LMECI,

D: the S_0/S_1 MECI,

E: the outer S_1/S_2 LMECI, and

F:HT

The Cartesian coordinates of these node geometries are in Supporting Information (SI). Two ring-opening paths are considered. One path (LST1) corresponds to A → B → C → D → E → F; the other (LST2) corresponds to A → B → C → E → F. The two paths are shown in Figure 15 along with the HOMO and LUMO at each node. (All four valence orbitals of 13CHD ground state minimum, inner S_1/S_2 LMECI, S_0/S_1 MECI, outer S_1/S_2 LMECI, and HT geometries are shown in Figure S1 of the SI.) Figure 15 shows how the S_2 state of the reactant transforms diabatically to S_0 and the products and how the conical intersections mediate the necessary transitions from one adiabatic state to another. Clearly the inner S_1/S_2 LMECI is more important than the outer one.

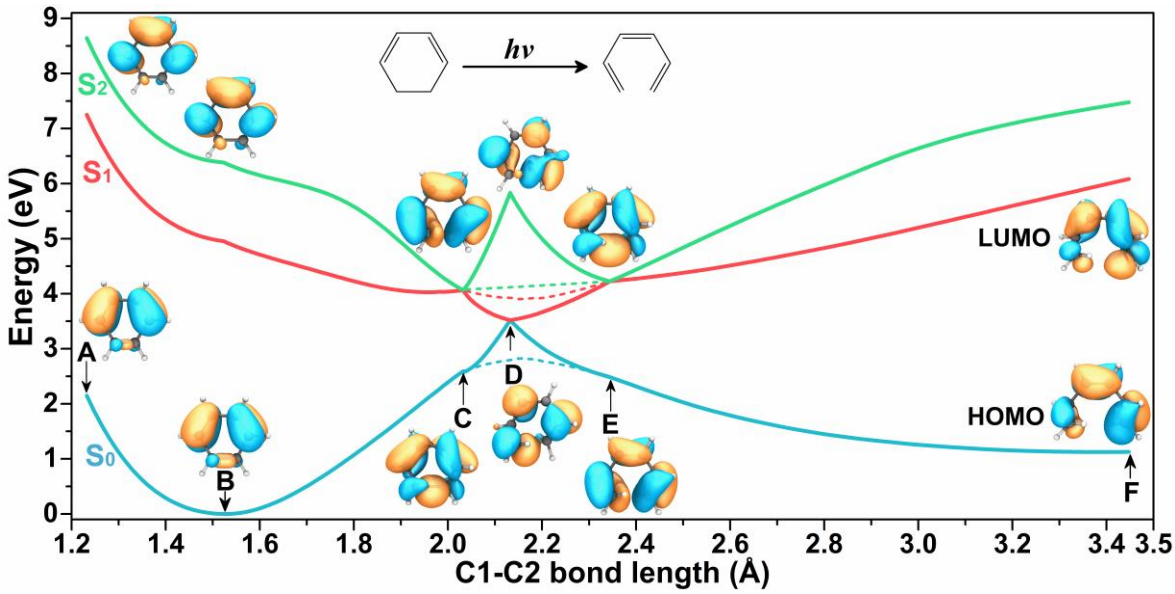

Figure 15: The XMS-CASPT2 energies along the piecewise linear-synchronous-transit ring-opening paths. Also shown, far each node, are the HOMO and LUMO orbitals from the SA(3)-CASSCF reference functions. Five geometries are considered, as specified in Section III. The LST1 path is shown as solid curves, and the LST2 path is shown as dotted curves. In the A-to-C and E-to-F regions, the two paths coincide. III. The LST1 path is shown as solid curves, and the LST2 path is shown as dotted curves. In the A-to-C and E-to-F regions, the two paths coincide.

The active space of 4 active electrons in four active orbitals is a minimal one for this problem. Parts 2 and 3 of the Supporting Information show that the HOMO and LUMO change smoothly along the C-C bond breaking path, but – as is already known from the orbital correlation diagram[241] – as the reaction proceeds, the HOMO–1 switches with the HOMO-2 and the LUMO+1 switches with the LUMO+2, so one might question whether an active space with 6 active electrons in six active orbitals would give qualitatively different results. Figure 16 compares the energy curves along the LST paths by (6e,6o) and (4e,4o) active spaces as calculated by XMS-CASPT2/def2-TZVP. They agree quite well, and we conclude that the (4e,4o) active space is sufficient for the present study of the performance of tCDDM for a realistic system. In fact, since orbital switching along a photodissociation pathway is often hard to avoid, this test, where some orbital switching occurs, is very relevant to practical applications.

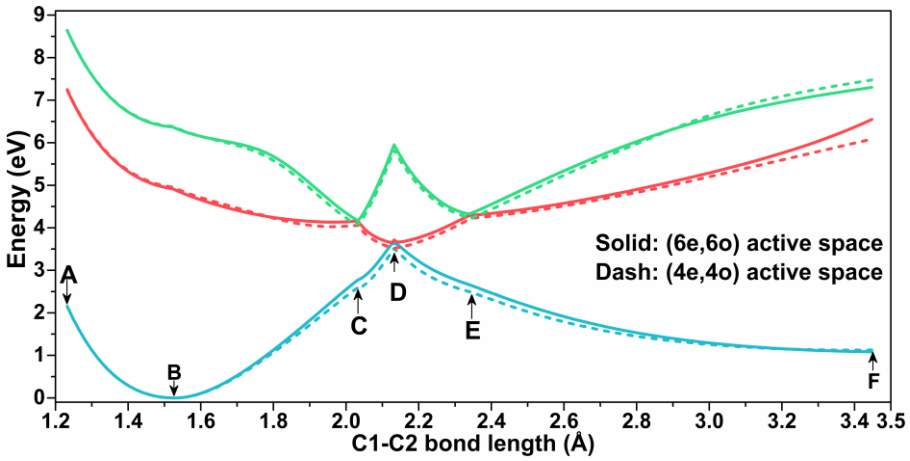

Figure 16: Comparison of the energy curves along the LST paths by (6e,6o) and (4e,4o) active spaces at XMS-CASPT2/def2-TZVP level.

3.3.2 Dynamics

Next, we discuss the trajectories. The same initial conditions (geometry and momentum), as obtained from the ground-state Wigner distribution, are used for both S_1 and S_2 dynamics; the difference between the two sets is the initial potential and this is realized by manually setting the initial state in the vertical excitation process. Therefore, the initial kinetic energy distribution for Set1 and Set2 are identical, but the total energy is different because of the difference in initial potential energy. The distributions of initial kinetic and total energies are shown in the left panel of Figure 17. The potential energy distributions for S_0, S_1, and S_2, which are denoted as V_0, V_1, and V_2 respectively, are shown in the right panel. The corresponding means of the kinetic, potential, and total energies with root-mean-square deviations (RMSD) from the means are shown in Table 5. The mean total energies for Set1 and Set2 are 8.17 and 9.57 eV with RMSDs of 0.78 and 0.86 eV. These data show the initial energy distributions for the two sets of trajectories. This provides quantitative information about the Wigner sampling, and the kinetic energy distributions in the excited states provide the initial conditions of the multistate trajectories. Figure 17 shows the range of energies involved in the simulation and hence the range of energies over which the potential energy surfaces affect the results.

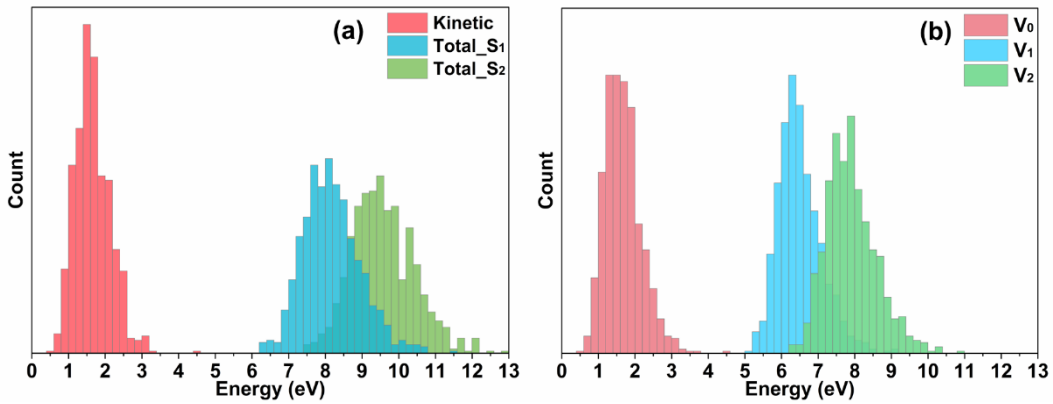

Figure 17: (a) Kinetic distributions of the ground-state Wigner distribution and total energy distributions after vertical excitation to S_1 or S_2. (b) Same except total energy is replaced by potential energy with respect to the energy of the ground-state minimum geometry. See Table 5 for mean values.

Table 5: Mean kinetic, potential, and total energies and root-mean-square deviation (RMSD) from its mean value (in eV)

Energy	Mean	RMSD
kinetic[a]	1.66	0.48
V_0[b]	1.68	0.49
V_1[b]	6.51	0.60
V_2[a]	7.91	0.69
Total[a,c]	8.17	0.78
Total[a,c]	9.57	0.86

[a] See Figure 17 for distribution.
[b] Potential energies are with respect to the energy of the ground-state minimum.
[c] Total energy when vertically excite to S_1. See Figure 17 for distribution.
[d] Total energy when vertically excite to S_2.

After simulation of 100 fs of dynamical motion, the populations of S_0, S_1, and S_2 are respectively 0.56, 0.36, and 0.08 for Set1 and 0.53, 0.39, and 0.08 for Set2. The population for both sets as functions of time is shown in Figure 18. For Set1, in which the trajectories start on S_1, the population of S_2 first increases until about 33 fs and then decays. This indicates that the trajectories go through S_1/S_2 locally avoided crossings, and it is consistent with the potential energy surfaces shown in Figure 15. By fitting the Set1 results to a single exponential function, as shown in Figure 18, the lifetime of S_1 is 96 fs, and the lifetime of S_1+S_2 is 79 fs. For Set2, the decay of S_2 population involves two time scales, with a fast

decay in the first 10–20 fs, followed by a slower decay. By fitting to a double exponential, the lifetimes of the fast and slow decays are 9 and 31 fs. For Set2, the lifetime of S_1+S_2 is 92 fs. The lifetimes are very comparable to experimentally measured internal conversion time constants around 60 – 80 fs.[197,242]

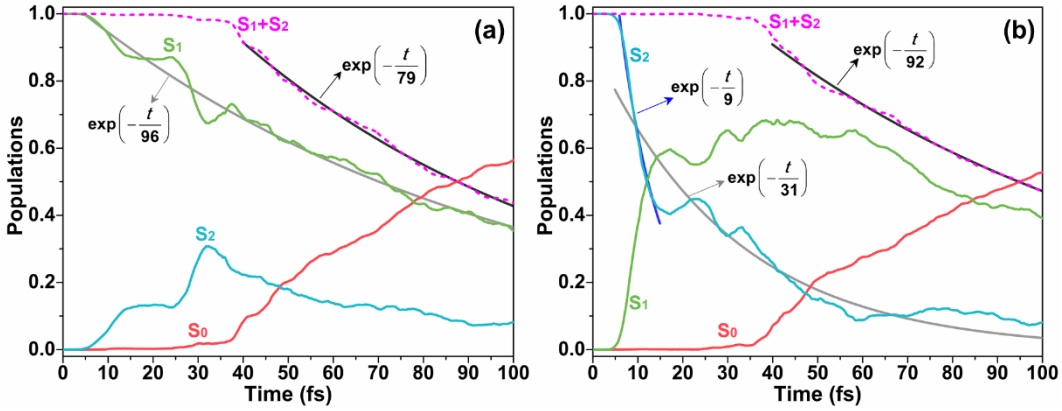

Figure 18: Ensemble averaged time evolution of the electronic state population for S_0 (red), S_1 (green), S_2 (blue) and S_1+S_2 (purple) averaged over 500 trajectories for Set1 and Set2. For Set1 (shown in panel a) the fitted lifetime of S_1 is 96 fs, and S_1+S_2 is 79 fs. For Set2 (shown in panel b) the decay of S_2 involves two processes with lifetimes of 9 and 31 fs; the fitted lifetime of S_1+S_2 is 92 fs.

The geometries where pointer-state switching occurs are expected to often be close to the locally avoided crossings. We computed the distribution of C1-C2 bond lengths at pointer-state switching geometries for Set2, and the results are shown in Figure 19. One can observe two peaks for S2-S1 pointer state switching geometries, one locates near 1.6 – 1.7 Å and the other (a much smaller peak) is about 1.9 – 2.0 Å. This may be explained by the different regions of pointer state switching geometries corresponding to different (i.e., inner and outer) S_1/S_2 LMECIs. (The distribution of C1-C2 bond length at 100 fs can be found in Figure S3, and the time evolution of C1-C2 bond length is given in Figure S4, where figures with a prefix S are in the SI.)

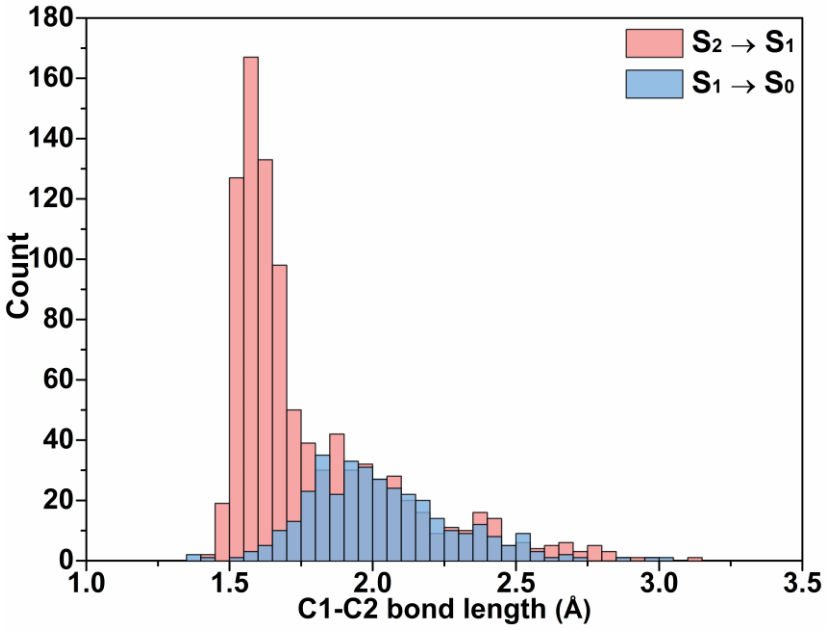

Figure 19: C1-C2 bond length distribution at pointer state switching geometries for Set2.

The time evolution of the ensemble-averaged S_0, S_1, S_2 and mean-field PESs is shown in Figure 20. For Set 1 the participation of S2 in the net $S_1 \rightarrow S_0$ transition is hard to see in the ensemble-averaged potentials. The Set2 trajectories show significant population in S_2 out to at least 40 fs. These ensemble-averaged potentials are both consistent with the observed fast population decay to S_0.

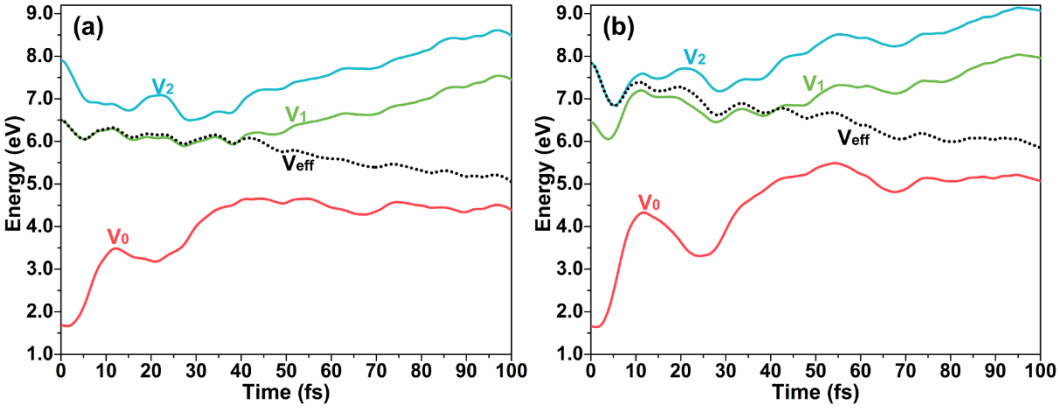

Figure 20: Time evaluation of the ensemble averaged S_0, S_1, S_2 and mean-field PESs denoted as V_0 (red), V_1 (green), V_2 (blue), and V_{eff} (dotted black) for dynamics of (a) Set1 and (b) Set2.

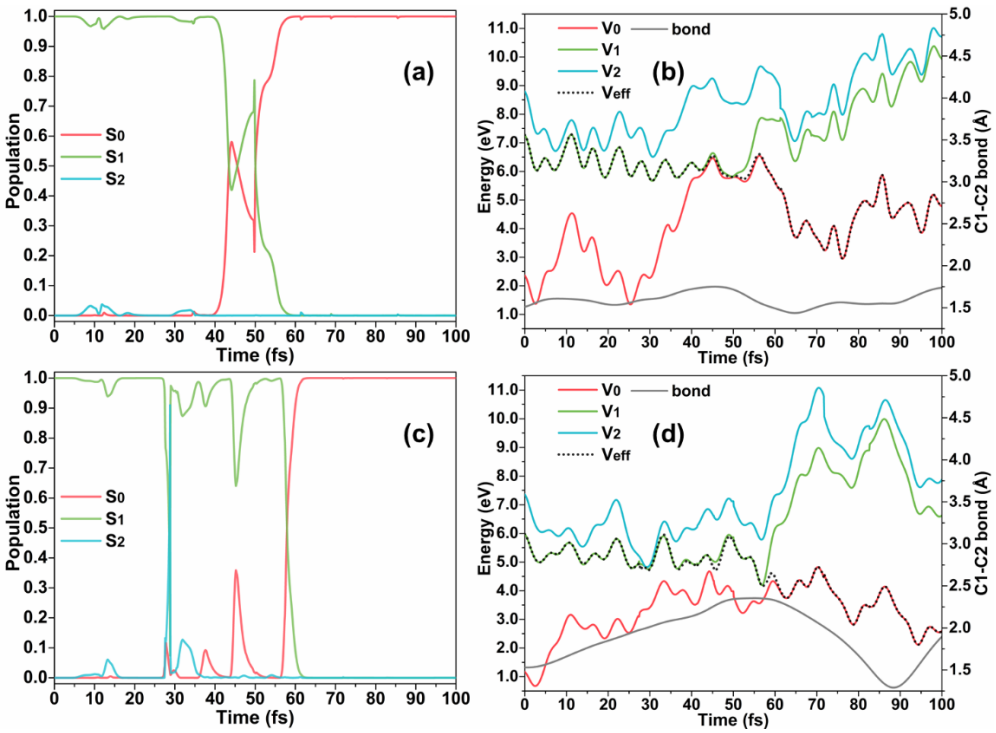

Figure 21: Time evolution of state density population, adiabatic and mean-field potentials, and C1-C2 bond length for two representative non-ring-opening trajectories.

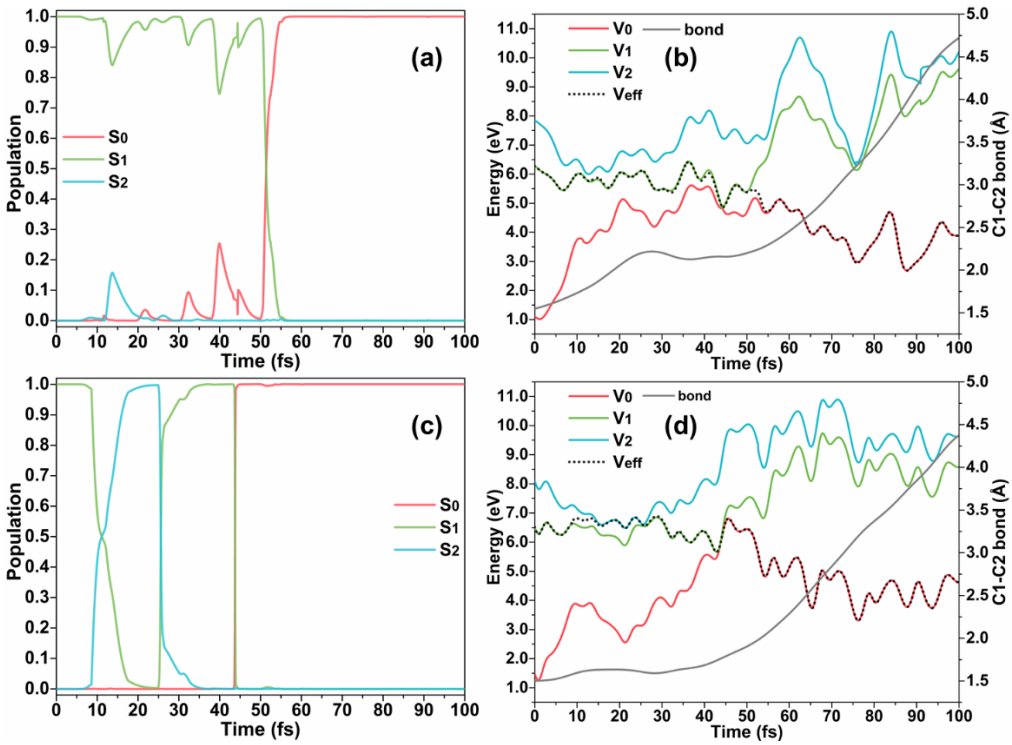

Figure 22: Time evolution of state density population, adiabatic and mean-field potentials, and C1-C2 bond length for two representative ring-opening trajectories.

Four typical trajectories are illustrated in Figures 21 and 22. Figure 21 shows two non-ring-opening trajectories, and Figure 22 shows two ring-opening trajectories. Analysis of these and other trajectories shows that the temporary population of S_2 is more prominent in the ring-opening trajectories. The state populations in Figures 21 and 22 are typical for CSDM trajectories. The rapid changing of the state populations is a result of properly treating the decoherence with the decay-of-mixing scheme in our CSDM nonadiabatic dynamics method,[209] in which, for each trajectory after traversing a strong interaction region, the diagonal density matrix element of the pointer state is driven to unity and all other density matrix elements tend to zero because of the decoherence. In previous papers on the decay-of-mixing methodology, we explain how this algorithmic demixing simulates electronic decoherence.[243,244,245,246,247,248] On the time scale shown, the decoherence can occur rapidly for this problem because the spatial separation of the nuclear wave packets after traversing a strong interaction region can be very fast.

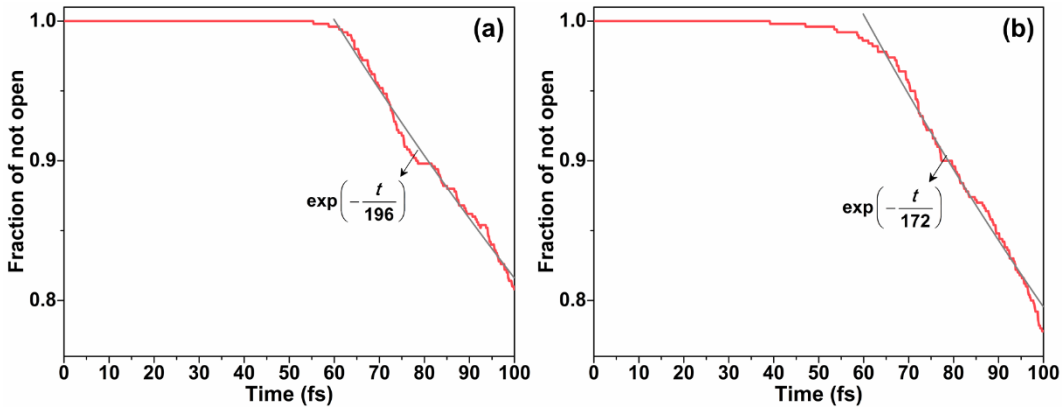

Figure 23: Population of ring-closed geometry as a function of time for (a) Set1 and (b) Set2. The fitted range is 60 fs to 100 fs. Ring opening is considered to have occurred when any C1–C2 distance exceeds 3 Å.

To access the rate of ring-opening nonadiabatic reaction, we monitored the population of ring-closed geometries along the trajectory. The criterion is set as 3 Å, i.e., a geometry with C1-C2 bond less than 3 Å is considered as ring-closed geometry. The population as a function of time is shown in Figure 23. The fitted lifetime after the induction period is 196 fs for Set1 and 172 fs for Set2. Therefore, we can predict the product ratio of HT for the experimentally relevant Set1 conditions:

$$\frac{[\mathrm{HT}]}{[\mathrm{HT}]+[\text{1,3-CHD}]} = \frac{k_{\mathrm{HT}}}{k_{\text{internal conversion}}} = \frac{\tau_{S_1+S_2}}{\tau_{\mathrm{HT}}} = \frac{79}{196} = 0.40 \quad (1)$$

where k_{HT} and $k_{\text{internal conversion}}$ are rate constants for ring opening and internal conversion, respectively, and τ_{HT} and $\tau_{\text{internal converson}}$ are lifetimes of excited states ad ring-opening reaction. This shows that the simulation of 13CHD nonadiabatic ring-opening dynamics with the κCSDM method is realistic because it is close to a previously reported 30% of ring-opening quantum yield in ref.196, but a comparison to all experimental evidence is beyond our scope. Comprehensive comparison to previous work would entail a review article because this reaction has been widely studied with a variety of experimental, electron structure, and dynamical methods. However, in the next paragraph we focus on a particularly relevant comparison to a previous theoretical study.

Concerning theoretical work, we note that Polyak et al.[204] wrote in 2019 that "All of the previous dynamic studies are prone to deficiencies of different types, either connected to the description of the nonadiabatic interaction or of the electronic density. In particular, none of the ab initio studies treated all aspects of electronic structure calculations in a balanced way with a consistent level of dynamic correlation, with some relying on CASSCF gradients and others on CASSCF NACs. Recent derivation of the analytic gradients and NAC for XMS-CASPT2 and their implementation in the BAGEL electronic-structure program finally made such calculations possible." Polyak et al. [204] then presented a very consistent study based on XMS-CASPT2 energies and NACs. Although they used a smaller basis set (cc-pVDZ) than we used here and a different dynamical method, comparison to their work is particularly interesting since we also included dynamical correlation by XMS-CASPT2 and since the main objective of the present work is to test whether we can get realistic results on a real system with our new curvature-driven method that does not require NACs or time derivatives (it uses only the adiabatic potentials and their time derivatives, which is very convenient). One difference between the present work and the simulations of Polyak et al. is that the present work involves a broader range of initial excitation energies; however, Figure S2 shows that the S_0 and S_1 decay times are not strong functions of energy in the range of our simulation; therefore, the comparison is meaningful. Without NACs, time derivatives, or diabatization, we get a decay constant of 79 fs for the excited-state decay and a quantum yield of 40%. Using NACs, Polyak et al. got 73 fs and 47% (almost the same). This shows that reasonable nonadiabatic dynamics can be calculated using only the adiabatic energies.

3.4 Conclusions

In this work, we have employed κCSDM to study the nonadiabatic ring-opening dynamics of the 13CHD molecule. The potential energies are displayed for linear-synchronous-transit ring-opening paths connecting critical geometries, which include the ground-state minimum structure of 13CHD, the S_1/S_2 local-minimum-energy conical intersections, the S_1/S_0 minimum energy conical intersection, and the product HT, and

these plots show the ring-opening mechanism involves both S_1/S_2 and S_1/S_0 conical intersections. The participation of both S_0 and S_1 are then observed in κCSDM electronically nonadiabatic dynamics. The predicted lifetime of internal conversion is 79 fs, which is consistent with experimentally observed values in the range 60–80 fs. With the fitted ring-opening lifetime of 196 fs, we have predicted the ring-opening quantum yield to be 40%, which is comparable to what has been measured in experiments.

The current simulation demonstrates that the κCSDM algorithm, a semiclassical nonadiabatic dynamics algorithm requiring only adiabatic potential energies and their gradients, can accurately describe the nonadiabatic processes in this prototypical photochemical electrocyclic reaction. Furthermore, we obtain a reasonable description of the reaction without including the low-lying Rydberg states. Our optimization of the local-minimum-energy and minimum-energy conical intersections and our mapping of the adiabatic potential energies along the paths connecting with XMS-CASPT2 dynamical correlation provides a quantitative confirmation of the classic interpretation of photochemical electrocyclizations reactions first advanced by van der Lugt and Oosterhoff.[236,237]

3.5 Supporting Information

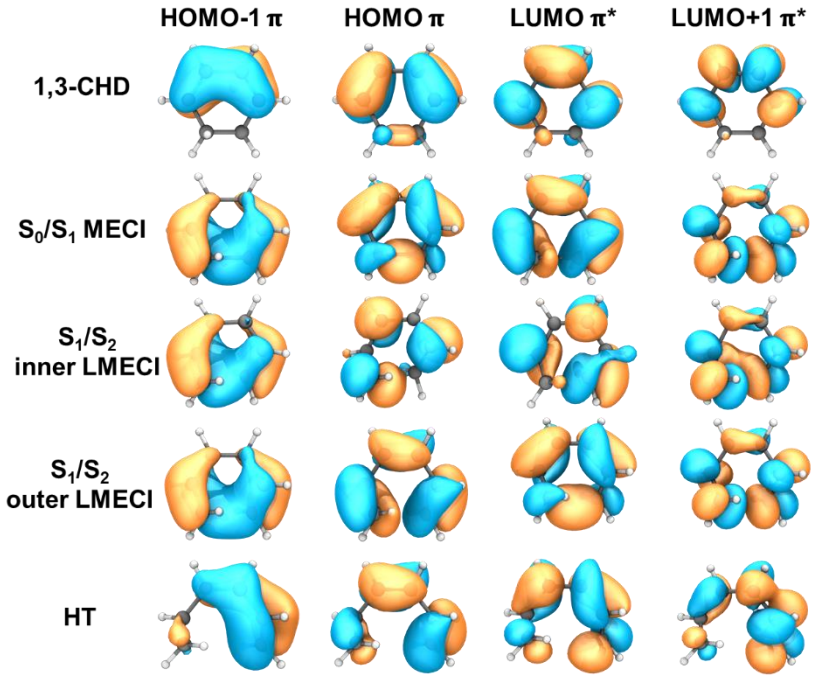

Figure S1 The active orbitals for key geometries along the ring-opening path.

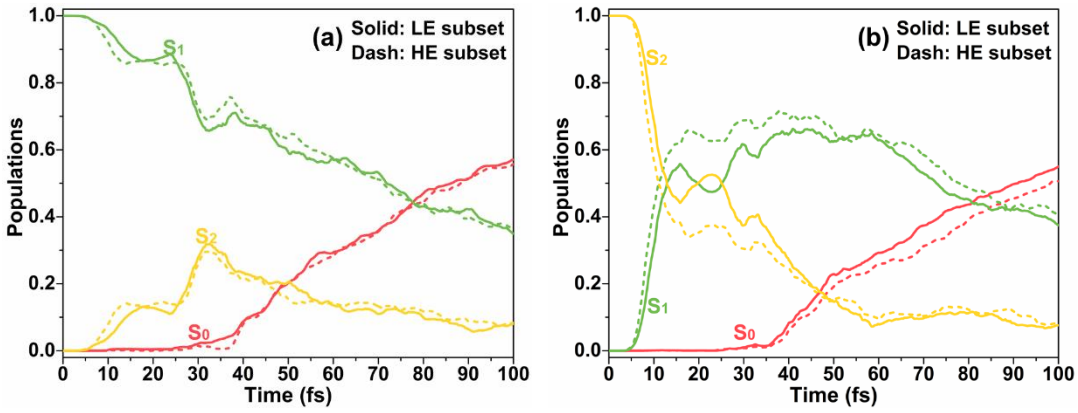

Figure S2. About half of the trajectories have total energy greater than the mean, and half have a total energy below the mean. Here we look at these two subsets separately, the high-energy (HE) and low-energy (LE) subsets. (a) Excitation to S_0. (b) Excitation to S_1. The two subsets (HE and LE subset) show similar behavior with respect to state populations.

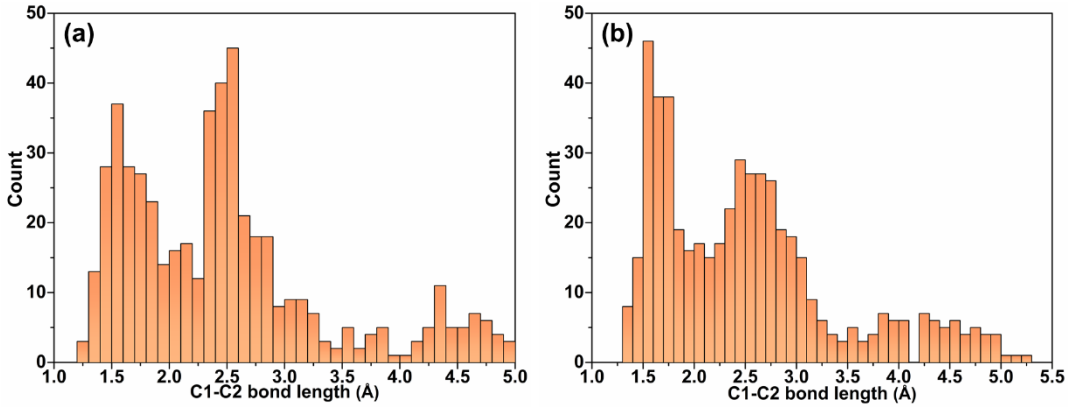

Figure S3. C1-C2 bond length distribution when integrated for 100 fs for (a) Set1 and (b) Set2.

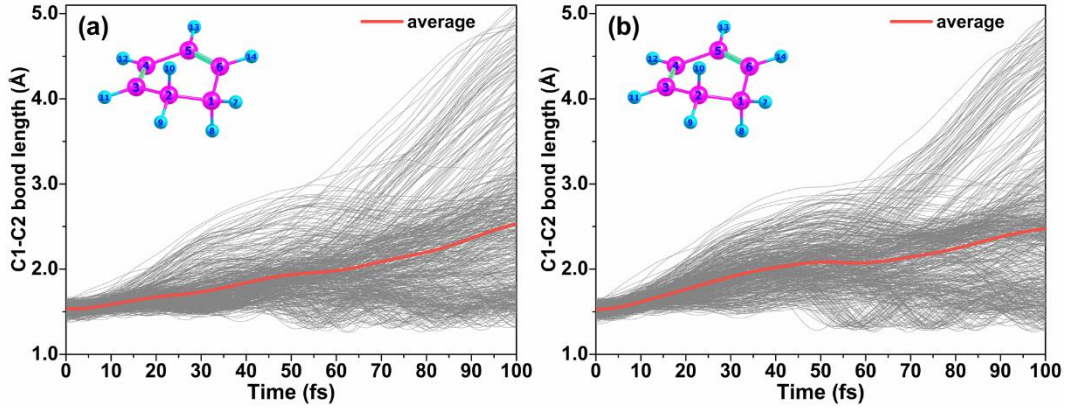

Figure S4. Evolution with time of C1-C2 bond length for all the trajectories of (a) Set1 and (b) Set2.

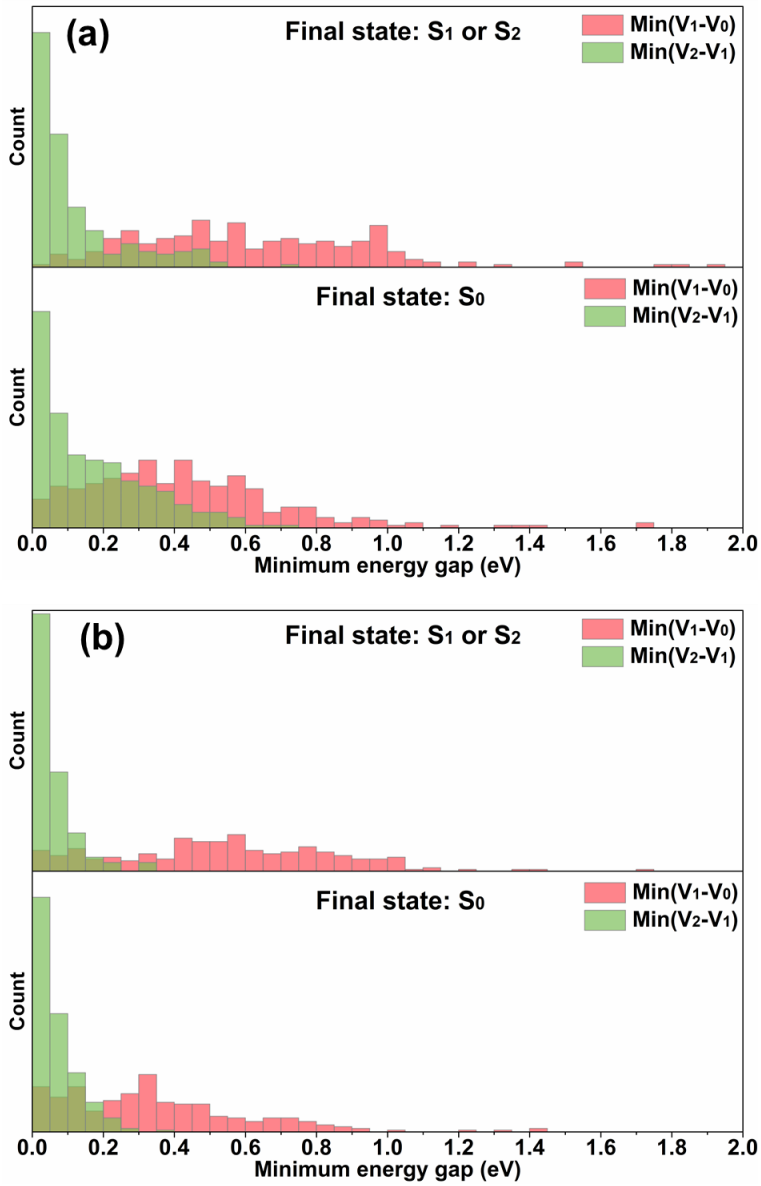

Figure S5. Distribution of the minimum of the (V_1–V_0) and (V_2–V_1) adiabatic gaps for the trajectories of (a) Set1 and (b) Set2.

Bibliography

[192] Deb, S.; Weber, P. M. The Ultrafast pathway of photon-induced electrocyclic ring-opening reactions: The case of 1,3-cyclohexadiene. *Annu. Rev. Phys. Chem.* **2011**, *62*, 19–39.

[193] Arruda, B. C.; Sension, R. J. Ultrafast polyene dynamics: the ring opening of 1,3-cyclohexadiene derivatives. *Phys. Chem. Chem. Phys.* **2014**, *16*, 4439-4455.

[194] Ohta, A.; Kobayashi, O.; Danielache, S. O.; Nanbu, S. Nonadiabatic ab initio molecular dynamics of photoisomerization reaction between 1,3-cyclohexadiene and 1,3,5-*cis*-hexatriene. *Chem. Phys.* **2015**, *459*, 45-53.

[195] Minitti, M. P.; et al. Imaging molecular motion: femtosecond X-ray scattering of thering opening in 1,3-cyclohexadiene. *Phys. Rev. Lett.* **2015**, *114*, 255501.

[196] Pemberton, C. C.; Zhang, Y.; Saita, K.; Kirrander, A.; Weber, P. M. From the (^{1}B) spectroscopic state to the photochemical product of the ultrafast ring-opening of 1,3-cyclohexadiene: A spectral observation of the complete reaction path. *J. Phys. Chem. A* **2015**, *119*, 8832-8845.

[197] Adachi S, Sato M, Suzuki T. Direct observation of ground-state productformation in a 1,3-cyclohexadiene ring-opening reaction. *J. Phys. Chem. Lett.* **2015**, *6*, 343–346.

[198] Lei, Y.; Wu, H.; Zheng, X.; Zhai, G.; Zhu, C. Photo-induced 1,3-cyclohexadiene ring opening reaction: Ab initio on-the-fly nonadiabatic molecular dynamics simulation. *J. Photochem. Photobiol. A Chem.* **2016**, *317*, 39–49.

[199] Schalk, O. *et al*. Cyclohexadiene revisited: A time-resolved photoelectron spectroscopy and ab initio study. *J. Phys. Chem. A* **2016**, *120*, 2320–2329.

[200] Attar A. R.; Bhattacherjee A.; Pemmaraju C. D.; Schnorr K.; Closser K. D.; Prendergast D.; Leone S. R. Femtosecond X-ray spectroscopy of an electrocyclic ring-opening reaction. *Science* **2017**, *356*, 54–58.

[201] Tudorovskaya, M.; Minns, R. S.; Kirrander, A. Effects of probe energy and competing pathways on time-resolved photoelectron spectroscopy: The ring-opening of 1,3-cyclohexadiene. *Phys. Chem. Chem. Phys.* **2018**, *20*, 17714-17726.

[202] Filatov, M.; Min, S. K.; Kim, K. S. Non-adiabatic dynamics of ring opening in cyclohexa-1,3-diene described by an ensemble density-functional theory method. *Mol. Phys.* **2019**, *117*, 1128-1141.

[203] Wolf, T. J. A.; et al. **2019** The photochemical ring-opening of 1,3-cyclohexadiene imaged by ultrafast electron diffraction. *Nat. Chem.* ***2019***, *11*, 504–509.

[204] Polyak I, Hutton L, Crespo-Otero R, Barbatti M, Knowles PJ. Ultrafast photoinduceddynamics of 1,3-cyclohexadiene using XMS-CASPT2 surface hopping. *J. Chem. Theory Comput.* **2019**, *15*, 3929–3940.

[205] Ruddock, J. M. et al. A deep UV trigger for ground-state ring-opening dynamics of 1,3-cyclohexadiene. *Sci. Adv.* **2019**, *5*, eaax6625.

[206] Karashima, S.; Humeniuk, A.; Uenishi, R.; Horio, T.; Kanno, M.; Ohta, T.; Nishitani, J.; Mitrić, R.; Suzuki, T. Ultrafast ring-opening reaction of 1,3-cyclohexadiene: Identification of nonadiabatic pathway via doubly excited state. *J. Am. Chem. Soc.* **2021**, *143*, 8034-8045.

[207] Guerra, C.; Ayarde-Henríquez, L.; Duque-Noreña, M.; Chamorro, E. On electron pair rearrangements in photochemical reactions: 1,3-cyclohexadiene ring opening. *J. Phys. Chem. A* **2022**, *126*, 395-405.

[208] Shu, Y.; Zhang, L.; Chen, X.; Sun, S.; Huang, Y.; Truhlar, D. G. Nonadiabatic dynamics algorithms with only potential energies and gradients: Curvature-driven coherent switching with decay of mixing and curvature-driven trajectory surface hopping. *J. Chem. Theory Comput.* **2022**, *18*, 1320-1328.

[209] Zhu, C.; Nangia, S.; Jasper, A. W.; Truhlar, D. G. Coherent switching with decay of mixing: An improved treatment of electronic coherence for non-Born-Oppenheimer trajectories. *J. Chem. Phys.* **2004**, *121*, 7658.

[210] Shu, Y.; Zhang, L.; Mai, S.; Sun, S.; González, L.; Truhlar, D. G. Implementation of coherent switching with decay of mixing into the SHARC program. *J. Chem. Theory Comput.* **2020**, *16*, 3464-3475.

[211] Tully, J. C.; Preston, R. K. Trajectory surface hopping approach to nonadiabatic molecular collisions: The reaction of H^+ with D_2. *J. Chem. Phys.* **1971**, *55*, 562-572.

[212] Truhlar, D. G.; Duff, J. W.; Blais, N. C.; Tully, J. C.; Garrett, B. C. The quenching of Na(3 ^{2}P) by H_2: Interactions and dynamics. *J. Chem. Phys.* **1982**, *77*, 764−776.

[213] Tully, J. C. Molecular dynamics with electronic transitions. *J. Chem. Phys.* **1990**, *93*, 1061−1071.

[214] McLachlan, A. D. A Variational solution of the time-dependent Schrödinger equation. *Mol. Phys.* **1964**, *8*, 39-44.

[215] McLachlan, A. D.; Ball, M. A. Time-dependent Hartree-Fock theory for molecules. *Rev. Mod. Phys.* **1964**, *36*, 844-855.

[216] Meyer, H.-D.; Miller, W. H. A classical analog for electronic degrees of freedom in nonadiabatic collision processes. *J. Chem. Phys.* ***1979***, *70*, 3214−3223.

[217] Topaler, M. S.; Allison, T. C.; Schwenke, D. W.; Truhlar, D. G. What is the best semiclassical method for photochemical dynamics of systems with conical intersections? *J. Chem. Phys.* ***1998***, *109*, 3321−3345.

[218] Zhu, C.; Nangia, S.; Jasper, A. W.; Truhlar, D. G. Coherent switching with decay of mixing: An improved treatment of electronic coherence for non-Born-Oppenheimer trajectories. *J. Chem. Phys.* **2004**, *121*, 7658.

[219] May, V.; Kühn, O. *Charge and Energy Transfer Dynamics in Molecular Systems*; Wiley-VCH: Berlin, 2000.

[220] Jasper, A. W.; Nangia, S.; Zhu, C.; Truhlar, D. G. Non-Born-Oppenheimer molecular dynamics. *Acc. Chem. Res.* **2006**, *39*, 101−108.

[221] Shu, Y.; L. Zhang; Varga, Z.; Kelsey, P. A.; Kanchanakungwankul, S.; Sun, S.; Truhlar, D. G. Conservation of angular momentum in direct nonadiabatic dynamics. *J. Phys. Chem. Lett.* **2020,** *11*, 1135-1140.

[222] Shu, Y.; Zhang, L.; Sun, S.; Truhlar, D. G. Time-derivative couplings for self-consistent electronically nonadiabatic dynamics. *J. Chem. Theory Comput.* **2020**, *16*, 4098-4106.

[223] Shu, Y.; Zhang, L.; Chen, X.; Sun, S.; Huang, Y.; Truhlar, D. G. Nonadiabatic dynamics algorithms with only potential energies and gradients: Curvature-driven coherent switching with decay of mixing and curvature-driven trajectory surface hopping. *J. Chem. Theory Comput.* **2022**, *18*, 1320-1328.

[224] Ning, J.; Truhlar, D. G. The valence and Rydberg states of dienes. *Phys. Chem. Chem. Phys.* **2020**, *22*, 6176-6183.

[225] Yu, H. S.; He, X.; Li, S. L.; Truhlar, D. G. MN15: A Kohn-Sham global-hybrid exchange-correlation density functional with broad accuracy for multi-reference and single-reference systems and noncovalent interactions. *Chem. Sci.* **2016**, *7*, 5032-5051.

[226] Papajak, E.; Zheng, J.; Xu, X.; Leverentz, H. R.; Truhlar, D. G. Perspectives on basis sets beautiful: Seasonal plantings of diffuse basis functions. *J. Chem. Theory Comput.* **2011**, *7*, 3027-3034.

[227] Frisch, M. J.; Trucks, G. W.; Schlegel, H. B.; Scuseria, G. E.; Robb, M. A.; Cheeseman, J. R.; Scalmani, G.; Barone, V.; Petersson, G. A.; Nakatsuji, H.; Li, X.; Caricato, M.; Marenich, A. V.; Bloino, J.; Janesko, B. G.; Gomperts, R.; Mennucci, B.; Hratchian, H. P.; Ortiz, J. V.; Izmaylov, A. F.; Sonnenberg, J. L.; Williams-Young, D.; Ding, F.; Lipparini, F.; Egidi, F.; Goings, J.; Peng, B.; Petrone, A.; Henderson, T.; Ranasinghe, D.; Zakrzewski, V. G.; Gao, J.; Rega, N.; Zheng, G.; Liang, W.; Hada, M.; Ehara, M.; Toyota, K.; Fukuda, R.; Hasegawa, J.; Ishida, M.; Nakajima, T.; Honda, Y.; Kitao, O.; Nakai, H.; Vreven, T.; Throssell, K.; Montgomery, J. A.; Jr.; Peralta, J. E.; Ogliaro, F.; Bearpark, M. J.; Heyd, J. J.; Brothers, E. N.; Kudin, K. N.; Staroverov, V. N.; Keith, T. A.; Kobayashi, R.; Normand, J.; Raghavachari, K.; Rendell, A. P.; Burant, J. C.; Iyengar, S. S.; Tomasi, J.; Cossi, M.; Millam, J. M.; Klene, M.; Adamo, C.; Cammi, R.; Ochterski, J. W.; Martin, R. L.; Morokuma, K.; Farkas, O.; Foresman, J. B.; Fox, D. J. *Gaussian 16,* Revision C.01; Gaussian, Inc.: Wallingford CT, 2016.

[228] Halgren, T. A.; Lipscomb, W. N. The synchronous-transit method for determining reaction pathways and locating molecular transition states. Chem. Phys. Lett. **1977**, *49*, 225−232.

[229] Shiozaki, T.; Györffy, W.; Celani, P.; Werner, H.-J. Communication: Extended multi-state complete active space second-order perturbation theory: energy and nuclear gradients. *J. Chem. Phys.* **2011**, *135*, 081106.

[230] Shiozaki, T.; Park, J. W. Analytical derivative coupling for multistate CASPT2 theory. *J. Chem. Theory Comput.* **2017**, *13*, 2561-2570.

[231] Ahlrichs, R.; Weigend, F. Balanced basis sets of split valence, triple zeta valence and quadruple zeta valence quality for h to rn: design and assessment of accuracy. *Phys. Chem. Chem. Phys.* **2005**, *7*, 3297-3305.

[232] Levine, B. G.; Coe, J. D.; Martínez, T. J. Optimizing conical intersections without derivative coupling vectors: Application to multistate multireference second-order perturbation theory (MS-CASPT2). *J. Phys. Chem. B* **2008**, *112*, 405-413.

[233] Shu, Y.; Zhang, L.; Truhlar, D. G. *SHARC-MN*–v1.2; University of Minnesota, Minneapolis, 2022; https://comp.chem.umn.edu/sharc-mn

[234] Ning, J.; Truhlar, D. G. The valence and Rydberg states of dienes. *Phys. Chem. Chem. Phys.* **2020**, *22*, 6176-6183.
[235] McDiarmid, R.; Sabljić, A.; Doering, J. P. Valence transitions in 1,3-cyclopentadiene, 1,3-cyclohexadiene, and 1,3-cycloheptadiene. *J. Chem. Phys.* **1985**, *83*, 2147−2152.
[236] Merchán, M.; Serrano-Andrés, L.; Slater, L. S.; Roos, B. O.; McDiarmid, R.; Xing, X. Electronic spectra of 1,4-cyclohexadiene and 1,3-cyclohexadiene: A combined experimental and theoretical investigation. *J. Phys. Chem. A* **1999**, *103*, 5468−5476.
[237] Van der Lugt, W. T. A. M.; Oosterhoff, L. J. Quantum-chemical interpretation of photo-induced electrocyclic reactions. *Chem. Commun.* **1968**, 1235-1236.
[238] Van der Lugt, W. T. A. M.; Oosterhoff, L. J. Symmetry control and photoinduced reactions. *J. Am. Chem. Soc.* **1969**, *91***,** 6042–6049.
[239] Fuss, W.; Schmid, W. E.; Trushin, S. A. Time-resolved dissociative intense-laser field ionization for probing dynamics: Femtosecond photochemical ring opening of 1,3-cyclohexadiene. *J. Chem. Phys.* **2000**, *112*, 8347-8362.
[240] Mori, T.; Kato, S. Dynamic electron correlation effect on conical intersections in photochemical ring-opening reaction of cyclohexadiene: MS-CASPT2 study. *Chem. Phys. Lett.* **2009**, *476*, 97-100.
[241] Salazar, E.; Faraji, S. Theoretical Study of Cyclohexadiene/Hexatriene Photochemical Interconversion Using Spin-Flip Time-Dependent Density Functional Theory. *Mol. Phys.* **2020**, *118*, e1764120.
[242] Garavelli, M.; Page, C. .S; Celani, P; Olivucci, M.; Schmid, W. E.; Trushin, S. A.; Fuss, W. Reaction path of a sub-200 fs photochemical electrocyclic reaction. *J. Phys. Chem. A* **2001**, *105*, 4458-4469.
[243] Zhu, C.; Jasper, A. W.; Truhlar, D. G. Non-Born-Oppenheimer Trajectories with Self-Consistent Decay of Mixing. *J. Chem. Phys.* **2004**, *120*, 5543-5557.
[244] Jasper, A. W.; Zhu, C.; Nangia, S.; Truhlar, D. G. Introductory Lecture: Nonadiabatic Effects in Chemical Dynamics. *Faraday Discuss.* **2004**, *127*, 1-22.
[245] Zhu, C.; Jasper, A. W.; Truhlar, D. G. Non-Born-Oppenheimer Liouville-von Neumann Dynamics. Evolution of a Subsystem Controlled by Linear and Population-Driven Decay of Mixing with Decoherent and Coherent Switching. *J. Chem. Theory Comput.* **2005**, *1*, 527-540.
[246]Truhlar, D. G. Decoherence in Combined Quantum Mechanical and Classical Mechanical Methods for Dynamics as Illustrated for Non-Born-Oppenheimer Dynamics. In *Quantum Dynamics of Complex Molecular Systems*; Micha, D. A., Burghardt, I., Eds.; Springer: Berlin, 2007; pp. 227–243.
[247] Cheng, S. C.; Zhu, C.; Liang, K. K.; Lin, S. H.; Truhlar, D. G. Algorithmic Decoherence Time for Decay of Mixing Non-Born-Oppenheimer Dynamics, *J. Chem. Phys.* **2008**, *129*, 024112.

[248] Jasper, A. W.; Truhlar, D. G. Non-Born-Oppenheimer Molecular Dynamics for Conical Intersections, Avoided Crossings, and Weak Interactions, in *Conical Intersections: Theory, Computation, and Experiment*, Domcke, W.; Yarkony, D. R.; Köppel, H., Eds.; World Scientific: Singapore, 2011; pp. 375-412.

Chapter 4 Parametrically Managed Activation Function for Fitting a Neural Network Potential with Physical Behavior Enforced by a Low-Dimensional Potential

In part from

Akher, F. B.; Shu, Y.; Varga; Z.; Bhaumik, S.; Truhlar, D. G. Parametrically Managed Activation Function for Fitting a Neural Network Potential with Physical Behavior Enforced by a Low-Dimensional Potential. *J. Phys. Chem. A* **2023,** *127*, 5287-5297.

4.1 Introduction

Application of machine learning to chemical and physical problems is a growing field with applications ranging from discovery of new molecules and materials to improving existing theoretical models.[249-263] The present article is about using machine learning to represent potential energy surfaces for small molecules and chemical reactions.[264-301]

The methods discussed in this article can be used for representing sets of coupled potential energy surfaces as required for simulating electronically nonadiabatic photochemical processes. Although we treat the difficult case of coupled potential energy surfaces for electronically nonadiabatic processes, the new kind of method we present should also be useful for uncoupled surfaces used to treat processes for which the Born-Oppenheimer approximation is valid.

Representation of coupled potential energy surfaces for multiple electronic states has been advanced by means of progress on diabatization methods, which have been reviewed recently.[302] Diabatization enables the study of nonadiabatic processes with nuclear quantum dynamics or with large ensembles of long-time semiclassical nonadiabatic dynamics. Two methods are competing for adoption, namely neural networks and multilinear regression with high-order polynomials. From a supervised-learning perspective, although both are universal, neural networks are gaining a stronger foothold in the field due to their high convenience.[303] However, a notorious drawback for machine-learned potentials is their unreliable behavior when applied to data quite different from that used for training. For example, it's easy for neural-network potentials to acquire unphysical holes or unphysical barriers and/or to have the wrong asymptotic behavior.

Maintaining physical behavior in regions where one or more interatomic distance is very large or very small is hard because one does not usually saturate such regions of space with training data. When poor physical behavior arises, one often resorts to an iterative scheme: fit the surfaces, run trajectories to discover regions of space where the fit is unphysical, add data in the problematic regions, refit, and iterate the steps until no more unphysical behavior is found. However, this is problematic for maintaining physical

behavior at large internuclear separation because the amount of space in asymptotic regions is infinite. And it can be troublesome in regions where two or more atoms get very close because the potential is very steep in those regions.

In this work, we will introduce a new step in the machine-learning procedure, namely, a parametrically managed activation function. This is designed so that the potential representation in difficult regions inherits the correct physical behavior of lower-dimensional potentials. We will introduce the parametrically managed activation function in the context of the methods of diabatization by deep neural network[282] (DDNN) and permutationally restrained DDNN[287] (PR-DDNN), but the type of approach employed here should also be useful for other uses of neural networks to represent potential energy surfaces. Section 4.2.1 reviews the relevant aspects of the DDNN and PR-DDNN schemes. Section 4.2.2 presents the new method. Section 4.3 illustrates the new method by using it to obtain improved potential energy surfaces for O + O_2 collisions in the $^3A'$ electronic state manifold.

4.2 Methods

4.2.1 Diabatization by deep neural network and permutationally restrained diabatization by deep neural network

We first introduce diabatization by deep neural network (DDNN).[282] The DDNN method is based on a diabatic potential energy matrix (DPEM), whose eigenvalues are the adiabatic potential energies. The diagonal elements $\mathbf{U}_{j,\beta\beta}$ of the DPEM at geometry j are the diabatic potential energies, and the off-diagonal elements $\mathbf{U}_{j,\beta\gamma}$ are called diabatic couplings. Because the elements of the DPEM are smooth and the adiabatic potentials are not smooth, the strategy adopted is to fit the DPEM and recover the adiabatic potentials by diagonalization. An $N_{\text{states}} \times N_{\text{states}}$ DPEM whose eigenvalues are the N_{states} adiabatic potential energies of interest is called an adiabatic equivalent.

The DDNN architecture is a fully connected feedforward network with an additional adiabatic potential energy layer at the end. Therefore, the DDNN architecture has four

types of layers: an input layer, hidden layers, a diabatic potential energy matrix (DPEM) layer, and an adiabatic potential energy layer. The DDNN architecture is illustrated in Figure 24.

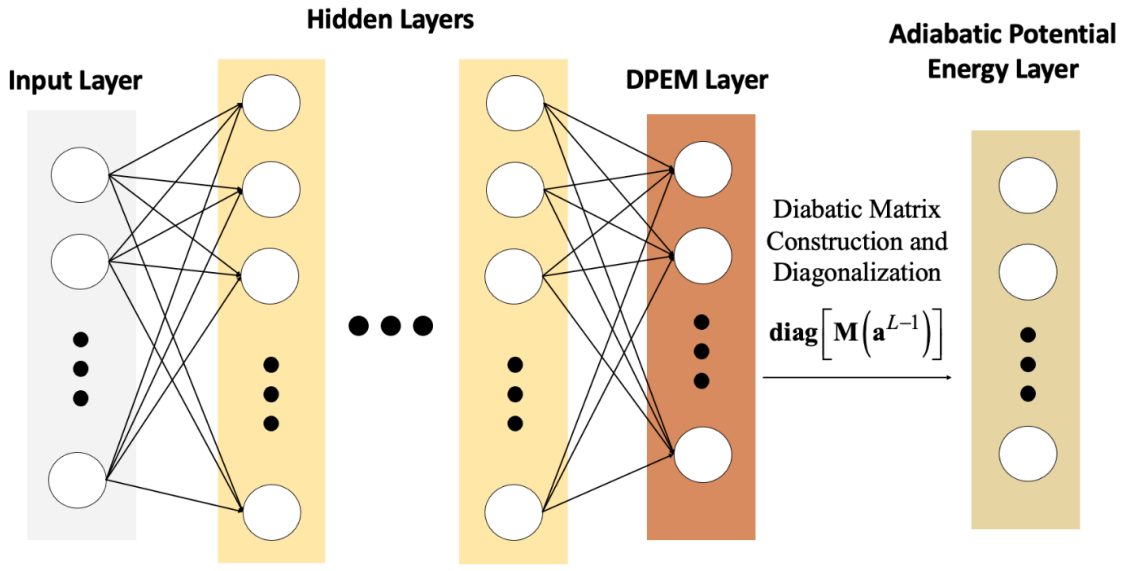

Figure 24: Architecture for diabatization by deep neural network

To train the weights and biases in DDNN, one uses two input databases, namely, an adiabatic database $\mathcal{N}$ and a diabatic cost-function database $\mathcal{I}$. Database $\mathcal{N}$ has N geometries (n = 1, 2, …, N), for each of which it has an N_{states}-dimensional vector $\mathbf{V}_n$ whose elements are target adiabatic energies. Database $\mathcal{I}$ has J geometries (j = 1, 2, …, J), for each of which it has an N_{st}-dimensional vector $\mathbf{\Xi}_j$ whose elements are the unique target diabatic matrix elements. In particular, N_{st} is $\frac{1}{2}N_{\text{states}}(N_{\text{states}}+1)$, and the elements of $\mathbf{\Xi}_j$ are the unique matrix elements of the symmetric $N_{\text{states}} \times N_{\text{states}}$ DPEM. In practical applications, $\mathcal{I}$ is a subset of $\mathcal{N}$, and usually $J << N$.

For an L-layer DDNN, the input layer for geometry n is $\mathbf{a}_n^1$, the hidden layers are $\mathbf{a}_n^2$ to $\mathbf{a}_n^{L-2}$, the DPEM layer is $\mathbf{a}_n^{L-1}$, and the adiabatic potential energy layer is $\mathbf{a}_n^L$. The propagation from the input layer to hidden layers is done by

$$\mathbf{a}_n^{l+1} = g(\boldsymbol{z}^l) = g[(\mathbf{w}^l)^{\mathrm{T}}\mathbf{a}_n^l + \mathbf{b}^l], \quad l = 1,2,..,L-3 \tag{1}$$

where a superscript T denotes a transpose, $\mathbf{w}^l$ and $\mathbf{b}^l$ are respectively the connection weights and biases of layer l, and g is the hidden-layer activation function. Nonlinear hidden layer activation functions like rectified linear unit (ReLU)[304] or Gaussian Error Linear Unit (GELU)[305] are suggested to prevent the vanishing gradient problem.[306] Note that GELU is an improved version of ReLU with a global continuous behavior. The GELU activation function is defined as

$$g(z_m^l) = \frac{1}{2} z_m^l \left(1 + \mathrm{erf}\left(\frac{1}{\sqrt{2}} z_m^l \right) \right) \tag{2}$$

where z_m^l is element m of the M-dimensional vector $\boldsymbol{z}^l$, and erf denotes the error function. Propagation from the last hidden layer to the DPEM layer employs an identity activation function,

$$\mathbf{a}_n^{L-1} = (\mathbf{w}^{L-2})^{\mathrm{T}} \mathbf{a}_n^{L-2} + \mathbf{b}^{L-2} \tag{3}$$

Because of we are considering an adiabatic-equivalent diabatic representation, the $\mathbf{a}_n^{L-1}$ is a vector with length of N_{st}, which is the number of unique elements of DPEM. For each geometry n, converting vector $\mathbf{a}_n^{L-1}$ to a DPEM matrix $\mathbf{U}_n$ and diagonalizing $\mathbf{U}_n$ forms the adiabatic potential energy layer $\mathbf{a}_n^L$. Therefore, the adiabatic potential energy layer is not a direct output of the feed-forward fully connected multi-layer perceptron part of the neural network. The DDNN cost function is

$$\begin{aligned} c_{\mathrm{DDNN}} = {} & \frac{1}{2NN_{\mathrm{states}}} \sum_{n=1}^{N} \left| \mathbf{a}_n^L - \mathbf{V}_n \right|^2 + \frac{\alpha_1}{2JN_{\mathrm{states}}} \sum_{j=1}^{J} \left| \mathbf{a}_j^{L-1} - \boldsymbol{\Xi}_j \right|^2 \\ & + \frac{\alpha_2}{2} \sum_{l=1}^{L-2} \sum_{p} \sum_{p'} \left| w_{pp'}^l \right|^2 \end{aligned} \tag{4}$$

where the last term is a regularization[307] that is employed to help prevent overfitting, and α_1 and α_2 are user-defined parameters of the network. This defines the DDNN method.

Optimization of the weights and biases according to eq (4) does not ensure that the adiabatic energies are invariant to permutation of identical nuclei. To promote permutational invariance, we add an additional database called permuted adiabatic database $\mathcal{S}$. Database $\mathcal{S}$ has $S = N_{\mathrm{p}} N$ geometries, where N_{p} is the number of non-identity

permutations of identical nuclei. For example, in O_3, there are three transpositions and two cyclic permutations of O atoms, and hence $N_\mathrm{p} = 5$. For each geometry s in the permuted adiabatic database $\mathcal{S}$, the target adiabatic potential energies $\mathbf{V}_s$ are known because they are identical to those for the unpermuted geometries in database $\mathcal{N}$.

The permutationally restrained DDNN (PR-DDNN)[287] method has the same architecture as DDNN, but the cost function is changed to,

$$c_{\mathrm{PR-DDNN}} = \frac{1}{2NN_{\mathrm{states}}}\sum_{n=1}^{N}\left|\mathbf{a}_n^L - \mathbf{V}_n\right|^2 + \frac{\alpha_1}{2JN_{\mathrm{states}}}\sum_{j=1}^{J}\left|\mathbf{a}_j^{L-1} - \boldsymbol{\Xi}_j\right|^2 + \frac{\alpha_2}{2}\sum_{l=1}^{L-2}\sum_{p}\sum_{p'}\left|w_{pp'}^l\right|^2 + \frac{1}{2SN_{\mathrm{states}}}\sum_{s=1}^{S}\left|\mathbf{a}_s^L - \mathbf{V}_s\right|^2 \quad (5)$$

The last term in eq (5) promotes permutational invariance.

Note that an alternative to the above would be to *constrain* the permutation invariance of identical nuclei rather than to restrain it. This could be accomplished by using permutationally invariant input for input layer $\mathbf{a}_n^1$ (which constrains permutation invariance in the input stage), for example permutationally invariant polynomials[266,308] or fundamental invariants,[271] or by using an equivariant neural network that constrains permutation invariance in the output stage.[309] Both approaches constrain the permutational invariance of adiabatic potential energies as well as DPEM elements. However, DPEM elements are not necessarily permutationally invariant,[302] and the PR-DDNN method allows the combination of permutational variance of the diabatic representation with permutational invariance of the adiabatic one. Furthermore, the PR-DDNN method recognizes that one does not fit the unpermuted adiabatic data perfectly and allows imperfect fitting of permutational invariance, which is a balanced approach, rather than insisting that exact permutational invariance be combined with inexact fitting of adiabatic potentials.

4.2.2 The new method

4.2.2.1 Separation of the interaction potential from a low-dimensional potential at a dissociation limit

The global potential energy surface of a many-body system often reduces in dimensionality at the dissociation limit. For example, when O is separated from O_2, an O_3 global adiabatic potential energy surface, which depends on three internal coordinates, should reduce to a one-dimensional diatomic potential energy surface of O_2 (that depends on the electronic state of O_2) plus a constant (which is the energy of a given state of O). To treat dissociation, we assume the entire system Z is composed of subsystems X and Y, and we considering the reaction

$$\mathrm{X} + \mathrm{Y} \rightarrow \mathrm{Z} \tag{6}$$

We let $\mathbf{R}_\mathrm{Z}$ denote the entire set of coordinates, we let $\mathbf{R}_\mathrm{X}$ denote the subset of coordinates pertaining to X, and we let $\mathbf{R}_\mathrm{Y}$ denote the subset of coordinates of Y. The adiabatic potential energy $E_\mathrm{Z}(\mathbf{R}_\mathrm{Z})$ of Z at geometry $\mathbf{R}_\mathrm{Z}$ can be written for a single electronic state as

$$E_\mathrm{Z}(\mathbf{R}_\mathrm{Z}) = E_\mathrm{X}(\mathbf{R}_\mathrm{X}) + E_\mathrm{Y}(\mathbf{R}_\mathrm{Y}) + E_\mathrm{AD}(\mathbf{R}_\mathrm{Z}) \tag{7}$$

where $E_\mathrm{X}(\mathbf{R}_\mathrm{X})$ is the adiabatic potential energy of X at geometry $\mathbf{R}_\mathrm{X}$, $E_\mathrm{Y}(\mathbf{R}_\mathrm{Y})$ is the adiabatic potential energy of Y at geometry $\mathbf{R}_\mathrm{Y}$, and $E_\mathrm{AD}(\mathbf{R}_\mathrm{Z})$ is the interaction potential energy, which will be called the added-dimensions (AD) potential energy because that is a more suitable name for the general case introduced in Section 4.2.2.2. Therefore, at the dissociation limit where X and Y are separated, the added-dimensions potential energy $E_\mathrm{AD}(\mathbf{R}_\mathrm{Z})$ is equal to 0. Let n_X and n_Y be the number of atoms in X and Y. Since the potential energy depends only on internal coordinates, $E_\mathrm{X}(\mathbf{R}_\mathrm{X}) + E_\mathrm{Y}(\mathbf{R}_\mathrm{Y})$ has a lower dimensionality than $E_\mathrm{Z}(\mathbf{R}_\mathrm{Z})$, and we label this sum as the low-dimensional (LD) adiabatic potential energy $E^\mathrm{LD}(\mathbf{R}_\mathrm{Z})$. For example, if X and Y are both polyatomic, then $E^\mathrm{LD}(\mathbf{R}_\mathrm{Z})$ is $(3n_\mathrm{X} + 3n_\mathrm{Y} - 12)$-dimensional, whereas $E_\mathrm{Z}(\mathbf{R}_\mathrm{Z})$ is $(3n_\mathrm{X} + 3n_\mathrm{Y} - 6)$-dimensional. If X is O_2 and Y is O, then $E^\mathrm{LD}(\mathbf{R}_\mathrm{Z})$ is 1-dimensional, but $E_\mathrm{Z}(\mathbf{R}_\mathrm{Z})$ is 3-dimensional. Notice that the low-dimensional potential $\mathbf{U}^\mathrm{LD}(\mathbf{R}_\mathrm{Z})$ is independent of the separation distance of X and Y, and therefore it is only decided by internal degrees of freedom of X and Y.

When we consider a multi-state problem, where N_X, N_Y, and N_Z are, respectively, the number of electronic states considered for X, Y, and Z, we have

$$N_{\mathrm{Z}} = N_{\mathrm{X}} N_{Y} \tag{8}$$

For example, considering 2 electronic states of X and 3 electronic states of Y, the total number of electronic states Z considered equals 6:

$$E_{\mathrm{Z},1}(\mathbf{R}_{\mathrm{Z}}) = E_{\mathrm{X},1}(\mathbf{R}_{\mathrm{X}}) + E_{\mathrm{Y},1}(\mathbf{R}_{\mathrm{Y}}) + E_{\mathrm{AD},1}(\mathbf{R}_{\mathrm{Z}}) = E_{1}^{\mathrm{LD}}(\mathbf{R}_{\mathrm{Z}}) + E_{\mathrm{AD},1}(\mathbf{R}_{\mathrm{Z}}) \tag{9}$$

$$E_{\mathrm{Z},2}(\mathbf{R}_{\mathrm{Z}}) = E_{\mathrm{X},1}(\mathbf{R}_{\mathrm{X}}) + E_{\mathrm{Y},2}(\mathbf{R}_{\mathrm{Y}}) + E_{\mathrm{AD},2}(\mathbf{R}_{\mathrm{Z}}) = E_{2}^{\mathrm{LD}}(\mathbf{R}_{\mathrm{Z}}) + E_{\mathrm{AD},2}(\mathbf{R}_{\mathrm{Z}}) \tag{10}$$

$$E_{\mathrm{Z},3}(\mathbf{R}_{\mathrm{Z}}) = E_{\mathrm{X},1}(\mathbf{R}_{\mathrm{X}}) + E_{\mathrm{Y},3}(\mathbf{R}_{\mathrm{Y}}) + E_{\mathrm{AD},3}(\mathbf{R}_{\mathrm{Z}}) = E_{3}^{\mathrm{LD}}(\mathbf{R}_{\mathrm{Z}}) + E_{\mathrm{AD},3}(\mathbf{R}_{\mathrm{Z}}) \tag{11}$$

$$E_{\mathrm{Z},4}(\mathbf{R}_{\mathrm{Z}}) = E_{\mathrm{X},2}(\mathbf{R}_{\mathrm{X}}) + E_{\mathrm{Y},1}(\mathbf{R}_{\mathrm{Y}}) + E_{\mathrm{AD},4}(\mathbf{R}_{\mathrm{Z}}) = E_{4}^{\mathrm{LD}}(\mathbf{R}_{\mathrm{Z}}) + E_{\mathrm{AD},4}(\mathbf{R}_{\mathrm{Z}}) \tag{12}$$

$$E_{\mathrm{Z},5}(\mathbf{R}_{\mathrm{Z}}) = E_{\mathrm{X},2}(\mathbf{R}_{\mathrm{X}}) + E_{\mathrm{Y},2}(\mathbf{R}_{\mathrm{Y}}) + E_{\mathrm{AD},5}(\mathbf{R}_{\mathrm{Z}}) = E_{5}^{\mathrm{LD}}(\mathbf{R}_{\mathrm{Z}}) + E_{\mathrm{AD},5}(\mathbf{R}_{\mathrm{Z}}) \tag{13}$$

$$E_{\mathrm{Z},6}(\mathbf{R}_{\mathrm{Z}}) = E_{\mathrm{X},2}(\mathbf{R}_{\mathrm{X}}) + E_{\mathrm{Y},3}(\mathbf{R}_{\mathrm{Y}}) + E_{\mathrm{AD},6}(\mathbf{R}_{\mathrm{Z}}) = E_{6}^{\mathrm{LD}}(\mathbf{R}_{\mathrm{Z}}) + E_{\mathrm{AD},6}(\mathbf{R}_{\mathrm{Z}}) \tag{14}$$

where the number in the subscript of E is a state index. Hence, eq (7) can be extended to multi-state problems as

$$\mathbf{E}_{\mathrm{Z}}(\mathbf{R}_{\mathrm{Z}}) = \mathbf{E}_{\mathrm{X}}(\mathbf{R}_{\mathrm{X}}) + \mathbf{E}_{\mathrm{Y}}(\mathbf{R}_{\mathrm{Y}}) + \mathbf{E}_{\mathrm{AD}}(\mathbf{R}_{\mathrm{Z}}) = \mathbf{E}^{\mathrm{LD}}(\mathbf{R}_{\mathrm{Z}}) + \mathbf{E}_{\mathrm{AD}}(\mathbf{R}_{\mathrm{Z}}) \tag{15}$$

where $\mathbf{E}_{\mathrm{Z}}(\mathbf{R}_{\mathrm{Z}})$, $\mathbf{E}_{\mathrm{X}}(\mathbf{R}_{\mathrm{X}})$, $\mathbf{E}_{\mathrm{Y}}(\mathbf{R}_{\mathrm{Y}})$, $\mathbf{E}^{\mathrm{LD}}(\mathbf{R}_{\mathrm{Z}})$ and $\mathbf{E}_{\mathrm{AD}}(\mathbf{R}_{\mathrm{Z}})$ are N_{Z}-dimensional vectors. We will denote the β element (component) of a vector $\mathbf{E}$ as E_{β}. Let $\mathbf{R}_{\mathrm{Z},\infty}$ indicate a geometry where X is separated from Y; then constraining the potential of a high-dimensional system to that of a low-dimensional system in the dissociation limit means that $\mathbf{E}_{\mathrm{AD}}(\mathbf{R}_{\mathrm{Z},\infty})$ is an N_{Z}-dimensional zero vector.

Note that $\mathbf{E}_{\mathrm{Z}}(\mathbf{R}_{\mathrm{Z}})$ is not the final adiabatic potential energy vector of Z because the elements are not sorted in energetic order. In practice, our preferred choice of diabatic representation usually satisfies the constraint that at any dissociation geometry (where $\mathbf{R}_{\mathrm{Z}}$ equals $\mathbf{R}_{\mathrm{Z},\infty}$), the diabatic potentials equal the adiabatic ones, although they might be in a different order. We will assume this usual constraint in the present article. However, we will also require the following constraints that include state ordering:

$$U_{\beta\beta}(\mathbf{R}_{\mathrm{Z},\infty}) = U_{\beta\beta}^{\mathrm{LD}}(\mathbf{R}_{\mathrm{Z},\infty}) = E_{\beta}^{\mathrm{LD}}(\mathbf{R}_{\mathrm{Z},\infty}) = E_{\mathrm{Z},\beta}(\mathbf{R}_{\mathrm{Z},\infty}) \tag{16}$$

And the diabatic couplings at separation satisfy

$$U_{\beta\gamma}(\mathbf{R}_{\mathrm{Z},\infty}) = U_{\beta\gamma}^{\mathrm{LD}}(\mathbf{R}_{\mathrm{Z},\infty}) = 0, \quad \beta \neq \gamma \tag{17}$$

In general, we have

$$\mathbf{U}(\mathbf{R}_\mathrm{Z}) = \mathbf{U}^\mathrm{LD}(\mathbf{R}_\mathrm{Z}) + \mathbf{U}_\mathrm{AD}(\mathbf{R}_\mathrm{Z}) \tag{18}$$

The adiabatic potential energies at $\mathbf{R}_{\mathrm{Z},\infty}$ are computed by diagonalizing $\mathbf{U}(\mathbf{R}_{\mathrm{Z},\infty})$. At geometries where X and Y are not separated, diagonalizing $\mathbf{U}(\mathbf{R}_\mathrm{Z})$ yields $\mathbf{V}(\mathbf{R}_\mathrm{Z})$, which is the same as $\mathbf{E}_\mathrm{Z}(\mathbf{R}_\mathrm{Z})$ up to a permutation of vector elements.

4.2.2.2. More general separation of the potential into LD and AD parts

Next, we recast the formalism to treat it any low-dimensional potential that vanishes or may be assumed to vanish when the subsystems separate, i.e., the LD potential need not be the sum of the potential of X and the potential of Y, and the AD potential need not be the interaction between two subsystems. We let $\mathbf{R}_\mathrm{LD}$ denote any geometry where the system is dissociated or where the AD potential is to be approximated as zero. We employ a diabatic representation in which

$$\mathbf{U}(\mathbf{R}) = \mathbf{U}^\mathrm{LD}(\mathbf{R}) + \mathbf{U}_\mathrm{AD}(\mathbf{R}) \tag{19}$$

and $\mathbf{U}^\mathrm{LD}(\mathbf{R})$ is diagonal. We also have

$$\mathbf{V}(\mathbf{R}) = \mathbf{V}^\mathrm{LD}(\mathbf{R}) + \mathbf{V}_\mathrm{AD}(\mathbf{R}) \tag{20}$$

where $\mathbf{V}(\mathbf{R})$ is a vector consisting of the eigenvalues of $\mathbf{U}(\mathbf{R})$. Our goal is to constrain $\mathbf{U}(\mathbf{R}_\mathrm{LD})$ to equal $\mathbf{U}^\mathrm{LD}(\mathbf{R}_\mathrm{LD})$ and thus to constrain $\mathbf{U}_\mathrm{AD}(\mathbf{R}_\mathrm{LD})$ to equal $\mathbf{0}$.

Employing eqs (19) and (20) in DDNN and PR-DDNN, the cost functions are respectively

$$\begin{aligned} c_\mathrm{DDNN} = \frac{1}{2NN_\mathrm{states}}\sum_{n=1}^{N}\left|\mathbf{a}_n^L - \mathbf{V}_n\right|^2 + \frac{\alpha_1}{2JN_\mathrm{states}}\sum_{j=1}^{J}\left|\mathbf{a}_j^{L-1} + \boldsymbol{\Xi}_j^\mathrm{LD} - \boldsymbol{\Xi}_j\right|^2 \\ + \frac{\alpha_2}{2}\sum_{l=1}^{L-2}\sum_{p}\sum_{p'}\left|w_{pp'}^l\right|^2 \end{aligned} \tag{21}$$

and

$$c_{\mathrm{PR-DDNN}} = c_{\mathrm{DDNN}} + \frac{1}{2SN_{\mathrm{states}}} \sum_{s=1}^{S} \left| \mathbf{a}_s^L - \mathbf{V}_s \right|^2 \tag{22}$$

where $\boldsymbol{\Xi}_j^{\mathrm{LD}}$ is a vector of the unique matrix elements of $\mathbf{U}^{\mathrm{LD}}$ defined in eq (19).

We do not enforce the permutation symmetry in PR-DDNN by using permutationally symmetric input coordinates or using a symmetrized neutral network architecture. This is because the DDNN architecture finds a diabatic representation and fits the DPEM, and diabatic representations are not necessarily permutationally invariant.[302] Our architecture allows diabatic representation to have the desired flexibility to not be permutationally invariant.[287] The resulting adiabatic potentials are restrained by the new term of eq 22 to have approximate permutational invariance; just as we do not fit the adiabatic potentials exactly but rather with some residual deviation, we also do not enforce permutational symmetry exactly but rather we allow some residual deviation.

Notice that

$$\boldsymbol{\Xi}_j^{\mathrm{LD}} - \boldsymbol{\Xi}_j = -\boldsymbol{\Xi}_{\mathrm{AD},j} \tag{23}$$

where $\boldsymbol{\Xi}_{\mathrm{AD},j}$ is a vector of unique matrix elements of $\mathbf{U}_{\mathrm{AD}}$ defined in eq (19). Therefore, we are effectively using the feedforward neural networks of DDNN and PR-DDNN to fit the interaction DPEM $\mathbf{U}_{\mathrm{AD}}$. We add the low-dimensional DPEM $\mathbf{U}^{\mathrm{LD}}$ at the DPEM layer, which is layer L-1. Diagonalizing the DPEM yields the final adiabatic potential energy. Constraining the potential of the high-dimensional system to be a function of the low-dimensional subsystems in the dissociation limit means that DDNN and PR-DDNN predict zero vectors for DPEM layer for dissociation limit geometries,

$$\mathbf{a}_{n\in\mathrm{LD}}^{L-1} = \mathbf{0} \tag{24}$$

where "$n \in$ LD" denotes that geometry n corresponds to the dissociation limit.

One possible application of the more general formalism presented in this section is to treat dissociation when the LD potential is not simply the sum of two fragment potentials and hence the AD potential is not simply the interaction potential. An example of this kind

of application is discussed in Sections 4.2.2.3 and 4.3. In that example, we apply the theory where LD is the two-body approximation, and AD is the many-body correction to the two-body approximation.

Another example of an application where this kind of treatment can be useful is the region where two atoms get close. In such regions, the potential is very steep, and any analytic fit extrapolated into this region is liable to have wells instead of steep repulsive wall. However, a system with n_Z atoms has $n_Z(n_Z - 1)/2$ internuclear distances. Because this is quadratic in the number of atoms, it is often prohibitive to include data in all regions where two atoms get close. However, one often does not need quantitative accuracy in regions where the repulsive interaction is very large; one simply needs to be sure that the analytic potential is repulsive enough to keep trajectories from unphysically entering such a region. A pairwise additive potential is repulsive in any such region, and designing the full potential be a pairwise potential plus corrections is a reasonable strategy.[310] Then, having the full potential reduce to a pairwise additive repulsive potential in highly repulsive regions without having data there would be a convenient way to ensure a physical fit at close distances. Note that for $n_Z > 4$, $n_Z(n_Z - 1)/2$ is greater than $3n_Z - 6$, so a pairwise additive potential does not depend on less coordinates than $3n_Z - 6$, but rather it is a sum of lower-dimensional potentials (in this case a sum of 1-dimensional potentials), and that is what we signify when we label it as LD.

4.2.2.3. Parametrically managed activation function

As mentioned in the introduction and in Section 4.2.2.2, we anticipate two kinds of region where the potential can be set to the LD potential. One is the region where two subsystems dissociate, and another region is where two atoms get very close. To illustrate the use of a parametrically managed activation function, we next give an example suitable for treating the dissociation case. Section 4.2.2.1 converted the problem of achieving a physical extrapolation to asymptotic regions into the problem of how to satisfy eq (24). In regression problems, the output layer often employs the identity function as an output activation function as shown in eq (3). To satisfy eq (24), we generalize eq (3) to

$$\boldsymbol{z}^{L-1} = (\mathbf{w}^{L-2})^{\mathrm{T}}\mathbf{a}_n^{L-2} + \mathbf{b}^{L-2} \tag{25}$$

$$\mathbf{a}_n^{L-1} = F[\boldsymbol{z}^{L-1}, \mathbf{R}] \tag{26}$$

where F should satisfy eq (24). We call F a parametrically managed activation function. Therefore, we are looking for a function that is parametrically dependent on **R**, and which yields a zero vector when $\mathbf{R} = \mathbf{R}_{\mathrm{LD}}$, that is

$$F[\mathbf{z}; \mathbf{R}] = \mathbf{0} \tag{27}$$

We choose an element-wise definition that depends on the distance $r_{\mathrm{diss},n}$ between subsystems in geometry n and that has the shape of a smoothed boxcar window (SBW) function:

$$F[z_m^{L-1}; \mathbf{R}] = f_1(r_{\mathrm{diss},n}) f_2(r_{\mathrm{diss},n}) z_m^{L-1} \tag{28}$$

where z_m^{L-1} is the mth element of vector $\boldsymbol{z}^{L-1}$, and

$$f_1(r_{\mathrm{diss},n}) = 0.5 + 0.5\tanh\left(f\left(r_{\mathrm{diss},n} - a\right)\right) \tag{29}$$

$$f_2(r_{\mathrm{diss},n}) = 0.5 + 0.5\tanh\left(f\left(-r_{\mathrm{diss},n} + b\right)\right) \tag{30}$$

where f, a, and b are parameters. Employing the SBW parametrically managed activation function defined in eqs (28) – (30) in conjunction with the formalism of Section 4.3 will produce a fit to the interaction potential that is damped out, except when the separation distance is approximately in the interval $a < r_{\mathrm{diss},n} < b$. Figure 25 shows the shape of $f_1(r_{\mathrm{diss},n}) f_2(r_{\mathrm{diss},n})$ as a function of $r_{\mathrm{diss},n}$ with f = 2.0 Å^{-1}, a = 2.0 Å, and b = 8.0 Å. Since the left and right tails decay to zero exponentially, the resulting potential decreases exponentially to the desired limit of eq (27).

In practical applications, we often want to use a negative a value, i.e., we want to have non-zero added-dimensions potentials from neural networks when separation distance is short.

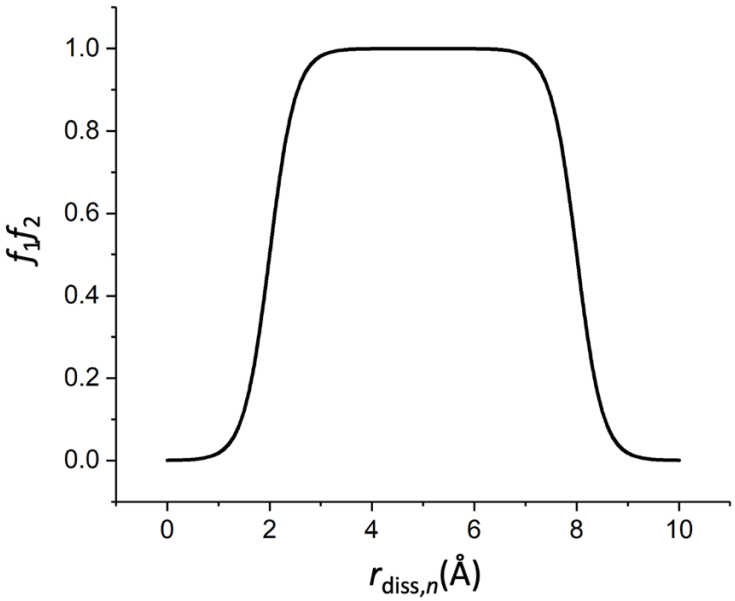

Figure 25: Value of $f_1 f_2$ as a function of $r_{\mathrm{diss},n}$ with f = 2.0 Å^{-1}, a = 2.0 Å, and b = 8.0 Å.

4.2.2.4. Parametrically managed diabatization by deep neural network

Now we combine PR-DDNN with separation of the interaction potential from the low-dimensional potential with the SBW parametrically managed activation function for semi-automatic simultaneous diabatization and adiabatic surface fitting. We will call the neural network that combines these features a parametrically managed DDNN or PM-DDNN. The PM-DDNN forces the global potential energy surfaces to behave as low-dimensional potentials at dissociation-limit geometries.

In PM-DDNN, the propagation from the input layer to the last hidden layer follows eqs (1) and (2). Propagation from last hidden layer to DPEM layer follows

$$\mathbf{a}_n^{L-1} = F[((\mathbf{w}^{L-2})^{\mathrm{T}}\mathbf{a}_n^{L-2} + \mathbf{b}^{L-2}); \mathbf{R}_n] + \boldsymbol{\Xi}_n^{\mathrm{LD}} \tag{31}$$

Where we recall that $\mathbf{R}_n$ is the nuclear configuration of geometry n, and $\boldsymbol{\Xi}_n^{\mathrm{LD}}$ contains the unique LD DPEM elements. The adiabatic potential energy layer is

$$\mathbf{a}_n^{L} = \mathrm{diag}[\mathbf{M}(\mathbf{a}_n^{L-1})] \tag{32}$$

where $\mathbf{M}(\mathbf{a}_n^{L-1})$ denotes a conversion from DPEM layer to DPEM (i.e., from the unique elements of the DPEM stored as a vector to the full matrix form), and $\mathrm{diag}[\mathbf{M}(\mathbf{a}_n^{L-1})]$

denotes the diagonalization of the DPEM. The PM-DDNN approach employs following cost function,

$$c_{\mathrm{PM-DDNN}} = \frac{1}{2NN_{\mathrm{states}}}\sum_{n=1}^{N}\left|\mathbf{a}_n^L - \mathbf{V}_n\right|^2 + \frac{\alpha_1}{2JN_{\mathrm{states}}}\sum_{j=1}^{J}\left|\mathbf{a}_j^{L-1} - \boldsymbol{\Xi}_j\right|^2 + \frac{\alpha_2}{2}\sum_{l=1}^{L-2}\sum_{p}\sum_{p'}\left|w_{pp'}^{l}\right|^2 + \frac{1}{2SN_{\mathrm{states}}}\sum_{s=1}^{S}\left|\mathbf{a}_s^L - \mathbf{V}_s\right|^2 \tag{33}$$

The PM-DDNN architecture is shown in Figure 26.

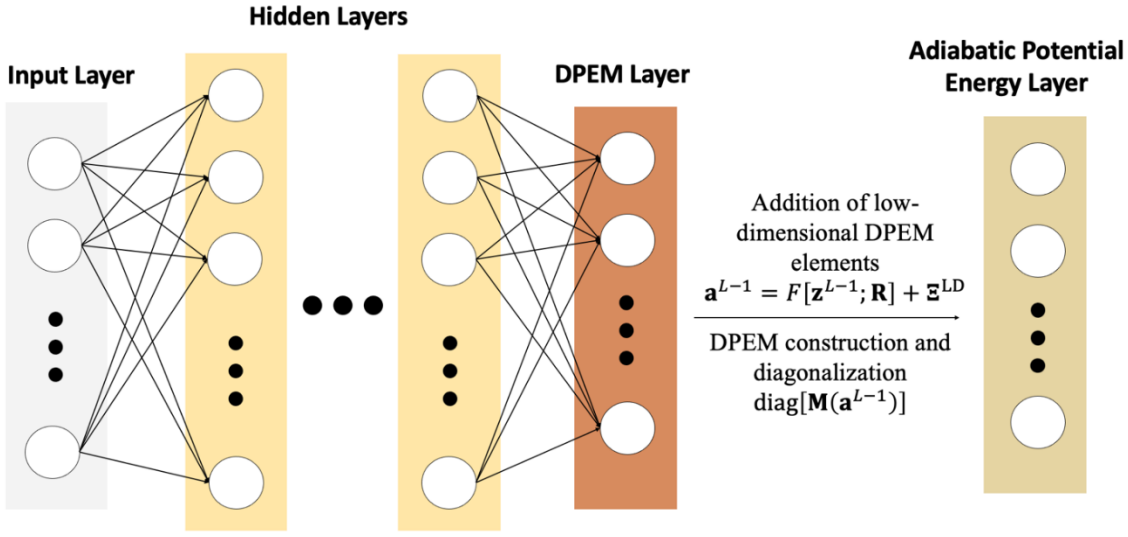

Figure 26: Architecture for parametrically managed diabatization by deep neural network.

4.3 Results

We illustrate the usefulness of PM-DDNN by using it to improve the recently developed[292] 14-state set of triplet O_3 A' global potential energy surfaces. We label the version published in ref. 292 as version 2022 and current version as version 2023. To develop version 2022, we used PR-DDNN, and we separated the interaction potential from the low-dimensional potential, but we did not use the parametrically managed activation function. Version 2023 adds the parametrically managed activation function.

Because O_3 is a three-atom system, the LD potential involves the diatomic potential of O_2 (a function) plus the energy of a given state of O (a single value). The global fitting

procedure involves a multi-stage process involving supervised learning for one-dimensional and two-dimensional cuts, followed by representation of the final three-dimensional global surface. The fitting procedure is presented in ref. 292, and only three changes were made: (i) we improved the diatomic potentials; (ii) we added the parametrically managed activation function; (iii) we re-optimized the number of neurons in the hidden layers of the net. Details that have not changed are not repeated here, and the readers is referred to the previous paper for details of steps that have not changed.

The LD potential of O_3 is written as

$$\left(\mathbf{U}^{\mathrm{LD}}\right)_{mm} = V_0 + \sum_{i=1}^{3} V_m^{\mathrm{PA}}\left(r_{i,n}\right) \tag{34}$$

where m is an electronic state index, V_0 is a constant that is set to dissociation energy of ground-state $O_2(\,^3\Sigma_g^-)$, $r_{i,n}$, is a one of the three internuclear distances (i = 1, 2, 3) at geometry n, and the sum is over pairwise-additive (PA) contributions of the potentials of the diatomic subsystems. The 2023 potential uses improved fits to the diatomic potentials. The improved diatomic fits are presented in the Appendix.

The separation parameter, $r_{\mathrm{diss},n}$, for the parametrically managed activation function is taken as

$$r_{\mathrm{diss},n} = \max\left(r_{1,n}, r_{2,n}, r_{3,n}\right) \tag{35}$$

The three O–O distances $\left(r_{1,n}, r_{2,n}, r_{3,n}\right)$ are used in an input vector in the PM-DDNN calculations.

We set a equal to a negative number, in particular a = –2.0 a_0, because we are only concerned with large values of $r_{\mathrm{diss},n}$ in the present application. (Note: 1 $a_0 \equiv 1$ bohr $\approx$ 0.5292 Å.) We set f equal to 2.0 a_0^{-1} and b equal to 7.5 a_0 because these choices of the parameters gave physical fits.

In the current work, $\alpha_1 = 1.0$, and $\alpha_2 = 0.0001$. The input adiabatic database contains the same 6340 geometries as described previously.[292]

We tested several node structures of PM-DDNN corresponding to different numbers of hidden layers and hidden layer neurons (HLNs). We made several runs with each combination, and the best mean unsigned errors (MUEs) of the unpermuted energies obtained for each node structure of PM-DDNN are provided in Table 6. The first and last number in the structure column are fixed because the first number corresponds to the number of input coordinates, and the final number corresponds to the number of unique DPEM elements. For the present 14-state system, we have 105 unique elements of the DPEM. The final selection of global surfaces involves a balanced compromise between accuracy and efficiency because a larger number of HLNs usually improves the accuracy but always raises the cost of evaluating the potential energies, couplings, and gradients during simulations.

Table 6: The best fitting results of various PM-DDNN neural-network node structures

HLNs [a]	PM-DDNN structure[b]	MUE (meV)[c]
	Final selection	
315	(*3, 30,65,95,125,105*)	61
	Other trials	
915	(*3,405,305,205,105*)	51
230	(*3,35,65,65,65,105*)	186
140	(*3,35,15,35,55,105*)	213
105	(*3,15,35,55,105*)	111

[a]This column gives the total number of hidden-layer neurons.

[b]The italic values correspond to the neuron numbers of hidden layers.

[c]MUE is the mean unsigned error in the adiabatic energies at the unpermuted geometries.

Our finally selected surface uses 30, 65, 95, and 125 neurons in four hidden layers. This final surface is available in the online version[311] of POTLIB.[312]

The final surface has a root-mean-square error of the adiabatic database (the unpermuted geometries used in the first term of the cost function) of 106 meV and a root-mean square error of the permuted adiabatic database (the last term of the cost function) of 126 meV. The closeness of these numbers shows that the restraint on energies at permuted geometries was successful. The mean unsigned error (MUE) of the unpermuted adiabatic database is 61 meV, and the mean signed error on the permuted adiabatic database is 68 meV. The smallness (106/61 = 1.74 and 126/68 = 1.85) of the ratios of the root-mean-squared errors to the MUEs is an indication that there are not an excessive number of large outliers.

In the long run, when the goal is a global potential energy surface, it is irrelevant whether a geometry is found in the permuted or unpermuted set, and we simply want a reasonably small error on all adiabatic energies. Table 7 provides further details of the MUEs of the entire set of 532560 adiabatic energies, breaking them down by electronic state and energy range. For each state in each energy range, the table shows the number of geometries and the MUE. At energies below 10 eV, the MUE is not a strong function of state. Close examination of the table shows remarkably good across-the-board accuracy up to 10 eV and quite reasonable relative accuracy at higher energies.

The desirable new property of PM-DDNN with the parametrically managed activation function of Section 4.2.2.3 is that it damps the interaction potential to zero at large separation distances. This builds physical extrapolation into the results of the neural network. To assess this property for the results obtained by PM-DDNN, we computed $\left|\mathrm{Tr}\left(\mathbf{U}_{\mathrm{AD}}(\mathbf{R})\right)\right|$, and $\left|\mathrm{Tr}\left(\mathbf{U}_{\mathrm{AD}}(\mathbf{R})\right)/\mathrm{Tr}\left(\mathbf{U}^{\mathrm{LD}}(\mathbf{R})\right)\right|$ as functions of the O–O_2 separation distance and the diatomic O_2 distance, where Tr denotes the trace of a matrix. We consider a range of separation distances from 5 to 20 a_0 (corresponding to 2.65 to 10.58 Å) and diatomic O_2 distances from 1 to 7 a_0 (corresponds to 0.53 to 3.70 Å). These quantities are shown in Figure 27.

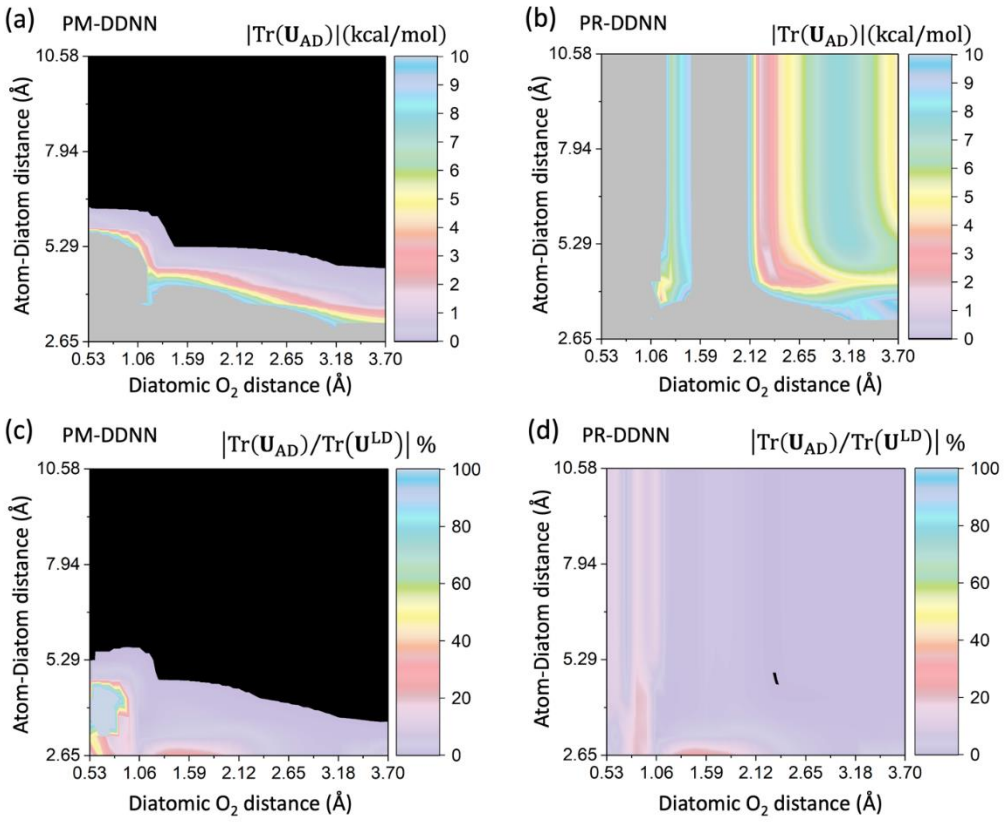

Figure 27: $\left|\mathrm{Tr}\left(\mathbf{U}_{\mathrm{AD}}(\mathbf{R})\right)\right|$ and percentage of $\left|\mathrm{Tr}\left(\mathbf{U}_{\mathrm{AD}}(\mathbf{R})\right)/\mathrm{Tr}\left(\mathbf{U}^{\mathrm{LD}}(\mathbf{R})\right)\right|$ for PM-DDNN and PR-DDNN employed in version 2023 and version 2022 of the 14-state triplet O_3 A´ global potential energy surfaces. The black region in panel a and b is where $\left|\mathrm{Tr}\left(\mathbf{U}_{\mathrm{AD}}(\mathbf{R})\right)\right| < 0.02$ kcal/mol; there is no such region in panel b. Gray regions in panels a and b correspond to $\left(\mathrm{Tr}\left(\mathbf{U}_{\mathrm{AD}}(\mathbf{R})\right) > 10\right.$ kcal/mol. The black regions in panels c and d are the regions with $\left|\mathrm{Tr}\left(\mathbf{U}_{\mathrm{AD}}(\mathbf{R})\right)/\mathrm{Tr}\left(\mathbf{U}^{\mathrm{LD}}(\mathbf{R})\right)\right| < 0.1\%$; this region is very small in panel d, and it should not be confused with a possible tiny fleck of dirt on the screen.

Panels a and b of Figure 27 show $\mathrm{Tr}\left(\mathbf{U}_{\mathrm{AD}}(\mathbf{R})\right)$ for the version-2023 PM-DDNN potential and for the version-2022 PR-DDNN potential, respectively. The black part in panel a and b indicates the region where $\left|\mathrm{Tr}\left(\mathbf{U}_{\mathrm{AD}}(\mathbf{R})\right)\right| < 0.02$ kcal/mol. The gray region in panels a and b corresponds to $\left(\mathrm{Tr}\left(\mathbf{U}_{\mathrm{AD}}(\mathbf{R})\right) > 10\right.$ kcal/mol. One sees that $\mathrm{Tr}\left(\mathbf{U}_{\mathrm{AD}}(\mathbf{R})\right)$ from the PM-DDNN calculation decays very well as a function of the atom–diatom distance (i.e., the subsystem-separation distance). In contrast, for the PR-DDNN surface,

there is no black region. Panels c and d of figure 27 show $\left|\mathrm{Tr}\left(\mathbf{U}_{\mathrm{AD}}(\mathbf{R})\right)/\mathrm{Tr}\left(\mathbf{U}^{\mathrm{LD}}(\mathbf{R})\right)\right|$ for the two surfaces. The black regions in panels c and d indicate the regions with $\left|\mathrm{Tr}\left(\mathbf{U}_{\mathrm{AD}}(\mathbf{R})\right)/\mathrm{Tr}\left(\mathbf{U}^{\mathrm{LD}}(\mathbf{R})\right)\right| < 0.1\%$. We conclude from Figure 27 that PM-DDNN achieves a physical fit at large separation distances, which was the primary objective of the present work.

Table 7: Mean unsigned errors (MUEs in meV) of the adiabatic energies (for both unpermuted and permuted geometries) and number of geometries (N_{geom}) in different energy ranges (E in eV) of the final fit for the 2023 version of the fourteen-state $^3A'$ O_3 system

	$E < 5$		$5 < E < 10$		$10 < E < 20$		$20 < E < 40$		$E > 40$		All	
State	N_{geom}	MUE	N_{geom}	MUE	N_{geom}	MUE	N_{geom}	MUE	N_{geom}	MUE	N_{geom}	MUE
V_1	31956	33	4668	70	1170	137	246	185	0	–	38040	42
V_2	30744	32	5352	66	1638	153	306	184	0	–	38040	43
V_3	29292	34	6318	65	2052	149	378	169	0	–	38040	47
V_4	27822	30	7254	56	2520	197	444	189	0	–	38040	48
V_5	25758	32	8904	59	2778	213	600	218	0	–	38040	54
V_6	23922	31	10428	54	3030	222	660	256	0	–	38040	56
V_7	22080	29	11784	55	3372	202	804	239	0	–	38040	57
V_8	19476	32	13902	56	3762	189	900	238	0	–	38040	61
V_9	11778	42	20628	68	4674	220	954	286	6	116	38040	84
V_{10}	10080	30	21918	61	4950	226	1086	290	6	119	38040	81
V_{11}	8016	31	23532	63	5298	231	1188	311	6	152	38040	87
V_{12}	6606	29	22026	52	7074	176	2328	229	6	269	38040	82
V_{13}	3948	30	24342	61	7008	196	2736	223	6	485	38040	94
V_{14}	3402	31	24462	64	7170	194	3000	250	6	77	38040	100
All	254880	32	205518	60	56496	199	15630	244	36	203	532560	67

In the future, one can explore other strategies. For example, in a triatomic system where one is concerned with managing potential representations in asymptotic regions, one might base the parametrically managed activation function on the second largest interatomic distance (rather than the largest). For another example, in any polyatomic

system where one is concerned with managing potential representations in highly repulsive regions, one might base a parametrically managed activation function on any or all interatomic distances that become very small.

4.4 Conclusions

In this work, we introduced a new step in neural network optimization of molecular potentials. The new step is called a parametrically managed activation function. Adding the parametrically managed activation function to our previously developed PR-DDNN yields a new method called parametrically managed DDNN or PM-DDNN.

The PM-DDNN method can be used to enforce physical behavior in potential functions by employing lower-dimensional potentials in asymptotic regions and/or when two atoms get close. We illustrated the method for the former case by presenting a parametrically managed activation function that is specifically designed to damp interaction potentials toward zero in asymptotic regions – even without placing data there. The parametrically managed activation function depends parametrically on the separation distance of the fragments of the full system. The result is an improved set of 14-state $^3A'$ global potential energy surfaces for $O + O_2$ collisions that shows that the neural network potential can be used safely outside the range of its data. Although the equations in present article were written in the language of a low-dimensional potential, one could also apply this method where the low-dimensional potential is replaced by a lower-level potential with the same dimensionality as the final potential.

We emphasize that the step of using a parametrically managed activation function can also be employed in other neural network architectures and contexts. One of the disadvantages of neural network potentials, as compared to ones designed with more human input, has been that they do not necessarily augment the mathematical steps with underlying human understanding, for example, by choosing a functional form that satisfies the known characters of the potentials. Use of a parametrically managed activation step is one way to add human understanding to a neural network potential without limiting the neural network to a chosen functional form.

Appendix. Improved diatomic potentials

The two-body potentials are the diatomic potential energies at the $O_2(\ ^3\Sigma_g^-)$ + O (^{3}P), $O_2(\ ^3\Delta_u)$ + O (^{3}P), and $O_2(\ ^3\Sigma_u^+)$ + O (^{3}P) asymptotes. Recall that the adiabatic two-body energies are the same as the diabatic two-body energies.

Each diatomic potential $V_m^{\mathrm{PA}}(r_i)$ is separated into short-range (SR) potential and a damped dispersion term[313,314,315] based on the based on the D3(BJ) parameterization:

$$V_m^{\mathrm{PA}}(r_i) = V_m^{\mathrm{SR}}(r_i) + V^{\mathrm{D3(BJ)}}(r_i) \tag{36}$$

The same $V^{\mathrm{D3(BJ)}}(r_i)$ is used for all fourteen states, and it is the same in the 2023 potentials as in the 2022 ones. For $V_m^{\mathrm{SR}}(r_i)$, the 2023 potentials use the same functional form as was used in the 2022 potentials, but we improved the parameters by calculating extra points in the vicinity of the potential minima and adding these points to the diatomic data used for fitting, The SR functional form is an even-tempered Gaussian function:

$$V_m^{\mathrm{SR}} = \begin{cases} \left[\sum_{k=0}^{7} a_{k,m}\exp\left(-\alpha_m\beta_m r_i^2\right)\right] + \left[\varepsilon_m\exp\left(-\delta_m\left(r_i - 1.7\ \text{Å}\right)^2\right)\right] & \text{if } m = 7, 8 \\ \sum_{k=0}^{7} a_{k,m}\exp\left(-\alpha_m\beta_m r_i^2\right) & \text{if } m = 1\text{–}6 \text{ or } 9\text{–}14 \end{cases} \tag{37}$$

The improved coefficients $\alpha_{k,m}$, β_m, ε_m and $\delta_m$are in Tables 8 and 9.

Table 8: Fitted parameters of for *m* = 1 – 2 and *m* = 9-14

	m = 1,2	*m* = 9,10	*m* = 11,12,13	*m* = 14
State	$O_2(\ ^3\Sigma_g^-)+O(^3P)$	$O_2(\ ^1\Sigma_u^-)+O(^3P)$	$O_2(\ ^3\Delta_u)+O(^3P)$	$O_2(\ ^3\Sigma_u^+)+O(^3P)$
α_n, Å^{-2}	0.991088352	0.950046799307d0	1.11399797348271	1.24888948675275
β_n , unitless	1.35561616	1.642688451339d0	1.63184883563828	1.61630730207906
a_0, kcal/mol	1028.27423	-483.125326	-767.018283	-866.519522
a_1, kcal/mol	-10422.5661	956.00518	2893.42549	3532.65087
a_2, kcal/mol	26251.0588	1684.94566	-3964.21584	-2927.82317
a_3, kcal/mol	-35759.8376	2347.10958	32389.5668	23357.3166
a_4, kcal/mol	34535.4087	18401.7933	-203511.939	-113057.808
a_5, kcal/mol	-15442.1054	-49552.6652	2627822.41	1880718.34
a_6, kcal/mol	5100.53268	-367905.919	-68125724.3	-73167704.6
a_7, kcal/mol	15216.8614	47140027.3	4210349180	6245674420

Table 9: Fitted parameters of for m = 3 – 8

	m = 3,4,5	m = 6	m = 7,8
State	$O_2(\ ^1\Delta_g)+O(^3P)$	$O_2(\ ^1\Sigma_g^+)+O(^3P)$	See ref. 290
α_n, Å^{-2}	0.926743129655067	0.859772042751452	2.19185728150371
β_n , unitless	1.49310094503326	1.52376335851761	-2663791.40882274
a_0, kcal/mol	-306.73487963	-191.49156299	4890643.13480523
a_1, kcal/mol	-1390.05533975	-971.3168522	18211797.6008347
a_2, kcal/mol	4128.81576751	2222.1876317	-69478406.8831105
a_3, kcal/mol	-4290.68553855	-885.28321436	88925293.456462
a_4, kcal/mol	11743.6159167	7119.8709632	-48996476.3149754
a_5, kcal/mol	-4286.12400273	2330.45304051	7263885.80760647
a_6, kcal/mol	21029.43435387	14359.28824246	1859624.51906546
a_7, kcal/mol	1807.06950125	10675.50993141	1.05793185102898
$\varepsilon_{7\text{ or }8}$, kcal/mol			15.5242851149696
$\delta_{7\text{ or }8}$, Å^{-2}			39.7454754114259

Bibliography

[249] Hautier, G.; Fischer, C. C.; Jain, A.; Mueller, T.; Ceder, G. Finding Nature's Missing Ternary Oxide Compounds Using Machine Learning and Density Functional Theory. *Chem. Matter.* **2010**, *22*, 3762-3767.

[250] Rupp, M.; Tkatchenko, A.; Müller, K.-R.; von Lilienfeld, O. A. Fast and Accurate Modeling of Molecular Atomization Energies with Machine Learning. *Phys. Rev. Lett.* **2012**, *108*, 058301.

[251] Ramakrishnan, R.; Dral, P. O.; Rupp, M; von Lilienfeld, O. A. Quantum Chemistry Structures and Properties of 134 kilo Molecules. *Sci. Data* **2014**, *1*, 140022.

[252] Shu, Y.; Levine, B. G. Simulated Evolution of Fluorophores for Light Emitting Diodes. *J. Chem. Phys.* **2015**, *142*, 104104.

[253] Rupp, M.; von Lilienfeld, O. A.; Burke, K. Guest Editorial: Special Topic on Data-Enabled Theoretical Chemistry. *J. Chem. Phys.* **2018**, *148*, 241401.

[254] Huang, B.; von Lilienfeld, O. A. Ab Initio Machine Learning in Chemical Compound Space. *Chem. Rev.* **2021**, *121*, 10001-10036.

[255] Duan, C.; Nandy, A.; Kulik, H. J. Machine Learning for the Discovery, Design, and Engineering of Materials. *Annu. Rev. Chem. Biomol. Eng.* **2022**, *13*, 405-429.

[256] Ess, D. H.; Jelfs, K. E.; Kulik, H. J. Chemical Design by Artificial Intelligence. *J. Chem. Phys.* **2022**, *157*, 120401.

[257] Rosen, A. S.; Fung, V.; Huck, P.; O'Donnell, C. T.; Horton, M. K.; Truhlar, D. G.; Persson, K. A.; Notestein, J. M.; Snurr, R. Q. High-Throughput Predictions of Metal–Organic Framework Electronic Properties: Theoretical Challenges, Graph Neural Networks, and Data Exploration. *npj Comput. Mat.* **2022**, *8*, 112.

[258] Terrones, G. G.; Duan, C.; Nandy, A.; Kulik, H. J. Low-Cost Machine Learning Prediction of Excited State Properties of Iridium-Centered Phosphors. *Chem. Sci*. **2023**, *14*, 1419-1433.

[259] Snyder, J. C.; Rupp, M.; Hansen, K.; Blooston, L.; Müller, K.-R.; Burke, K. Orbital-Free Bond Breaking via Machine Learning. *J. Chem. Phys.* **2013**, *139*, 224104.

[260] Ramakrishnan, R.; Dral, P. O.; Rupp, M.; von Lilienfeld, O. A. Big Data Meets Quantum Chemistry Approximations: The Δ-Machine Learning Approach. *J. Chem. Theory Comput.* **2015**, *11*, 2087-2096.

[261] Nagai, R.; Akashi, R.; Sugino, O. Completing Density Functional Theory by Machine Learning Hidden Messages from Molecules. *npj Comput. Mater.* **2020**, *6*, 43.

[262] King, D. S.; Truhlar, D. G.; Gagliardi, L. Machine-Learned Energy Functionals for Strongly Correlated Systems. *J. Phys. Chem. Lett.* **2021**, *12*, 7761-7767.

[263] Houston, P. L.; Nandi, A.; Bowman, J. M. A Machine Learning Approach for Rate Constants. III. Application to the $Cl(^2P) + CH_4 \rightarrow CH_3 + HCl$ Reaction. *J. Phys. Chem. A* **2022**, *126*, 5672-5679.

[264] Blank, T. B.; Brown, S. D.; Calhoun, A. W.; Doren, D. J. Neural Network Models of Potential Energy Surfaces. *J. Chem. Phys.* **1995**, *103*, 4129-4137.

[265] Gassner, H.; Probst, M.; Lauenstein, A.; Hermansson, K. Representation of Intermolecular Potential Functions by Neural Networks. *J. Phys. Chem. A* **1998**, *102*, 4596-4605.

[266] Jiang, B.; Guo, H. Permutation Invariant Polynomial Neural Network Approach to Fitting Potential Energy Surfaces. *J. Chem. Phys.* **2013**, *139*, 054112.

[267] Raff, L. M.; Malshe, M.; Hagan, M.; Doughan, D. I.; Rockley M. G.; Komanduri R. Ab Initio Potential-Energy Surfaces for Complex, Multichannel Systems using Modified Novelty Sampling and Feedforward Neural Networks. *J. Chem. Phys.* **2005**, *122*, 084104.

[268] Behler, J.; Parrinello, M. Generalized Neural-Network Representation of High-Dimensional Potential-Energy Surfaces. *Phys. Rev. Lett.* **2007**,*98, 146401*.

[269] Jiang, B.; Guo, H. Permutation Invariant Polynomial Neural Network Approach to Fitting Potential Energy Surfaces. *J. Chem. Phys.* **2013**, 139, 054112.

[270] Manzhos, S.; Dawes, R.; Carrington T. Neural Network-Based Approaches for Building High Dimensional and Quantum Dynamics-Friendly Potential Energy Surfaces. *Int. J. Quant. Chem.* **2015**, *115*, 1012–1020.

[271] Shao, K.; Chen, J.; Zhao, Z.; Zhang, D. H. Communication: Fitting Potential Energy Surfaces with Fundamental Invariant Neural Network. *J. Chem. Phys.* **2016**, *145*, 071101.

[272] Behler, J. Perspective, Machine Learning Potentials for Atomistic Simulations. *J. Chem. Phys.* **2016**, *145*, 170901.

[273] Zhang, D. H.; Guo, H. Recent Advances in Quantum Dynamics of Bimolecular Reactions. *Annu. Rev. Phys. Chem.* **2016**, *67*, 135-158.

[274] Jiang, B.; Li, J.; Guo, H. Potential Energy Surfaces from High Fidelity Fitting of Ab Initio Points. The Permutation Invariant Polynomial - Neural Network Approach. *Int. Rev. Phys. Chem.* **2016**, *35*, 479-506.

[275] Yao, K.; Herr, J. E.; Parkhill, J. The Many-Body Expansion Combined with Neural Networks. *J. Chem. Phys.* **2017**, *146*, 014106.

[276] Qu, C.; Yu, Q.; Bowman, J. M. Permutationally Invariant Potential Energy Surfaces. *Annu. Rev. Phys. Chem.* **2018**, *69*, 151-175.

[277] Hu, D.; Xie, Y.; Li, X.; Li, L.; Lan, Z. Inclusion of Machine Learning Kernel Ridge Regression Potential Energy Surfaces in On-the-Fly Nonadiabatic Molecular Dynamics Simulation. *J. Phys. Chem. Lett.* **2018**, *9*, 2725-2732.

[278] Guan, Y.; Guo, H.; Yarkony, D. R. Neural Network Based Quasidiabatic Hamiltonians with Symmetry Adaptation and a Correct Description of Conical Intersections. *J. Chem. Phys.* **2019**, *150*, 214101.

[279] Kang, P. -.; Shang, C.; Liu, Z. -.Large-Scale Atomic Simulation Via Machine Learning Potentials Constructed by Global Potential Energy Surface Exploration. *Acc. Chem. Res.* **2020**, *53*, 2119-2129.

[280] Li, J.; Varga, Z.; Truhlar, D. G.; Guo, H. Many-Body Permutationally Invariant Polynomial Neural Network Potential Energy Surface for N_4. *J. Chem. Theory Comput.* **2020**, *16*, 4822-4832.

[281] Koner, D.; Meuwly, M. Permutationally Invariant, Reproducing Kernel-Based Potential Energy Surfaces for Polyatomic Molecules: from Formaldehyde to Acetone. *J. Chem. Theory Comput.* **2020**, *16*, 5474-5484.

[282] Shu, Y.; Trular, D. G. Diabatization by Machine Intelligence. *J. Chem. Theory Comput.* **2020**, *16*, 6456-6464.

[283] Jiang, B.; Li, J.; Guo, H. High-Fidelity Potential Energy Surfaces for Gas-Phase and Gas-Surface Scattering Processes from Machine Learning. *J. Phys. Chem. Lett.* **2020**, *11*, 5120-5131.

[284] Ang, S. J.; Wang, W.; Schwalbe-Koda, D.; Axelrod, S.; Gómez-Bombarelli, R. Active Learning Accelerates Ab Initio Molecular Dynamics on Reactive Energy Surfaces. *Chem* **2021**, *7*, 738-751.

[285] Manzhos, S.; Carrington, T. Neural Network Potential Energy Surfaces for Small Molecules and Reactions. *Chem. Rev.* **2021**, *121*, 10187-10217.

[286] Meuwly, M. Machine Learning for Chemical Reactions. *Chem. Rev.* **2021**, *121*, 10218-10239.

[287] Shu, Y.; Varga, Z.; de Oliveira-Filho, A. G. S.; Truhlar, D. G. Permutationally Restrained Diabatization by Machine Intelligence. *J. Chem. Theory Comput.* **2021**, *17*, 1106-1116.

[288] Lin, Q.; Zhang, L.; Zhang, Y.; Jiang, B. Searching Configurations in Uncertainty Space: Active Learning of High-Dimensional Neural Network Reactive Potentials. *J. Chem. Theory Comput.* **2021**, *17*, 2691-2701.

[289] Varga, Z.; Liu, Y.; Li, J.; Paukku, Y.; Guo, H.; Truhlar, D. G. Potential Energy Surfaces for High-Energy N + O_2 Collisions. *J. Chem. Phys.* **2021**, *154*, 084304.

[290] Ko, T. W.; Finkler, J. A.; Goedecker, S.; Behler, J. A Fourth-Generation High-Dimensional Neural Network Potential with Accurate Electrostatics Including Non-Local Charge Transfer. *Nature Commun.* **2021**, *12*, 398.

[291] Friederich, P.; Häse, F.; Proppe, J.; Aspuru-Guzik, A. Machine-Learned Potentials for Next-Generation Matter Simulations. *Nature Mat.* **2021**, *20*, 750-761.

[292] Varga, Z.; Shu, Y.; Ning, J.; Truhlar, D. G. Diabatic Potential Energy Surfaces and Semiclassical Muti-State Dynamics for Fourteen Coupled $^3A'$ States of O_3. *Electron. Struct.* **2022**, *4*, 047002.

[293] Bai, Y.; Fu, Y.-L.; Wang, G.-R.; Fu, B.; Han, Y.-C. The Full-Dimensional Potential Energy Surface of He_2H^- Using Fundamental Invariant Neural Network Method. *Int. J. Quantum Chem.* **2022**, *122*, e26988.

[294] Houston, P. L.; Qu, C.; Nandi, A.; Conte, R.; Yu, Q.; Bowman, J. M. Permutationally Invariant Polynomial Regression for Energies and Gradients, Using Reverse Differentiation, Achieves Orders of Magnitude Speed-Up with High Precision Compared to Other Machine Learning Methods. *J. Chem. Phys.* **2022**, *156*, 044120.

[295] Nandi, A.; Conte, R.; Qu, C.; Houston, P. L.; Yu, Q.; Bowman, J. M. Quantum Calculations on a new CCSD(T) Machine-Learned Potential Energy Surface Reveal the Leaky Nature of Gas-Phase Trans and Gauche Ethanol Conformers. *J. Chem. Theory Comput.* **2022**, *18*, 5527-5538.

[296] Guo, H.; Zhang, D.; Truhlar, D. G.; Zuo, J. Global Potential Energy Surfaces by Compressed-State Multistate Pair-Density Functional Theory: The Lowest Doublet States Responsible for the $N(^4S_u) + C_2(a\ ^3\Pi_u) \rightarrow CN(X\ ^2\Sigma^+) + C(^3P_g)$ reaction. *J. Chem. Theory Comput.* **2022**, *18*, 7121-7131.

[297] Xu, X.; Li, J. Deciphering Dynamics of the Cl + SiH_4→ H + SiH_3Cl Reaction on a Machine Learning Made Globally Accurate Full-Dimensional Potential Energy Surface. *J. Phys. Chem. A* **2022**, *126*, 6456-6466.

[298] Lu, X.; Shang, C.; Li, L.; Chen, R.; Fu, B.; Xu, X.; Zhang, D. H. Unexpected Steric Hindrance Failure in the Gas Phase F^- + $(CH_3)_3Cl$ S_N2 Reaction. *Nature Commun.* **2022**, *13*, 4427.

[299] Cheng, Z.; Du, J.; Zhang, L.; Ma, J.; Li, W.; Li, S. Building Quantum Mechanics Quality Force Fields of Proteins with the Generalized Energy-Based Fragmentation Approach and Machine Learning. *Phys. Chem. Chem. Phys.* **2022**, *24*, 1326-1337.

[300] Bowman, J. M.; Qu, C.; Conte, R.; Nandi, A.; Houston, P. L.; Yu, Q. Δ-Machine Learned Potential Energy Surfaces and Force Fields. *J. Chem. Theory Comput.* **2023**, *19*, 1-17.

[301] Gokcan, H.; Isayev, O. Learning Molecular Potentials with Neural Networks. *Wiley Interdisc. Rev. Comp. Mol. Sci.* **2022**,*12*, e1564.

[302] Shu, Y.; Varga, Z.; Kanchanakungwankul, S.; Zhang, L.; Truhlar, D. G. Diabatic States of Molecules. *J. Phys. Chem. A* **2022**, *126*, 992-01018.

[303] Andoni, A.; Panigraphy, R.; Valiant, G.; Zhang, L. Learning Polynomials with Neural Networks. *International Conference on Machine Learning*. In *PMLR*, **2014**, 1908-1916.

[304] Glorot, X.; Bordes, A.; Bengio, Y. Deep Sparse Rectifier Neural Networks. *J. Machine Learning Res.* **2011**, *15*, 315-323.

[305] Hendrycks, D.; Gimpel, K. Gaussian Error Linear Units (GELUs). arXiv:1606.08415; 2016. July 8, 2020, https://arxiv.org/abs/1606.08415 (accessed May 17, 2023).

[306] Hochreiter, S.; Bengio, Y.; Frasconi, P.; Schmidhuber, J. Gradient Flow in Recurrent Nets: The Difficulty of Learning Long-Term Dependencies. In A Field Guide to Dynamical Recurrent Neural Networks; Kremer, S. C., Kolen, J. F., Eds.; Wiley-IEEE Press: New York, 2001.

[307] Tikhonov, A. N.; Arsenin, V. Y. *Solutions of Ill-Posed Problems*; John Wiley: New York, 1977.

[308] Braams, B. J.; Bowman, J. M. Permutationally Invariant Potential Energy Surfaces in High Dimensionality. *Int. Rev. Phys. Chem.* **2009**, *28*, 577-606.

[309] Li, Y.; Liu, J.; Li, J.; Zhai, Y.; Yang, J.; Qu, Z.; Li, H. A New Permutation-Symmetry-Adapted Machine Learning Diabatization Procedure and Its Application in MgH_2 system. *J. Chem. Phys.* **2021**, *155*, 214102.

[310] Brown, F. B.; Schwenke, D. W.; Truhlar, D. G. An Ab Initio Potential Energy Surface and Dynamics Calculations for Vibrational Excitation of I_2 by He, *Theor. Chim. Acta* **1985**, *68*, 23-44.

[311] Shu, Y.; Varga, Z.; Jasper, A. W.; Garrett, B. C.; Espinosa-García, J.; Corchado, J. C.; Duchovic, R. J.; Volobuev, Y. L.; Lynch, G. C.; Yang, K. R.; et al. D. G. POTLIB. http://comp.chem.umn.edu/potlib (accessed May 17, 2023).

[312] Duchovic, R. J.; Volobuev, Y. L.; Lynch, G. C.; Truhlar, D. G.; Allison, T. C.; Wanger, A. F.; Garrett, B. C.; Corchado, J. C. POTLIB: A Potential Energy Surface Library for Chemical Systems. *Comput. Phys. Commun.* **2002**, *144*, 169-187.

[313] Grimme, S.; Antony, J.; Ehrlich, S.; Krieg, H. A Consistent an Accurate Ab Initio Parametrization of Density Functional Dispersion Correction (DFT-D) for the 94 Elements H-Pu. *J. Chem. Phys.* **2010**, *132*, 154104.

[314] Grimme, S.; Ehrlich, S.; Goerigk, L. Effect of the Damping Function in Dispersion Corrected Density Finctional Theory. *J. Comput. Chem.* **2011**, *32*, 1456-1465.

[315] Verma, P.; Wang, B.; Fernandez, L. E.; Truhlar, D. G. Physical Molecular Mechanics Method for Damped Dispersion. *J. Phys. Chem. A* **2017**, *121*, 2855-2862.

Chapter 5 Dual-Level Parametrically Managed Neural Network Method for Learning a Potential Energy Surface for Efficient Dynamics

In part from

Bhaumik, S.; Zhang, D.; Shu, Y.; Truhlar, D. G. Dual-Level Parametrically Managed Neural Network Method for Learning a Potential Energy Surface for Efficient Dynamics. (To be Published)

5.1 Introduction

Machine learning is an advancing field with applications in materials discovery, chemical feature tuning, and molecular dynamics.[316-328] Employing a neural network (NN) is very convenient for representing potential energy surfaces for studying chemical reactions in small molecules.[329-365] However, a major drawback for NN potentials is their untrustworthy behavior when used in regions that differ significantly from their training, especially when they are used for extrapolation. For example, NN potentials may behave inaccurately when a molecule is dissociated because it is hard to fill the dissociated space with data. That is, when creating data for training an NN, it is a hard task to saturate regions where one or more interatomic distances are very large because there is infinite space in asymptotic regions. As a consequence, physical behavior is not necessarily maintained in asymptotic regions. Furthermore, when any internuclear distance gets very small, the potential rises steeply, and one might require a large amount of data to ensure a stable fit. But for classical dynamics, it is not necessary for the potential to be quantitatively accurate there; it is simply required that the potential be large enough to make classical trajectories energetically forbidden there. The present article presents a method designed to handle these aspects of potential surface fitting in an efficient manner.

We have previously developed a method called parametrically managed diabatization by deep neural network (PM-DDNN)[366] that uses a parametrically managed activation function (PMAF) to correct the unphysical behavior conventional NN fits in asymptotic regions by decaying the NN fit to a lower-dimensional analytic potential in regions with large interatomic distances. In this way, we obtained an improved set of potential energy surfaces for the 14 lowest $^3A'$ states of O_3, and we showed that the resulting surfaces had satisfactory behavior for calculating O + O_2 collision dynamics. Here we apply a more powerful version of this kind of approach to a larger and more complex system. The new version uses a full-dimensional potential for efficient representation of the potential at both large distances and in the steep repulsive region at small distances.

We apply the new approach to *ortho*-fluorothiophenol (*o*-FTP; see Figure 28). The fluorine atom of *o*-FTP introduces a new issue that does not occur in thiophenol because

the fluorine atom can form a hydrogen bond with the hydrogen atom of the SH group.[367] In this work, we develop a dual-level parametrically managed neural network (DL-PMNN) to represent the ground-electronic-state potential energy surface of *o*-FTP. The treatment uses an energy-dependent and distance-dependent PMAF with a lower-level electronic structure method to guide a higher-level NN fit.

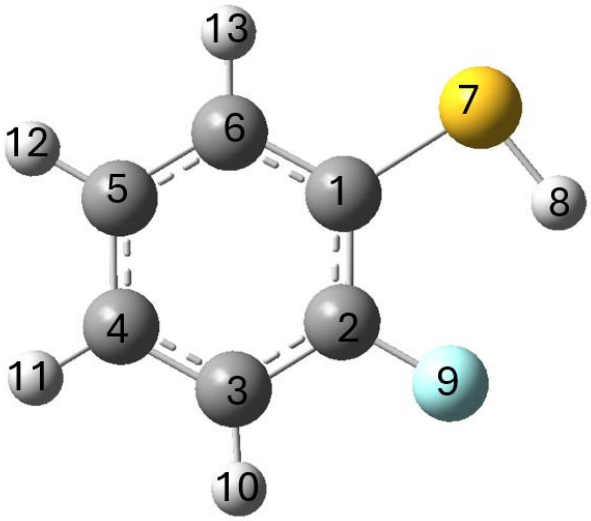

Figure 28: *Ortho*-fluorothiophenol. Color code: grey: carbon, white: hydrogen, yellow: sulfur, green: fluorine. The S7-H8 distance is called the dissociation coordinate, and the C2-C1-S7-H8 dihedral angle is denoted as θ_{CCSH}.

Table 10 defines some symbols and acronyms that will be used in this paper.

Table 10: Definitions

Notation	Definition
V	Potential energy for nuclear motion ≡ electronic energy including nuclear repulsion
ZPE ≡ ε_0	Zero-point vibrational energy
SF	Scale Factor
H_0	Enthalpy at 0 K ≡ V + ZPE
R	*ortho*-fluorothiophenoxyl
H	Hydrogen atom

RH	*ortho*-fluorothiophenol ≡ *o*-FTP
BDE	Bond dissociation energy
D_e	Equilibrium BDE ≡ $V(R_{eq}) + V(H) - V(RH_{eq})$
D_0	Ground-state BDE ≡ $H_0(R_{eq}) + H_0(H) - H_0(RH_{eq})$
HL	Higher level
LL	Lower level
SA	State-averaged
CASSCF	Complete active space self-consistent field
XMS-CASPT2	Extended multi-state complete active space second-order perturbation theory

5.2 Computational Details

All density functional calculations are performed in *Gaussian 16*,[368] except for calculations with the CF22D functional[369] which are performed in *revG16*. The NN training and evaluation is performed in a *Python* script that we implemented using *TensorFlow* (version 2.15.0, build cpu_py311hd3d7757_2 via conda-forge).[370] All dynamics calculations are performed in the *SHARC-MN* semiclassical trajectory program,[371] which is a modified version of the *SHARC* program.[372] We explain some additional details regarding interfacing the NN code later in the paper.

5.3 Choosing two electronic structure methods

Since we are using a dual-level method, we need to validate both an HL electronic structure method and an LL electronic structure method. Our aim is to generate a ground-state potential energy surface of *o*-FTP not only close to the equilibrium geometry, but also in asymptotic and highly repulsive regions. First, we need to choose electronic structure methods that give an accurate enough BDE. Since we lack an experimental value of D_0 for *o*-FTP, we validated the theoretical methods by calculating the D_0 of thiophenol, for which we do have an experimental D_0.

We have calculated the theoretical values of D_0 by

$$D_0 = D_e + \varepsilon_0(\mathrm{R}_{eq}) - \varepsilon_0\left((\mathrm{RH}_{eq})\right) \quad (1)$$

where the subscript *eq* denotes the equilibrium structure of the molecule (RH) or the radical (R). The ZPEs are calculated as scaled harmonic frequencies using the scale-factor method described previously.[373] The scale-factors for every combination of density functional and basis set are given in Table S1.

Both the HL and the LL calculations are performed by unrestricted Kohn-Sham (UKS) calculations.

For the possible choice of HL method, we considered the revM06-L,[374] M06-2X,[375] PW6B95-D3BJ,[376] MN15,[377] and CF22D[378] density functionals and the may-cc-pVTZ,[379,380] may-cc-pV(T+D)Z,[379,381] def2-TZVP,[382,383] and MG3S[384] basis sets. We optimized the geometries of *o*-FTP and *ortho*-fluorothiophenoxyl and calculated D_e and $D_{0;}$ the results are in Table 11. Our D_0 values are in good agreement with previous experimental values[385,386] as shown in Table 12 (left side). Our D_e values agree well with previous computational results[387] as shown in Table 12 (right side).

Table 11: D_0 and D_e (in eV) calculated for the S-H bond of thiophenol using various combinations of density functionals and basis sets

	may-cc-pVTZ		may-cc-pV(T+d)Z		def2-TZVP		MG3S	
	D_0	D_e	D_0	D_e	D_0	D_e	D_0	D_e
revM06-L	3.41	3.65	3.43	3.67	3.41	3.65	3.42	3.65
M06-2X	3.41	3.65	3.43	3.67	3.42	3.65	3.42	3.67
PW6B95-D3(BJ)	3.36	3.59	3.38	3.61	3.37	3.59	3.38	3.61
MN15	3.40	3.63	3.42	3.65	3.40	3.63	3.41	3.64
CF22D	3.44	3.68	3.46	3.70	3.44	3.69	3.44	3.69

Table 12: D_0 (in eV) obtained from experiments (left side) and D_e (in eV) obtained from previous computations (right side)

Experiment	D_0	Previous theroetical[387]	D_e
Velocity map imaging[385]	3.33	M06-2X/aug-cc-pVTZ	3.65
Photofragment translational spectroscopy[386]	≤3.47	MN15/MG3S	3.65
		B3LYP/MG3S	3.63

Table 13 shows a consistent effect (as calculated by all candidate HL methods) of the hydrogen bond on the D_0 and D_e when we compare *o*-FTP to thiophenol. Therefore, we based the choice of HL method on Tables 11 and 12 and on previous comparisons of the functionals on broad databases, which led to the selection of CF22D/may-cc-pVTZ as the HL method.

Table 13: D_0, D_e, ΔD_0, and ΔD_e (in eV) calculated for the S-H bond of o-FTP using various HL methods

	may-cc-pVTZ		may-cc-pV(T+d)Z		def2-TZVP		MG3S	
o-FTP	D_0	D_e	D_0	D_e	D_0	D_e	D_0	D_e
revM06-L	3.45	3.68	3.46	3.70	3.44	3.67	3.45	3.69
M06-2X	3.47	3.71	3.48	3.73	3.46	3.71	3.47	3.73
PW6B95-D3(BJ)	3.42	3.66	3.44	3.67	3.42	3.65	3.44	3.67
MN15	3.46	3.70	3.48	3.71	3.46	3.69	3.47	3.71
CF22D	3.50	3.74	3.52	3.76	3.50	3.74	3.51	3.76
Difference from Thiophenol	ΔD_0	ΔD_e	ΔD_0	ΔD_e	ΔD_0	ΔD_e	ΔD_0	ΔD_e
revM06-L	0.04	0.03	0.03	0.03	0.03	0.02	0.03	0.04
M06-2X	0.06	0.06	0.05	0.06	0.04	0.06	0.05	0.06
PW6B95-D3(BJ)	0.06	0.07	0.06	0.06	0.05	0.04	0.06	0.06
MN15	0.06	0.07	0.06	0.06	0.06	0.06	0.06	0.07
CF22D	0.06	0.06	0.06	0.06	0.06	0.05	0.07	0.07

From a previous study,[388] we have SA(3)-CASSCF(12,11)-XMS-CASPT2/TZVPPD data for the scan of energy as a function of S-H distance. We plot this in Figure 29, which shows that the energy does not rise monotonically as the bond is broken. The interaction energy at 4.5 Å is 0.002 eV lower than that at 5 Å. The energy at 3.0 Å is 0.08 eV above the dissociation limit, indicating a barrier. We use these as features to help us choose an LL method.

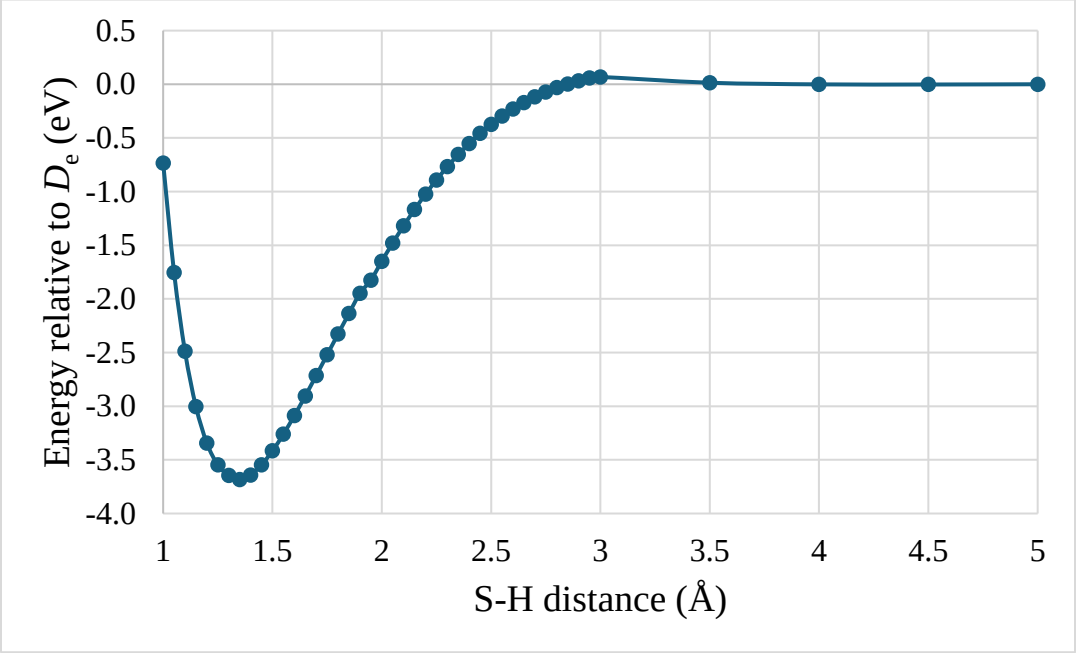

Figure 29: Energy vs S-H distance by SA(3)-CASSCF(12,11)-XMS-CASPT2/TZVPPD calculations.

For the possible choice of lower-level (LL) method, we considered five methods: (i) the MPW1K[389] method with the MIDIY[390] basis set and (ii–v) four semiempirical molecular orbital methods: PM7[391], PM7-D3,[391,392] PM3,[393] and AM1.[394] For each method, we performed a scan along the S-H bond distance in the range 1–5 Å, and we compared D_e, the interaction energy at 4.5 Å, and the barrier determined using a fine scan. We found a barrier for MPW1K/MIDIY at 2.7 Å and a barrier for PM7 at 2.8 Å. For PM3 and AM1,

we didn't observe a negative interaction energy at 4.5 Å and we didn't find any barrier. The PM7 method gave a value of D_e which is 0.27 eV smaller than CF22D/may-cc-pVTZ. It is important for the LL method to be reasonably consistent with the HL method for the PMAF to achieve a smooth transition. Therefore, based upon the results shown in Table 14, we chose the MPW1K/MIDIY method to be the LL.

The ratio of CPU time for a single-point energy calculation with our chosen HL method to the CPU time for a single-point energy calculation with our chosen LL method is a factor of 28.

Table 14: Comparison of energetic features (in eV) of the chosen HL method and of the potential choices of LL method

Method	D_e	Depth at 4.5 Å	Barrier to form S-H bond
CF22D/may-cc-pVTZ	3.80	0.002	0.11
MPW1K/MIDIY	3.76	0.002	0.09
PM7	3.53	0.001	0.10
PM7-D3	3.53	0.002	0.09
PM3	3.60	-	-
AM1	3.59	-	-

5.4 DL-PMNN

5.4.1 Training the DL-PMNN

The goal is to reach HL accuracy for all geometries without making HL calculations in regions where the LL can guide the fit.

We trained and tested the NN on 28880 geometries. To obtain these geometries, we considered 722 combinations of S-H bond distance (Å) and CCSH dihedral angle (°) by combining 38 values of r_{SH} in the range 1-5 Å with 19 values of θ_{CCSH} in the range 0-180 degrees, each spaced by 10 degrees. For each of the 722 selected combinations, we randomly selected 40 coordinates for the other degrees of freedom from the ground-state

Wigner distribution. For 10% of these geometries, we picked an atom at random, and we moved it by 0.2 Å in a random direction. This yields 28880 geometries. We then randomly selected approximately one third of the geometries for testing and used the remaining geometries for training; the actual numbers are 19475 for training and 9405 for testing.

We define E_n^{HL} and E_n^{LL} to be the energies calculated for geometry *n* using the HL and LL methods (CF22D/may-cc-pVTZ for HL and MPW1K/MIDIY for LL) relative to the energy of a nearly dissociated reference configuration where the r_{SH} is 5 Å and the θ_{CCSH} is 0°. We also define

$$\Delta E_n = E_n^{\mathrm{HL}} - E_n^{\mathrm{LL}} \tag{1}$$

and our final surface is defined by

$$E_n^{\mathrm{DL-PMNN}} = \Delta E_n^{\mathrm{DL-PMNN}} + E_n^{\mathrm{LL}} \tag{2}$$

where $\Delta E_n^{\mathrm{DL-PMNN}}$ is an NN fit to ΔE_n.

At geometry *n*, *o*-FTP has 78 interatomic distances $r_{1,n}$, $r_{2,n}$, …, $r_{78,n}$. We define $\Delta r_{i,n}$ and $\Delta r_{\mathrm{max},n}$ as:

$$\Delta r_{i,n} = r_{i,n} - r_{i,eq} \tag{3}$$

$$\Delta r_{\mathrm{max},n} = \max\left(\Delta r_{i,n}\right) \tag{4}$$

where subscript *eq* denotes the equilibrium geometry of *o*-FTP as optimized by CF22D/may-cc-pVTZ. We use one input layer and six hidden layers for the NN. The hidden layers had 512, 256, 128, 64, 32, and 16 nodes. The optimization of the NN is achieved with 120 epochs, a batch size of 256, and the ADAM[395] optimizer. The input layer is $\mathbf{a}^0$, the hidden layers are $\mathbf{a}^1$-$\mathbf{a}^6$. The propagation from the input layer to the sixth hidden layer is done by:

$$\mathbf{a}^{l+1} = g[\mathbf{a}^l\mathbf{w}^{l+1} + \mathbf{b}^{l+1}] \tag{5}$$

where l = 0, 1, …, 5, $\mathbf{w}^{l+1}$ is the connection weight between layers l and l+1, which is a $\omega^l \times \omega^{l+1}$ matrix, where ω^l is the number of nodes in layer l, and $\mathbf{b}^{l+1}$ is the bias of layer l+1; which is a vector of order ω^{l+1}, and g is the ReLU[396] activation function.

The output layer is

$$\mathbf{a}^7 = \mathbf{a}^6\mathbf{w}^7 + \mathbf{b}^7 \tag{6}$$

where $\mathbf{a}^7$ is $N_{\text{train}} \times 1$ matrix, where N_{train} is the number of training geometries Next we use the PMAF denoted by F, which has the shape of a smoothed boxcar window function. This is written as

$$\mathbf{a}^8 = F[\mathbf{a}^7] \tag{7}$$

where $\mathbf{a}^8$ is $N_{\text{train}} \times 1$ matrix whose element n is $\Delta E_n^{\text{DL-PMNN}}$, and

$$F[\mathbf{a}^7] = f_1(\Delta r_{\text{max},n}) f_2(E_n^{\text{LL}}) \mathbf{a}^7 \tag{8}$$

$$f_1(\Delta r_{\text{max},n}) = 0.5 + 0.5 * \tanh\{c(-\Delta r_{\text{max},n} + j)\} \tag{9}$$

$$f_2(E_n^{\text{LL}}) = 0.5 + 0.5 * \tanh\{d(-E_n^{\text{LL}} + k)\} \tag{10}$$

where c, d, j, and k are parameters. Equation 9 takes care of asymptotic regions where two atoms are far away, and eq 10 takes care of regions where the energy gets high due to two atoms being very close. In the last step, the E_n^{LL} is added to $\Delta E_n^{\text{DL-PMNN}}$ to get $E_n^{\text{DL-PMNN}}$. The architecture of our DL-PMNN is compared to a conventional network in Figure 30.

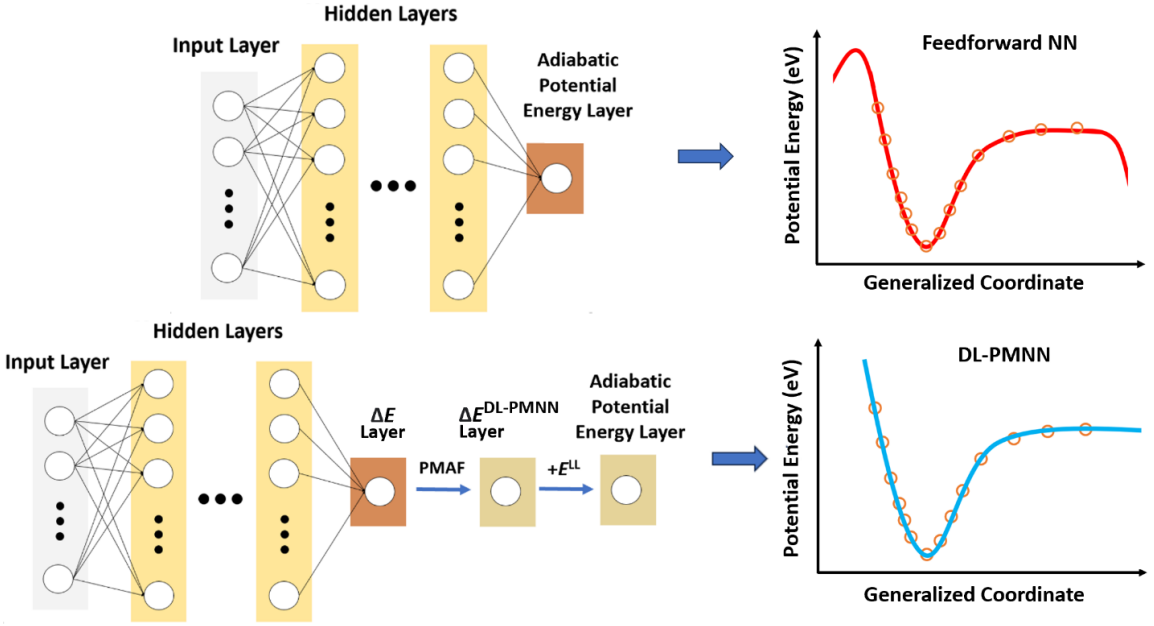

Figure 30: Top left: architecture of feedforward NN. Top Right: schematic potential energy curve generated by a feedforward NN. Bottom left: architecture of DL-PMNN. Bottom right: schematic potential energy curve generated by DL-PMNN. Circles represent training data points. Solid lines represent NN fits. Both NNs are drawn for a single geometry, but the equations in the text are written for N_{train} geometries.

Our PMAF is parametrically dependent on $\Delta r_{\mathrm{max},n}$ and E_n^{LL}; it yields a zero vector when the two subsystems are far away ($\Delta r_{\mathrm{max},n} \gg j$) or very close ($E_n^{\mathrm{LL}} \gg k$):

$$F\left[\boldsymbol{z};\ \Delta r_{\mathrm{max},n}, E_n^{\mathrm{LL}}\right] \rightarrow \begin{cases} \mathbf{1} & \Delta r_{\mathrm{max},n} \ll j \text{ and } E_n^{\mathrm{LL}} \ll k. \\ \mathbf{0} & \Delta r_{\mathrm{max},n} \gg j \text{ or } E_n^{\mathrm{LL}} \gg k \end{cases} \tag{11}$$

Employing the parametrically managed activation function defined by the smoothed boxcar windows in eqs 8–11 produces a fit to the interaction potential that is damped, except when $\Delta r_{\mathrm{max},n} \ll j$ and $E_n^{\mathrm{LL}} \ll k$. The values of *c* and *d* were chosen to make the eq 8 go to the desired limit of eq 10; we chose them as c = 3.0 Å^{-1} and d = 3.0 eV^{-1}. The value of *j* was chosen as 3.7 Å for all internuclear distances; for the S-H distance this corresponds a deviation from the equilibrium distance of 1.3 Å by 3.7 Å. The value of *k* is chosen as 1.3 eV. These parameters make eq 8 go to the desired limit of eq 11.

The loss function of the NN is mean squared error.

5.4.2 Automatic differentiation in DL-PMNN

The trajectory calculations require gradients of the energy. The gradient of $E^{\mathrm{DL-PMNN}}$ with respect to the nuclear coordinates for a given geometry is calculated by the automatic differentiation feature of the *TensorFlow* library. Automatic differentiation in the *TensorFlow* library uses the backpropagation algorithm, which internally constructs a computational graph connecting the input and output quantities. Figure 31 shows the computational graph of calculating $E^{\mathrm{DL-PMNN}}$ from the nuclear Cartesian coordinates **R**. The edges of the graph represent one or more mathematical operations that are available in the *TensorFlow* library. Most parts of the computational graph can be trivially performed using the mathematical operations available in *TensorFlow*, but the edge connecting **R** and E^{LL} (presented in red in Figure 31) is nontrivial because E^{LL} and its gradient are obtained from a density functional calculation in *Gaussian 16*. Therefore, we need a special way to incorporate the energy and the gradient obtained from *Gaussian 16* into the computational graph. In other words, we need to find a sequence of *TensorFlow* mathematical operations

that takes **R** as the input, E^{LL} as the output, and $\frac{\partial E^{\mathrm{LL}}}{\partial \mathbf{R}}$ as the gradient, where E^{LL} and $\frac{\partial E^{\mathrm{LL}}}{\partial \mathbf{R}}$ are obtained from the *Gaussian 16* output.

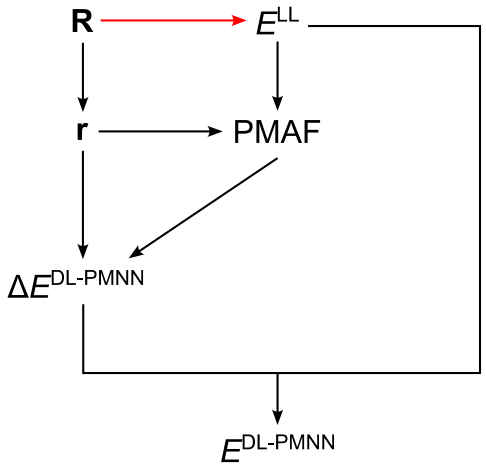

Figure 31: Computational graph showing the forward propagation process of $E^{\mathrm{DL-PMNN}}$ from the nuclear Cartesian coordinates **R**, where **r** denotes the 78 interatomic distances.

We use the following *TensorFlow* code to construct the computational subgraph:

```
e_ll_tensor = tf.tensordot(tf.reshape(R, -1), tf.reshape(grad_ll, -1), 1)
e_ll_tensor += e_ll - tf.stop_gradient(e_ll_tensor)
```

where `R` and `e_ll_tensor` are *TensorFlow* variables representing the input and output of the computational subgraph, while `e_ll` and `grad_ll` are the *TensorFlow* variables containing values of E^{LL} and $\frac{\partial E^{\mathrm{LL}}}{\partial \mathbf{R}}$, respectively. Note that variables `e_ll` and `grad_ll`, as well as the expression `tf.stop_gradient(e_ll_tensor)`, are treated as constants in the computational graph (i.e., the chain rule does not apply to these variables). One can verify that the value of `e_ll_tensor` equals E^{LL} (or `e_ll`), and the gradient of `e_ll_tensor` with respect to `R` equals to $\frac{\partial E^{\mathrm{LL}}}{\partial \mathbf{R}}$ (or `grad_ll`). Therefore, the two lines of *TensorFlow* code represent the edge highlighted in red in Figure 31.

5.5 Methodology for running the trajectories

Geometry optimizations, frequency calculations, initial condition sampling, and trajectory calculations using the DL-PMNN potential generally require several programs to work simultaneously. This subsection explains how we interface several programs in an efficient way. We use trajectory calculations as an example.

The trajectories were carried out with the *SHARC*-MN software. We generated initial conditions for the trajectories by specifying the initial vibration quantum numbers of the normal modes in *SHARC-MN*.[75] The normal mode corresponding to the S-H stretch was assigned quantum number *m*, and all the other normal modes were assigned quantum number 0. The initial rotational quantum numbers of all trajectories were 0.

We start the trajectory calculations by starting the *SHARC-MN* program. At each time step, *SHARC-MN* will generate a geometry and call an external program to calculate the energy and gradient. In the *Gaussian 16* calculations, we use `guess=(read,mix)` while moving from one geometry to another; this option provides a broken-symmetry wave function (unrestricted Kohn-Sham) as an initial guess throughout the entire trajectory. It is especially useful for trajectories that cross the Coulson–Fischer boundary[397] when the S–H bond increase beyond ~1.7 Å; otherwise the self-consistent-field iterations may converge to a higher-energy spin-restricted wave function. However, for geometries near equilibrium, the self-consistent-field iterations converge back to a spin-restricted closed-shell singlet.

In *SHARC-MN* or *SHARC*, a new Linux process must be created at the beginning of each time step and destroyed at the end of each time step. Traditionally, one would implement the interface by directly calling the DL-PMNN *Python* script at each time step to request a new energy and gradient calculation, but we found that the DL-PMNN *Python* script can sometimes be very slow to load on our cluster (i.e., statements such as "`import tensorflow`" can be very slow on a busy cluster), sometimes taking up to a minute when the disk is very busy. It would consequently be very inefficient to create a new instance of the *Python* process at each time step.

To overcome this, we use the setup illustrated in Figure 32 to reduce the overhead to load the *Python* script. At the beginning of the calculation, we simultaneously start the *SHARC-MN* program and the DL-PMNN *Python* script. Once fully loaded, the *Python* script creates and listens to a Unix domain socket, to which another Linux process can connect and send a message to notify the DL-PMNN *Python* script to perform a new energy and gradient calculation. We used a much simpler *Python* script named `send_signal.py` to send the message via the Unix domain socket. The simple script is called at each time step by *SHARC-MN* in place of the full DL-PMNN *Python* script. By using the improved setup, the DL-PMNN *Python* script spent negligible time calculating $E^{\mathrm{DL-PMNN}}$ and its gradient; most of the CPU time is spent on the LL density functional calculation.

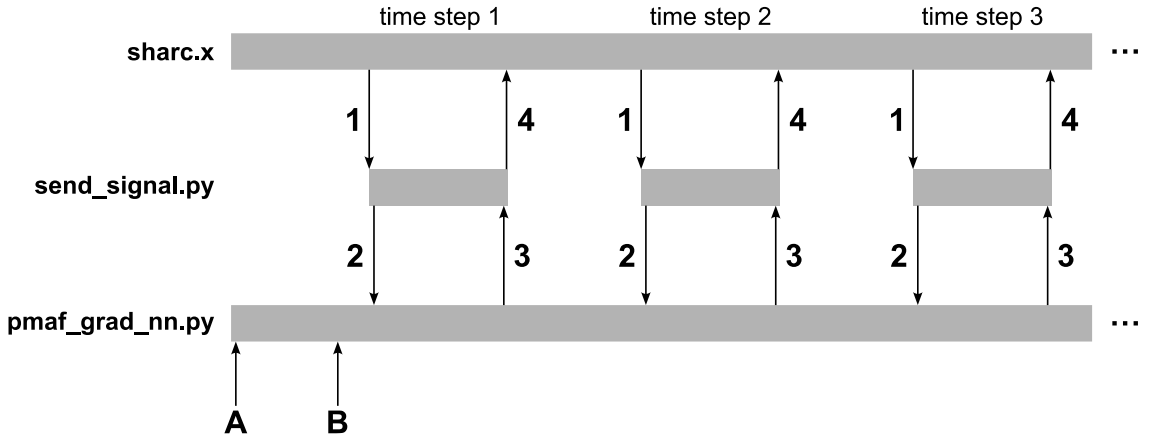

Figure 32: Workflow of *SHARC-MN*–DL-PMNN program interface. **A)** Load DL-PMNN library. **B)** Create and listen to Unix domain socket. **1)** Spawn process at new timestep. **2)** Connect to Unix domain socket and send message to the DL-PMNN *Python* script to request an energy and gradient calculation. **3)** After writing calculated energy and gradient to an output file, terminate and return to the previous process. **4)** Terminate and return to the previous process, read calculated energy and gradient from the output file, and propagate the current time step.

We also performed a similar treatment for geometry optimization and frequency calculations in *Gaussian 16* using the `external` keyword, as well as for initial condition sampling using a *Python* script in *SHARC-MN*. This setup greatly improves the efficiency of these calculations.

5.6 Results

5.6.1 Quality of the fit

We use mean unsigned error (MUE) for analyzing the DL-PMNN errors. This is defined as

$$\mathrm{MUE} = \frac{1}{N}\sum_{n=1}^{N} |E_n^{\mathrm{DL-PMNN}} - E_n^{\mathrm{HL}}| \tag{11}$$

where *N* is the total number of geometries. We did 40 separate optimizations and selected the best NN model based on the lowest mean squared error. For understanding the quality of the fit, we define regions as

A: Geometries where $E_n^{\mathrm{LL}} \ll$1.0 eV and $\Delta r_{\mathrm{max},n} \ll$ 3.4 Å

B: Geometries where $E_n^{\mathrm{LL}} \gg$1.0 eV or $\Delta r_{\mathrm{max},n} \gg$ 3.4 Å

C: Geometries where $E_n^{\mathrm{LL}} \ll$1.3 eV and $\Delta r_{\mathrm{max},n} \ll$ 3.7 Å

D: Geometries where $E_n^{\mathrm{LL}} \gg$1.3 eV or $\Delta r_{\mathrm{max},n} \gg$ 3.7 Å

E: Geometries where $E_n^{\mathrm{LL}} \ll$1.6 eV and $\Delta r_{\mathrm{max},n} \ll$ 4.0 Å

F: Geometries where $E_n^{\mathrm{LL}} \gg$1.6 eV or $\Delta r_{\mathrm{max},n} \gg$ 4.0 Å

G: Geometries where $E_n^{\mathrm{LL}} \ll$1.6 eV

H: Geometries where$E_n^{\mathrm{LL}} \gg$1.6 eV

Tables 15 and 16 give the MUEs for our training and testing datasets. When we consider all geometries, the MUE for the training set is 0.02 eV and for the test set is 0.04 eV. These values are acceptably small, and they correspond to the widely used "chemical accuracy" criterion of 1 kcal/mol, which equals 0.04 eV.

Table 15: Mean unsigned error of DL-PMNN for the training dataset

	All	**A**	**B**	**C**	**D**	**E**	**F**	**G**	**H**
Points	19475	15782	3693	17521	1954	17521	1954	19103	372
MUE	0.02	0.01	0.07	0.02	0.12	0.02	0.21	0.02	0.20

Table 16: Mean unsigned error of DL-PMNN for the testing dataset

	All	**A**	**B**	**C**	**D**	**E**	**F**	**G**	**H**
Points	9405	7822	1583	8649	756	9037	368	9195	210
MUE	0.04	0.03	0.14	0.03	0.21	0.04	0.28	0.04	0.28

Table 15 shows that the training-set MUEs in regions **F** and **H** are 0.21 eV and 0.20 eV respectively. As could have been anticipated by the design of the method, those values are close to the mean of $E_n^{\mathrm{LL}} - E_n^{\mathrm{HL}}$ in those regions, in both of which it is 0.22 eV. Similarly, Table 16 shows that the testing-set MUEs in regions **F** and **H** are 0.28 eV, which are close to the mean of $E_n^{\mathrm{LL}} - E_n^{\mathrm{HL}}$ in those regions, which is 0.30 eV. These comparisons tell us that the PMAF is working well.

5.6.2 Computational Cost

We used two procedures to speed up the calculations; (1) We used a more efficient interface based on Unix domain sockets as described earlier. (2) We used `Pop=none` to turn off population analysis and `Integral(Grid=Fine)` to use a coarser grid in our *Gaussian 16* calculations to reduce the computational cost.

We provide the timings for a representative trajectory in Table 17. The geometry used in this trajectory is sampled near the ground-state minimum of *o*-FTP. The time step is 0.1 fs and we used the velocity Verlet integrator with a fixed time step. We let the trajectories run for 250 fs. Table 17 shows that our speedup procedures, taken together, increased the speed by a factor of 2.6.

Table 17: Average time per step (wall clock time in s) for a representative trajectory

	time for DL-PMNN	time for *Gaussian 16*
Without the two speedup procedures	8.0	40
Using procedure 1	0.5	40
Using procedures 1 and 2	0.5	18

5.6.3 Trajectories

The zero of energy is the reference configuration specified in section 2.2. We did a set of 100 trajectories with m = 17 (17 quanta in the S-H stretch normal mode) and total energy (internal energy of the radical plus relative translational energy) equal to 4.705 eV and a second set of 100 trajectories with m = 11 and total energy of 2.539 eV. We defined the dissociation time as the time at which the S-H bond length reaches 7.0 Å.

For the m = 17 trajectories, all trajectories dissociated, with an average dissociation lifetime of 29.3 fs. All trajectories conserved energy within 0.23 eV; 88 out of 100 trajectories conserved energy within 0.10 eV. Figure 33 shows the energy conservation in two representative trajectories.

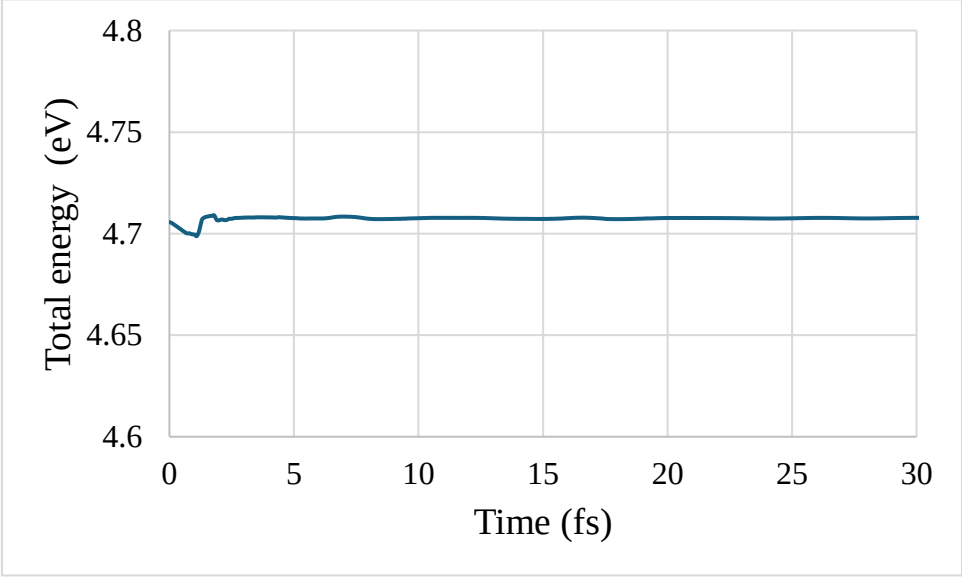

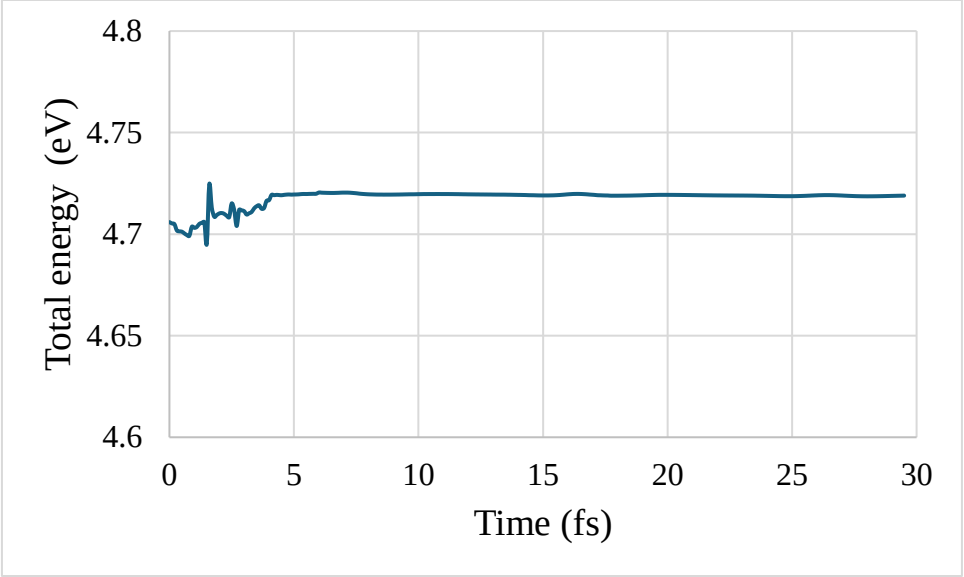

Figure 33: Energy conservation for two representative trajectories for the case of 17 quanta in the S-H stretch normal mode with all other normal modes in their zero-point level. (top) Trajectory 2 (dissociation lifetime is 30.1 fs, and energy is conserved within 0.01 eV). (bottom) Trajectory 56 (dissociation lifetime is 29.5 fs, and energy is conserved within 0.03 eV).

For the m = 11 trajectories, we again found that all trajectories dissociated, with an average dissociation lifetime of 117 fs. All trajectories conserved energy within 0.15 eV; 98 out of 100 trajectories conserved energy within 0.10 eV. Figure 34 shows the energy conservation of two representative trajectories.

These tests demonstrate that the method can be used for trajectories without crashes and with reasonable energy conservation even when dissociation occurs.

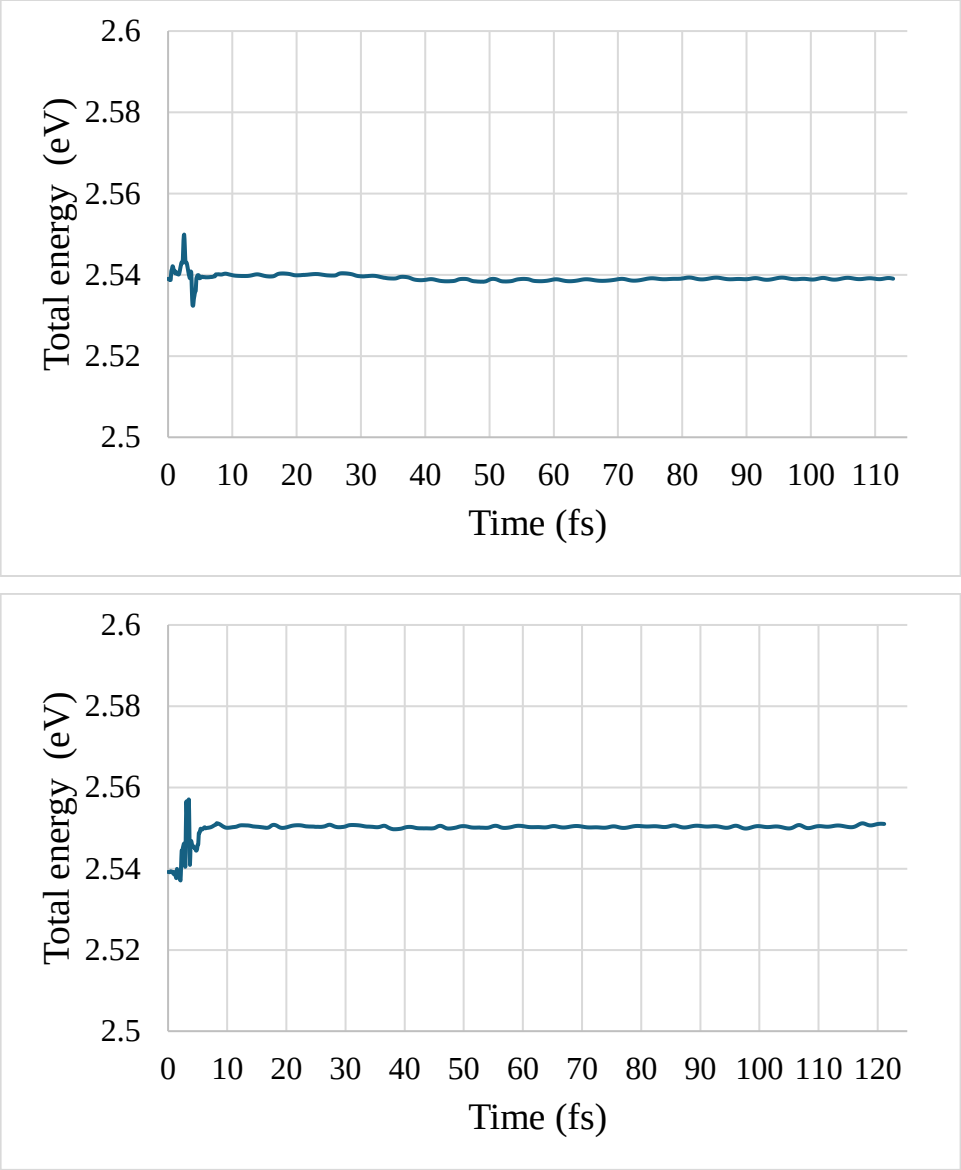

Figure 34: Energy conservation for two representative trajectories for the case of 11 quanta in the S-H stretch normal mode with all other normal modes in their zero-point level. (top) Trajectory 34 with a dissociation lifetime of 112.8 fs and energy conserved within 0.02 eV. (bottom) Trajectory 94 with a dissociation lifetime of 121.1 fs and energy conserved within 0.02 eV.

5.7 Concluding Remarks

In this article, we present a new method for fitting potential energy surfaces. The method, called DL-PMNN, is a dual level Δ-learning method that has the advantage of the

low computational cost of a low-level density functional calculation, while having the high accuracy of a high-level density functional. The method uses a PMAF, which is used to preserve the physical shape of the steep repulsive wall and the flat asymptotic region.

We used the method to fit an accurate potential energy surface of *ortho*-fluorothiophenol. We implemented the gradient of the potential energy surface for DL-PMNN using automatic differentiation by constructing a computational graph in *TensorFlow*. In addition, through Unix domain socket programming and proper keyword usage in *Gaussian 16*, we were able to speed up the calculations of our DL-PMNN by a factor of 2.6.

We observed good conservation of energy for trajectories initiated far from equilibrium regions. The trajectories that started with 17 quanta in the S-H stretch normal mode and with all other modes having ZPE dissociated with an average dissociation time of 29.3 fs. The trajectories that started with 11 quanta in S-H stretch normal mode and all other modes having ZPE dissociated with an average dissociation time of 117 fs.

5.8 Supporting Information

Scale Factors

Table S1: Scale factors for all the combinations of methods and basis sets

	may-cc-pVTZ	may-cc-pV(T+d)Z	def2-TZVP	MG3S
revM06-L	0.974	0.974	0.972	0.970
M06-2X	0.971	0.971	0.971	0.981
PW6B95-D3(BJ)	0.973	0.973	0.974	0.972
MN15	0.975	0.975	0.976	0.975
CF22D	0.983	0.983	0.986	0.983

The scale factors used here are parametrized to give improved vibrational zero-point energies. Scale factors in red were determined using the reduced scale factor optimization model of Alecu et al.[398] Scale factors in black were obtained from

Database of Frequency Scale Factors for Electronic Model Chemistries

(https://comp.chem.umn.edu/freqscale/index.html).

Bibliography

[316] Rupp, M.; Tkatchenko, A.; Müller, K.-R.; von Lilienfeld, O. A. Fast and Accurate Modeling of Molecular Atomization Energies with Machine Learning. *Phys. Rev. Lett.* **2012**, *108*, 058301.

[317] Ramakrishnan, R.; Dral, P. O.; Rupp, M; von Lilienfeld, O. A. Quantum Chemistry Structures and Properties of 134 kilo Molecules. *Scientific Data* **2014**, *1*, 140022.

[318] Shu, Y.; Levine, B. G. Simulated Evolution of Fluorophores for Light Emitting Diodes. *J. Chem. Phys.* **2015**, *142*, 104104.

[319] Rupp, M.; von Lilienfeld, O. A.; Burke, K. Guest Editorial: Special Topic on Data-Enabled Theoretical Chemistry. *J. Chem. Phys.* **2018**, *148*, 241401.

[320] Huang, B.; von Lilienfeld, O. A. Ab Initio Machine Learning in Chemical Compound Space. *Chem. Rev.* **2021**, *121*, 10001-10036.

[321] Duan, C.; Nandy, A.; Kulik, H. J. Machine Learning for the Discovery, Design, and Engineering of Materials. *Annu. Rev. Chem. Biomol. Eng.* **2022**, *13*, 405-429.

[322] Ess, D. H.; Jelfs, K. E.; Kulik, H. J. Chemical Design by Artificial Intelligence. *J. Chem. Phys.* **2022**, *157*, 120401.

[323] Rosen, A. S.; Fung, V.; Huck, P.; O'Donnell, C. T.; Horton, M. K.; Truhlar, D. G.; Persson, K. A.; Notestein, J. M.; Snurr, R. Q. High-Throughput Predictions of Metal–Organic Framework Electronic Properties: Theoretical Challenges, Graph Neural Networks, and Data Exploration. *npj Comput. Mat.* **2022**, *8*, 112.

[324] Terrones, G. G.; Duan, C.; Nandy, A.; Kulik, H. J. Low-Cost Machine Learning Prediction of Excited State Properties of Iridium-Centered Phosphors. *Chem. Sci*. **2023**, *14*, 1419-1433.

[325] Snyder, J. C.; Rupp, M.; Hansen, K.; Blooston, L.; Müller, K.-R.; Burke, K. Orbital-Free Bond Breaking via Machine Learning. *J. Chem. Phys.* **2013**, *139*, 224104.

[326] Ramakrishnan, R.; Dral, P. O.; Rupp, M.; von Lilienfeld, O. A. Big Data Meets Quantum Chemistry Approximations: The Δ-Machine Learning Approach. *J. Chem. Theory Comput.* **2015**, *11*, 2087-2096.

[327] Nagai, R.; Akashi, R.; Sugino, O. Completing Density Functional Theory by Machine Learning Hidden Messages from Molecules. *npj Comput. Mater.* **2020**, *6*, 43.

[328] King, D. S.; Truhlar, D. G.; Gagliardi, L. Machine-Learned Energy Functionals for Strongly Correlated Systems. *J. Phys. Chem. Lett.* **2021**, *12*, 7761-7767.

[329] Gassner, H.; Probst, M.; Lauenstein, A.; Hermansson, K. Representation of Intermolecular Potential Functions by Neural Networks. *J. Phys. Chem. A* **1998**, *102*, 4596-4605.

[330] Jiang, B.; Guo, H. Permutation Invariant Polynomial Neural Network Approach to Fitting Potential Energy Surfaces. *J. Chem. Phys.* **2013**, *139*, 054112.

[331] Raff, L. M.; Malshe, M.; Hagan, M.; Doughan, D. I.; Rockley M. G.; Komanduri R. Ab Initio Potential-Energy Surfaces for Complex, Multichannel Systems Using Modified Novelty Sampling and Feedforward Neural Networks. *J. Chem. Phys.* **2005**, *122*, 084104.

[332] Behler, J.; Parrinello, M. Generalized Neural-Network Representation of High-Dimensional Potential-Energy Surfaces. *Phys. Rev. Lett.* **2007**, *98*, *146401*.

[333] Jiang, B.; Guo, H. Permutation Invariant Polynomial Neural Network Approach to Fitting Potential Energy Surfaces. *J. Chem. Phys.* **2013**, *139*, 054112.

[334] Manzhos, S.; Dawes, R.; Carrington T. Neural Network-Based Approaches for Building High Dimensional and Quantum Dynamics-Friendly Potential Energy Surfaces. *Int. J. Quant. Chem.* **2015**, *115*, 1012–1020.

[335] Shao, K.; Chen, J.; Zhao, Z.; Zhang, D. H. Communication: Fitting Potential Energy Surfaces with Fundamental Invariant Neural Network. *J. Chem. Phys.* **2016**, *145*, 071101.

[336] Behler, J. Perspective, Machine Learning Potentials for Atomistic Simulations. *J. Chem. Phys.* **2016**, *145*, 170901.

[337] Zhang, D. H.; Guo, H. Recent Advances in Quantum Dynamics of Bimolecular Reactions. *Annu. Rev. Phys. Chem.* **2016**, *67*, 135-158.

[338] Jiang, B.; Li, J.; Guo, H. Potential Energy Surfaces from High Fidelity Fitting of Ab Initio Points. The Permutation Invariant Polynomial - Neural Network Approach. *Int. Rev. Phys. Chem.* **2016**, *35*, 479-506.

[339] Yao, K.; Herr, J. E.; Parkhill, J. The Many-Body Expansion Combined with Neural Networks. *J. Chem. Phys.* **2017**, *146*, 014106.

[340] Qu, C.; Yu, Q.; Bowman, J. M. Permutationally Invariant Potential Energy Surfaces. *Annu. Rev. Phys. Chem.* **2018**, *69*, 151-175.

[341] Hu, D.; Xie, Y.; Li, X.; Li, L.; Lan, Z. Inclusion of Machine Learning Kernel Ridge Regression Potential Energy Surfaces in On-the-Fly Nonadiabatic Molecular Dynamics Simulation. *J. Phys. Chem. Lett.* **2018**, *9*, 2725-2732.

[342] Guan, Y.; Guo, H.; Yarkony, D. R. Neural Network Based Quasidiabatic Hamiltonians with Symmetry Adaptation and a Correct Description of Conical Intersections. *J. Chem. Phys.* **2019**, *150*, 214101.

[343] Kang, P.-L.; Shang, C.; Liu, Z.-P.Large-Scale Atomic Simulation Via Machine Learning Potentials Constructed by Global Potential Energy Surface Exploration. *Acc. Chem. Res.* **2020**, *53*, 2119-2129.

[344] Li, J.; Varga, Z.; Truhlar, D. G.; Guo, H. Many-Body Permutationally Invariant Polynomial Neural Network Potential Energy Surface for N_4. *J. Chem. Theory Comput.* **2020**, *16*, 4822-4832.

[345] Koner, D.; Meuwly, M. Permutationally Invariant, Reproducing Kernel-Based Potential Energy Surfaces for Polyatomic Molecules: from Formaldehyde to Acetone. *J. Chem. Theory Comput.* **2020**, *16*, 5474-5484.

[346] Shu, Y.; Truhlar, D. G. Diabatization by Machine Intelligence. *J. Chem. Theory Comput.* **2020**, *16*, 6456-6464.

[347] Jiang, B.; Li, J.; Guo, H. High-Fidelity Potential Energy Surfaces for Gas-Phase and Gas-Surface Scattering Processes from Machine Learning. *J. Phys. Chem. Lett.* **2020**, *11*, 5120-5131.

[348] Ang, S. J.; Wang, W.; Schwalbe-Koda, D.; Axelrod, S.; Gómez-Bombarelli, R. Active Learning Accelerates Ab Initio Molecular Dynamics on Reactive Energy Surfaces. *Chem* **2021**, *7*, 738-751.

[349] Manzhos, S.; Carrington, T. Neural Network Potential Energy Surfaces for Small Molecules and Reactions. *Chem. Rev.* **2021**, *121*, 10187-10217.
[350] Meuwly, M. Machine Learning for Chemical Reactions. *Chem. Rev.* **2021**, *121*, 10218-10239.
[351] Shu, Y.; Varga, Z.; de Oliveira-Filho, A. G. S.; Truhlar, D. G. Permutationally Restrained Diabatization by Machine Intelligence. *J. Chem. Theory Comput.* **2021**, *17*, 1106-1116.
[352] Lin, Q.; Zhang, L.; Zhang, Y.; Jiang, B. Searching Configurations in Uncertainty Space: Active Learning of High-Dimensional Neural Network Reactive Potentials. *J. Chem. Theory Comput.* **2021**, *17*, 2691-2701.
[353] Varga, Z.; Liu, Y.; Li, J.; Paukku, Y.; Guo, H.; Truhlar, D. G. Potential Energy Surfaces for High-Energy N + O_2 Collisions. *J. Chem. Phys.* **2021**, *154*, 084304.
[354] Ko, T. W.; Finkler, J. A.; Goedecker, S.; Behler, J. A Fourth-Generation High-Dimensional Neural Network Potential with Accurate Electrostatics Including Non-Local Charge Transfer. *Nature Commun.* **2021**, *12*, 398.
[355] Friederich, P.; Häse, F.; Proppe, J.; Aspuru-Guzik, A. Machine-Learned Potentials for Next-Generation Matter Simulations. *Nature Mat.* **2021**, *20*, 750-761.
[356] Varga, Z.; Shu, Y.; Ning, J.; Truhlar, D. G. Diabatic Potential Energy Surfaces and Semiclassical Muti-State Dynamics for Fourteen Coupled $^3A´$ States of O_3. *Electron. Struct.* **2022**, *4*, 047002.
[357] Bai, Y.; Fu, Y.-L.; Wang, G.-R.; Fu, B.; Han, Y.-C. The Full-Dimensional Potential Energy Surface of He_2H^- Using Fundamental Invariant Neural Network Method. *Int. J. Quantum Chem.* **2022**, *122*, e26988.
[358] Houston, P. L.; Qu, C.; Nandi, A.; Conte, R.; Yu, Q.; Bowman, J. M. Permutationally Invariant Polynomial Regression for Energies and Gradients, Using Reverse Differentiation, Achieves Orders of Magnitude Speed-Up with High Precision Compared to Other Machine Learning Methods. *J. Chem. Phys.* **2022**, *156*, 044120.
[359] Nandi, A.; Conte, R.; Qu, C.; Houston, P. L.; Yu, Q.; Bowman, J. M. Quantum Calculations on a new CCSD(T) Machine-Learned Potential Energy Surface Reveal the Leaky Nature of Gas-Phase Trans and Gauche Ethanol Conformers. *J. Chem. Theory Comput.* **2022**, *18*, 5527-5538.
[360] Guo, H.; Zhang, D.; Truhlar, D. G.; Zuo, J. Global Potential Energy Surfaces by Compressed-State Multistate Pair-Density Functional Theory: The Lowest Doublet States Responsible for the N(^4S_u) + C2($a\ ^3\Pi_u$) → CN($X\ ^2\Sigma^+$) + C(^3P_g) reaction. *J. Chem. Theory Comput.* **2022**, *18*, 7121-7131.
[361] Xu, X.; Li, J. Deciphering Dynamics of the Cl + SiH_4→ H + SiH_3Cl Reaction on a Machine Learning Made Globally Accurate Full-Dimensional Potential Energy Surface. *J. Phys. Chem. A* **2022**, *126*, 6456-6466.
[362] Lu, X.; Shang, C.; Li, L.; Chen, R.; Fu, B.; Xu, X.; Zhang, D. H. Unexpected Steric Hindrance Failure in the Gas Phase F^- + $(CH_3)_3CI$ S_N2 Reaction. *Nature Comm.* **2022**, *13*, 4427.
[363] Cheng, Z.; Du, J.; Zhang, L.; Ma, J.; Li, W.; Li, S. Building Quantum Mechanics Quality Force Fields of Proteins with the Generalized Energy-Based Fragmentation Approach and Machine Learning. *Phys. Chem. Chem. Phys.* **2022**, *24*, 1326-1337.

[364] Bowman, J. M.; Qu, C.; Conte, R.; Nandi, A.; Houston, P. L.; Yu, Q. Δ-Machine Learned Potential Energy Surfaces and Force Fields. *J. Chem. Theory Comput.* **2023**, *19*, 1-17.

[365] Andoni, A.; Panigraphy, R.; Valiant, G.; Zhang, L. Learning Polynomials with Neural Networks. In *International Conference on Machine Learning*; Proceedings of Machine Learning Research (PMLR): 2014; pp. 1908-1916.

[366] Akher, F.B.; Shu, Y.; Varga, Z.; Bhaumik, S.; Truhlar, D.G. Parametrically Managed Activation Function for Managing the Behavior of a Neural Network Potential with a Low-Dimensional Potential. *J. Phys. Chem. A* **2023**, *127*, 5287-5297.

[367] Han, S.; You, H. S.; Kim, S. Y.; Kim, S. K. Dynamic Role of Intermolecular Hydrogen Bonding in Nonadiabatic Chemistry Revealed in the UV Photodissociation Reactions of 2-Fluorothiophenol and 2-Chlorothiophenol. *J. Phys. Chem. A* **2014**, *118*, 6940−6949.

[368] Frisch, M. J.; Trucks, G. W.; Schlegel, H. B.; Scuseria, G. E.; Robb, M. A.; Cheeseman, J. R.; Scalmani, G.; Barone, V.; Petersson, G. A.; Nakatsuji, H.; Li, X.; Caricato, M.; Marenich, A. V.; Bloino, J.; Janesko, B. G.; Gomperts, R.; Mennucci, B.; Hratchian, H. P.; Ortiz, J.V.; Izmaylov, A. F.; Sonnenberg, J. L.; Williams-Young, D.; Ding, F.; Lipparini, F.; Egidi, F.; Goings, J.; Peng, B.; Petrone, A.; Henderson, T.; Ranasinghe, D.; Zakrzewski, V. G.; Gao, J.; Rega, N.; Zheng, G.; Liang, W.; Hada, M.; Ehara, M.; Toyota, K.; Fukuda, R.; Hasegawa, J.; Ishida, M.; Nakajima, T.; Honda, Y.; Kitao, O.; Nakai, H.; Vreven, T.; Throssell, K.; Montgomery, J. A.; Jr.; Peralta, J. E.; Ogliaro, F.; Bearpark, M. J.; Heyd, J. J.; Brothers, E. N.; Kudin, K. N.; Staroverov, V. N.; Keith, T. A.; Kobayashi, R.; Normand, J.; Raghavachari, K.; Rendell, A. P.; Burant, J. C.; Iyengar, S. S.; Tomasi, J.; Cossi, M.; Millam, J. M.; Klene, M.; Adamo, C.; Cammi, R.; Ochterski, J. W.; Martin, R. L.; Morokuma, K.; Farkas, O.; Foresman, J. B.; Fox, D. J. *Gaussian 16*, Revision C.01; Gaussian, Inc.: Wallingford CT, 2016.

[369] Liu, Y.; Zhang, C.; Liu, Z.; Truhlar, D. G.; Wang, Y.; He, X. Supervised Learning of a Chemistry Functional with Damped Dispersion. *Nat. Comput. Sci.* **2023** *3*, 48-58.

[370] Abadi, M.; Agarwal, A.; Barham, P.; Brevdo, E.; Chen, Z.; Citro, C.; Corrado, G. S.; Davis, A.; Dean, J.; Devin, M.; Ghemawat, S.; Goodfellow, I.; Harp, A.; Irving, G.; Isard, M.; Jozefowicz, R.; Jia, Y.; Kaiser, L.; Kudlur, M.; Levenberg, J.; Mané, D.; Schuster, M.; Monga, R.; Moore, S.; Murray, D.; Olah, C.; Shlens, J.; Steiner, B.; Sutskever, I.; Talwar, K.; Tucker, P.; Vanhoucke, V.; Vasudevan, V.; Viégas, F.; Vinyals, O.; Warden, P.; Wattenberg, M.; Wicke, M.; Yu, Y.; Zheng, X. *TensorFlow: Large-scale machine learning on heterogeneous systems*; 2015.

[371] Shu, Y.; Zhang, L.; Truhlar, D. G. SHARC-MN v3.1; CERN, Zenodo, 2024. DOI: 10.5281/zenodo.13899676. (accessed November 13, 2024)

[372] Mai, S.; Avagliano, D.; Heindl, M.; Marquetand, P.; Menger, F. S. J.; Oppel, M.; Plasser, F.; Polonius, S.; Ruckenbauer, M.; Shu, Y.; Truhlar, D. G.; Zhang, L.; Zobel, P.; González, L. SHARC release 3.0.2; González Group: Wien, 2024. https://sharc-md.org (accessed May 13, 2024).

[373] Alecu, I. M.; Zheng, J.; Zhao, Y.; Truhlar, D. G. Computational Thermochemistry: Scale Factor Databases and Scale Factors for Vibrational Frequencies Obtained from Electronic Model Chemistries. *J. Chem. Theory Comput.* **2010**, *6*, 2872−2887.

[374] Wang, Y.; Jin, X.; Yu, H. S.; Truhlar, D. G.; He, X. Revised M06-L Functional for Improved Accuracy on Chemical Reaction Barrier Heights, Noncovalent Interactions, and Solid-State Physics. *Proc. Nat. Acad. Sci. US* **2017,** *114*, 8487-8492.

[375] Zhao, Y.; Truhlar, D. G. The M06 Suite of Density Functionals for Main Group Thermochemistry, Thermochemical Kinetics, Noncovalent Interactions, Excited States, and Transition Elements: Two New Functionals and Systematic Testing of Four M06-Class Functionals and 12 Other Functionals. *Theor. Chem. Acc.* **2008,** *120*, 215-241.

[376] Zhao, Y.; Truhlar, D. G. Design of Density Functionals that are Broadly Accurate for Thermochemistry, Thermochemical Kinetics, and Nonbonded Interactions. *J. Phys. Chem. A*, **2005**, *109*, 5656-5667.

[377] Yu, H. S.; He, X.; Li, S. L.; Truhlar, D. G. MN15: A Kohn–Sham Global-Hybrid Exchange–Correlation Density Functional with Broad Accuracy for Multi-Reference and Single-Reference Systems and Noncovalent Interactions. *Chem. Sci.* **2016**, *7*, 5032-5051.

[378] Liu, Y.; Zhang, C.; Liu, Z.; Truhlar, D. G.; Wang, Y.; He, X. Supervised Learning of a Chemistry Functional with Damped Dispersion. *Nat. Comput. Sci.* **2023** *3*, 48-58.

[379] Papajak, E.; Leverentz, H. R.; Zheng, J.; Truhlar, D. G. Efficient Diffuse Basis Sets: cc-pVxZ+ and maug-cc-pVxZ. *J. Chem. Theory Comput*. **2009**, *5*, 1197−1202.

[380] Dunning, T. H. Jr. Gaussian Basis Sets for Use in Correlated Molecular Calculations. I. The Atoms Boron Through Neon and Hydrogen. *J. Chem. Phys.* **1989**, *90*, 1007−1023.

[381] Dunning T.H. Jr.; Peterson K.A.; Wilson A.K. Gaussian Basis Sets for Use in Correlated Molecular Calculations. X. The Atoms Aluminum Through Argon Revisited. *J. Chem. Phys.* **2001**, 114, 9244 – 9253.

[382] Weigend, F.; Ahlrichs, R. Balanced Basis Sets of Split Valence, Triple Zeta Valence and Quadruple Zeta Valence Quality for H to Rn: Design and Assessment of Accuracy. *Phys. Chem. Chem. Phys.* **2005**, *7*, 3297-3305.

[383] Weigend, F. Accurate Coulomb-Fitting Basis Sets for H to Rn. *Phys. Chem. Chem. Phys.* **2006**, *8*, 1057-1065.

[384] Fast, P. L.; Sanchez, M. L.; Truhlar, D. G. Multi-Coefficient Gaussian-3 Method for Calculating Potential Energy Surfaces *Chem. Phys. Lett.***1999**, *306*, 407-410.

[385] Lim, I. S.; Lim, J. S.; Lee, Y. S.; Kim, S. K. Experimental and Theoretical Study of the Photodissociation Reaction of Thiophenol at 243 nm: Intramolecular Orbital Alignment of the Phenylthiyl Radical. *J. Chem. Phys.* **2007** *126*.

[386] Devine, A. L.; Nix, M. G.; Dixon, R. N.; Ashfold, M. N. Near-Ultraviolet Photodissociation of Thiophenol. *J. Phys. Chem. A* **2008** *112*, 9563-9574.

[387] Zhang, L.; Truhlar, D. G. Sun, S. Correction: Electronic Spectrum and Characterization of Diabatic Potential Energy Surfaces for Thiophenol. *Phys. Chem. Chem. Phys.* **2019** *21*, 8179-8179.

[388] Ning, J.; Truhlar, D. G. Electronic Excitation of *ortho*-Fluorothiophenol. *J. Phys. Chem. A* **2023,** *127*, 1469-1474.

[389] Lynch, B. J.; Fast, P. L.; Harris, M.; Truhlar, D. G. Adiabatic Connection for Kinetics. *J. Phys. Chem. A* **2000**, *104*, 4811-4815.

[390] Easton, R. E.; Giesen, D. J.; Welch, A.; Cramer, C. J.; Truhlar, D. G. The MIDI! Basis Set for Quantum Mechanical Calculations of Molecular Geometries and Partial Charges. *Theor. Chim. Acta* **1996**, *93*, 281-301.

[391] Stewart, J. J. P. Optimization of Parameters for Semiempirical Methods VI: More Modifications to the NDDO Approximations and Re-optimization of Parameters. *J. Mol. Model.* **2013**, *19*, 1−32.

[392] Grimme, S.; Ehrlich, S.; Goerigk, L. Effect of the Damping Function in Dispersion Corrected Density Functional Theory. *J. Comput. Chem.* **2011**, *32*, 1456−1465.

[393] J.J.P. Stewart, Optimization of Parameters for Semiempirical Methods II. Applications. *J . Comp. Chem.* **1989**, *10*, 221-264.

[394] Dewar, M. J. S.; Zoebisch, E.G.; Healy, E.F.; Stewart, J. J. P. Development and use of quantum mechanical molecular models. 76. AM1: A New General Purpose Quantum Mechanical Molecular Model. *J. Am. Chem. Soc.* **1985**, *107*, 3902-2909.

[395] Diederik, P. K.; Ba, J. L. ADAM: A Method for Stochastic Optimization. *AIP Conf. Proc.* **2014**, *1631*, 58-62.

[396] Glorot, X.; Bordes, A.; Bengio, Y. Deep Sparse Rectifier Neural Networks. *J. Mach. Learn. Res.* **2011**, *15*, 315−323.

[397] Coulson, C. A.; Fischer, I. XXXIV. Notes on the Molecular Orbital Treatment of the Hydrogen Molecule. *Philos. Mag.* **1949**, *40*, 386−393.

[398] Alecu, I. M.; Zheng, J.; Zhao, Y.; Truhlar, D. G. Computational thermochemistry: scale factor databases and scale factors for vibrational frequencies obtained from electronic model chemistries. *J. Chem. Theory Comput.* **2010,** *6*, 2872−2887.